Friction measurement with single atom resolution

DISSERTATION ZUR ERLANGUNG DES DOKTORGRADES DER NATURWISSEN-
SCHAFTEN (DR. RER. NAT.) DER FAKULTÄT FÜR PHYSIK

DER UNIVERSITÄT REGENSBURG

vorgelegt von

Shinjae Nam

aus Seoul, Süd-Korea

im Jahr 2024

Promotionsgesuch eingereicht am: 12. September 2024
Die Arbeit wurde angeleitet von: PD. Dr. Alfred J. Weymouth

Prüfungsausschuss:
Prof. Dr. Andrea Donarini
Prof. Dr. Rupert Huber
Prof. Dr. Isabella Gierz

Datum Promotionskolloquium: 7. November 2024

Contents

1 Introduction

Tribology, the study of friction, has a long history dating back to ancient Greek times, where the term 'tribos', meaning 'to rub', was coined [1]. Over this extensive period, the concept of friction has evolved and been explored across various fields [2, 3]. Understanding friction is essential for enhancing the efficiency and longevity of machinery, reducing energy consumption, and minimizing wear on mechanical components [4, 5]. In recent years, its relevance has expanded into fields such as biology and electronics, further broadening its scope.

For instance, at the microscale, reducing friction in devices like microelectromechanical systems (MEMS) [6, 7] and nanotechnology-based components can significantly improve durability and reliability. As devices become smaller, controlling friction at the nanoscale ensures smooth operation of key components like nanoswitches [8, 9] and actuators [10, 11]. This precise control also aids in constructing accurate nanoelectronic circuits [12] and advancing quantum computing systems [13, 14], where reduced friction and wear enhance both reliability and energy efficiency. Devices with minimized friction consume less energy, generate less heat, and become faster, more efficient, and longer-lasting.

2D materials, such as graphene and MoS_2, offer unique advantages in the context of friction [15]. These materials are incredibly thin and prone to wear, making it critical to understand friction at the atomic level to prevent degradation. Many 2D materials exhibit low friction, or even superlubricity [16, 17]. Atomic-level friction studies can also optimize mechanical stability and contact resistance in interfaces within 2D material-based devices, enhancing performance in flexible electronics and sensors [15, 18]. Understanding how friction affects heat generation at the atomic level is vital for designing improved thermal management systems.

In biology, studying friction at the atomic scale helps in understanding how cells and proteins interact with surfaces and each other, which is crucial for processes like cell adhesion, migration, and tissue formation [19–21]. Molecular friction insights are also important for designing medical devices and implants that interact smoothly with biological tissues, reducing wear and improving biocompatibility [22–24]. Additionally, friction at the molecular level influences protein folding [25, 26] and molecular motors [27, 28], essential for understanding diseases caused by protein misfolding, such as Alzheimers [29, 30]. Studying natural lubricants, like synovial fluid in joints, can lead to the development of synthetic lubricants [31, 32]. Overall, atomic-scale friction studies offer significant advancements across diverse fields, driving innovation and improving technologies.

Given these advancements, one might ask: How close are we to fully understanding friction at the atomic scale? While the practical significance of tribology is clear, the field still involves intriguing physics that remains not fully understood. As Feynman said in 1963, 'Quantitative experiments in friction are difficult, and the laws of friction remain poorly understood.' [33]. Despite significant strides in tribology, friction continues to present fundamental challenges, especially at the nanoscale, requiring precise and high-resolution measurements [34]. Turning to the evolution of measurement tools and their resolution, Atomic Force Microscopy (AFM) holds the leading position among instrumental setups, despite the development of various other measurement methods.

AFM, introduced by Binnig *et al.* in 1986, marked a significant advancement in measuring surface interactions [35]. In a typical AFM setup, a sharp microfabricated tip is scanned over a surface. This tip is mounted on a cantilever force sensor with sensitivity well below 1 nN [36]. Images of surface topography are recorded by maintaining a constant normal force, achieved through piezoresistive cantilevers or by reflecting a laser beam from the back of the cantilever into a photodetector [37]. Just one year after the invention of AFM, the first lattice-resolved maps of stick-slip motion were acquired by Mate and coworkers [38]. In this technique, as the cantilever sweeps over the sample in one direction and then back again, the energy dissipation can be calculated, providing valuable insight into frictional forces. Since then, known as Friction Force Microscopy (FFM), this method has been widely applied to measure friction at atomic resolution [39–42]. Stick-slip motion, a type of wearless friction, involves energy dissipation without material loss

and was first proposed by Prandtl and Tomlinson 60 years earlier [43, 44]. This model describes the interaction between a particle and a surface, where the particle is trapped behind a potential energy barrier (sticking to the surface) and is then suddenly released (slipping) when the applied force overcomes static friction.

By 1990, advancements in AFM techniques were evident with Meyer and Amers introduction of a laser beam reflected off the cantilevers back, which was later expanded to a four-cell detector to measure torsional modes [45, 46]. This period also saw the proposal of frequency-modulation atomic force microscopy (FM-AFM) by Albrecht and coworkers [47]. FM-AFM utilizes a phase-locked loop (PLL) to track the cantilevers resonance frequency, enabling detailed force measurements at the atomic scale. This method allows for precise mapping of vertical and lateral forces, revealing piconewton force contrasts in a deep non-contact regime.

In 1998, Giessibl introduced the qPlus sensor, based on a quartz tuning fork, to enhance atomic resolution measurements [48]. Its high stiffness allows for operation with small amplitudes in dynamic mode, addressing limitations of previous sensors. With the introduction of the qPlus sensor, lateral force measurements were also enhanced by rotating the cantilever, allowing its bending mode to cause the tip to oscillate along the surface [49, 50]. This technique, named frequency-modulation lateral force microscopy (FM-LFM or LFM) [37, 51], records both the frequency shift (Δf) and drive signal,[49], corresponding to conservative and non-conservative interactions, respectively. An additional advantage of LFM for measuring friction is its ability to control the tips apex at the single-atomic level. This precision allows for accurate manipulation of the tip apex atom and detailed measurement of surface features. A widely used method is functionalizing the metal tip with a single carbon monoxide (CO) molecule, a technique first developed by Gross *et al.* for STM/AFM experiments [52].

In this thesis, high-precision LFM measurements with atomically characterized tips are presented. The study includes an analysis of atomic interaction mechanisms affecting LFM contrast as a function of tip-sample distance. These tips are then used to investigate friction across single chemical bonds. Additionally, the contribution of phonons to frictional forces is explored. The remaining chapters of this work are outlined as follows. Chapter 2 introduces the fundamental principles of STM and AFM. Specifically, the FM-LFM mode of operation, which is used throughout this work, is described in detail. Additionally, it covers Density

Functional Theory (DFT) and the basic concepts of the calculations discussed in this thesis.

Chapter 3 describes the experimental setup and measurement techniques used in this study. It begins with a detailed account of the microscope setup used for the measurements, followed by an introduction to the qPlus sensor, which enables simultaneous STM and AFM measurements. The chapter also covers techniques for sample and tip preparation, including established characterization methods such as the carbon monoxide front atom identification (COFI) method [53–55] and the methodology for creating Hydrogen and Deuterium terminated tips.

Chapter 4 focuses on high-precision LFM measurements using an atomically characterized CO tip. Understanding the probe's features, such as contact conditions and the properties of the driving system (its stiffness), is crucial as friction depends on these factors [56]. The discussion includes how LFM can precisely measure in-plane interactions with high-resolution imaging of individual H atoms and studies the impact of the CO-functionalized tip on image interpretation. Until this point, only conservative interactions are addressed, and friction is not yet introduced.

Chapter 5 enhances the understanding of friction at the single-atom scale by mapping energy dissipation over single chemical bonds. It provides a detailed quantitative analysis of energy dissipation over various chemical bonds, supported by precise potential energy surface calculations. DFT calculations and machine learning models are used to refine predictions and apply the snapping model to energy dissipation. Analysis of covalent bonds in the PTCDA molecule reveals a linear relationship between energy dissipation and bond order, concluding higher bond orders correlate with greater dissipation. Interestingly, Newtons law, applied within the principle of least action, still holds relevance in single-atom friction scenarios, provided the potential energy of the system is known. However, the fate of the dissipated energy is less clear. Electronic friction and phononic contributions are often proposed as explanations, but important questions remain: What is the time scale of these processes, and what are we truly measuring in terms of energy dissipation? The slow cantilever hides most information about the rapid dynamics of the tip apex, making it challenging to identify the exact transition of mechanical energy to heat.

Chapter 6 explores the impact of atomic and molecular mass on the phononic contribution to friction, using isotopic variations to more closely address the pre-

viously raised questions. It starts with comparing isotopes of functionalized tip, $^{12}C^{16}O$ and $^{12}C^{18}O$, to find the phononic contribution to friction. Additionally, experiments with Si(100) surfaces terminated with Hydrogen and Deuterium were conducted since the mass ratio is larger for this sample. Hydrogen-terminated surfaces exhibited significantly higher energy dissipation when measured directly over the atoms. While the measurements match well with the theoretical value when taken directly over the atoms, the dissipated energy varies depending on the scanned area at single-atom resolution. These findings highlight the critical role of atomic mass in friction and suggest the need for further precise research to resolve discrepancies at the single-atom scale, thereby advancing the understanding of nanoscale friction mechanisms.

Finally, chapter 7 concludes with a summary of all the results presented within this thesis.

2 Fundamentals of scanning tunneling and atomic force microscopy

All experiments in this thesis were conducted using a combined scanning tunneling microscope (STM) and atomic force microscope (AFM) using the qPlus sensor for simultaneous STM and AFM measurements [36]. This chapter provides a description of the fundamental principles of STM (section 2.1) and AFM (section 2.2).

2.1 Scanning tunneling microscopy

The scanning Tunneling Microscope (STM)[1] is the first instrument that allowed imaging surfaces at the atomic resolution, which was invented in 1982 by Gerd Binnig and Heinrich Rohrer [57]. Since then, it has paved the way for numerous discoveries in materials science, chemistry, and nanotechnology. This chapter summarizes the main concepts relevant for the present work based on Ref. [58]. The basic instrumentation and parameters are introduced, followed by the theoretical background of their working procedures.

The STM consists of a sharp metal tip that is brought very close to the surface of an atomically flat sample. The tip is mounted on a scanner equipped with three mutually perpendicular piezoelectric transducers, which can move the tip laterally in the $x\,y$-plane and vertically in the z-direction by applying a voltage to each piezo. Beneath the scanner, a piezo walker mechanism provides coarse approach capabilities. Vibration isolation system, including an eddy current damper with a

[1] In this work, STM refers to both the technique of scanning tunneling microscopy and the instrument, scanning tunneling microscope.

spring and a damping stage, ensures a stable operating environment by minimizing vibrations. Control electronics manage the electric signals necessary for the control of STM systems. STM uses the quantum mechanical tunneling current flowing through the vacuum gap, between the tip and the sample as measurement signal [58]. When the tip is sufficiently close to the sample (approximately 500 pm, a few atomic diameters), tunneling conductance arises, and a bias voltage V_{B} applied between the tip and sample makes electrons tunnel through the vacuum gap. The current amplifier converts the tunneling current into a voltage signal, which will be compared to a reference signal. This tunneling current, I, is used as the feedback signal in a z-feedback loop [58]. The STM image can be obtained by raster scanning over the surface. The constant current mode images are created by recording the z position while keeping I as constant. Constant height mode records I at the same z position.

The tunneling current can be described by a simple 1D model [59]. When V_{B} is small compared to the work function of tip and sample, the vacuum gap (tunneling barrier) is roughly rectangular with a width z, where z is defined as tip-sample distance. The barrier height is given by the average work function, $\Phi = (\Phi_{\mathrm{t}} + \Phi_{\mathrm{s}})/2$, of the tip ($\Phi_{\mathrm{t}}$) and sample ($\Phi_{\mathrm{s}}$). By solving the Schrödinger equation, the tunneling current is given by

$$I(z) = I_0 e^{-2\kappa z} \tag{2.1}$$

where I_0 is a function of the applied voltage and $\kappa = \sqrt{2m_{\mathrm{e}}\Phi/\hbar^2}$, m_{e} is the free electron mass and $\hbar$ is the reduced Plancks constant. The tunneling current has an exponential distance dependence and most of the tunneling current is carried by the front atom that is closest to the sample. This allows STM to easily achieve the atomic resolution imaging.

To account for the influences of the applied bias voltage and the electronic properties of the tip and sample, and temperature, the tunneling current I can be described by *Bardeen's theory* [60]. For tunneling across a barrier, Bardeens work on the tunneling current I through an insulating barrier can be described by:

$$I = \frac{e^2}{h} \int_{-\infty}^{\infty} T(E) \left[f(E - \mu_1) - f(E - \mu_2) \right] \, dE \tag{2.2}$$

where e is the electron charge, h is Plancks constant. $T(E)$ is the transmission

coefficient (probability of tunneling), and $f(E-\mu_i)$ is the Fermi-Dirac distribution function for the two electrodes with chemical potentials μ_1 and μ_2.

According to this theory, the tunneling current I is given by the following integral over the energy ϵ:

$$I = \frac{4\pi}{\hbar}\int_{-\infty}^{\infty}[f(E_\mathrm{F}-eV_\mathrm{B}+\epsilon)-f(E_\mathrm{F}+\epsilon)]\rho_t(E_\mathrm{F}-eV_\mathrm{B}+\epsilon)\rho_s(E_\mathrm{F}+\epsilon)|M_\mathrm{ts}|^2\,d\epsilon \quad (2.3)$$

where $f(E)$ is the Fermi-Dirac distribution function which describes the occupancy of electronic states. It is given by $f(E) = [1+\exp((E-E_\mathrm{F})/k_\mathrm{B}T)]^{-1}$, where E_F is the Fermi energy, k_B is the Boltzmann constant, and T is the temperature. ρ_t and ρ_s are the densities of states of the tip and the sample, respectively, and E_F is the Fermi energy. The tunneling current is expressed in terms of the matrix element M_ts, which represents the overlap of the tip and sample wave functions across the tunneling barrier. Therefore, $|M_\mathrm{ts}|^2$ determines the tunneling probability between the two electrodes [58].

Since the Fermi-Dirac distribution approximates a step function at low temperatures and the energy is confined within the applied voltage, equation (2.3) can be:

$$I(V_\mathrm{B}) = \frac{4\pi e^2}{\hbar}\int_0^{eV_\mathrm{B}}\rho_\mathrm{s}(E_\mathrm{F}-eV_\mathrm{B}+\varepsilon)\rho_\mathrm{t}(E_\mathrm{F}+\varepsilon)|M_\mathrm{ts}|^2\,d\varepsilon \quad (2.4)$$

While equation (2.4) primarily addresses tunneling phenomena, it illustrates the difficulty in interpreting STM images, as the tunneling current depends on the local density of states (LDOS) of both the tip and the sample.

This can be simplified in a more practical approach for STM experiments by assuming that $|M_\mathrm{ts}|^2$ is constant [60] and that the tip has a geometry of s-type wave functions. This is a reasonable assumption for metal tips [60, 61], implying that ρ_t is constant around E_F. Then equation (2.4) becomes [58, 61, 62]:

$$I(V_\mathrm{B}) \propto \int_0^{eV_\mathrm{B}}\rho_\mathrm{s}(E_\mathrm{F}-eV_\mathrm{B}+\varepsilon)\,d\varepsilon \quad (2.5)$$

This implies that the STM probes the LDOS of the sample at the Fermi level rather than the surface topography when using metal tips [58, 63].

While STM primarily provides spatial information about surface topography, Scanning Tunneling Spectroscopy (STS) focuses on the electronic properties of materials. STS measures the tunneling current as a function of the applied voltage

between the tip and the sample. The current-voltage ($I(V_\mathrm{B})$) characteristic reveals information about the local density of states (LDOS) of the sample, as described by equation (2.5). To enhance sensitivity, an AC voltage is applied during the voltage ramp, allowing measurement of the current derivative, which is directly related to the LDOS ($\frac{dI}{dV} \propto \rho_\mathrm{s}(E_\mathrm{F} - eV_\mathrm{B})$). For the work in this thesis, a lock-in demodulator within the Nanonis system was used.

Previous discussions considered only elastic tunneling, where electrons tunnel into states with the same energy as their initial state. Inelastic tunneling, on the other hand, involves electrons gaining or losing energy at specific values, $\hbar\omega$, which opens additional tunneling channels [64]. This expanded spectroscopy technique is often referred to as Inelastic Electron Tunneling Spectroscopy (IETS)[1].

The concept of IETS was first discovered by Jaklevic and Lambe in 1966 while studying metaloxidemetal junctions [65]. Contrary to their initial expectation of observing band structure effects in the metal electrodes, they identified patterns in the characteristics related to vibrational excitations of molecular impurities within the insulator [65]. Fig. 2.1 shows the schematic concept of the IETS mechanism. Fig. 2.1 A illustrates the energy band diagram of a tunnel junction with a vibrational mode of frequency ω localized inside. The elastic tunneling process is depicted in blue, while the inelastic tunneling process is shown in red. When a negative bias is applied to the left metal electrode (the tip electrode in this case), the left Fermi level is lifted. An electron from an occupied state on the left side tunnels into an empty state on the right side, and its energy is conserved (blue process). This is the elastic process, where the current increases linearly with the applied small bias as shown in Fig. 2.1 B. However, if there is a vibrational mode with a frequency ω localized inside the barrier, when the applied bias is large enough such that $eV \geq \hbar\omega$, the electron can lose an energy, $\hbar\omega$, by exciting the vibration mode and tunnel into another empty state (red process) [64]. This opens an inelastic tunneling channel for the electron, increasing its overall tunneling probability. Consequently, the total tunneling current exhibits a kink as a function of the applied bias as shown in Fig. 2.1 B. This kink appears as a step in the differential conductance $\frac{dI}{dV}$ plot and as a peak in the $\frac{d^2I}{dV^2}$ plot.

[1] In this work, IETS denotes both the technique of inelastic electron tunneling spectroscopy and the resulting measurements, referred to as inelastic electron tunneling spectra (or spectrum for a single measurement).

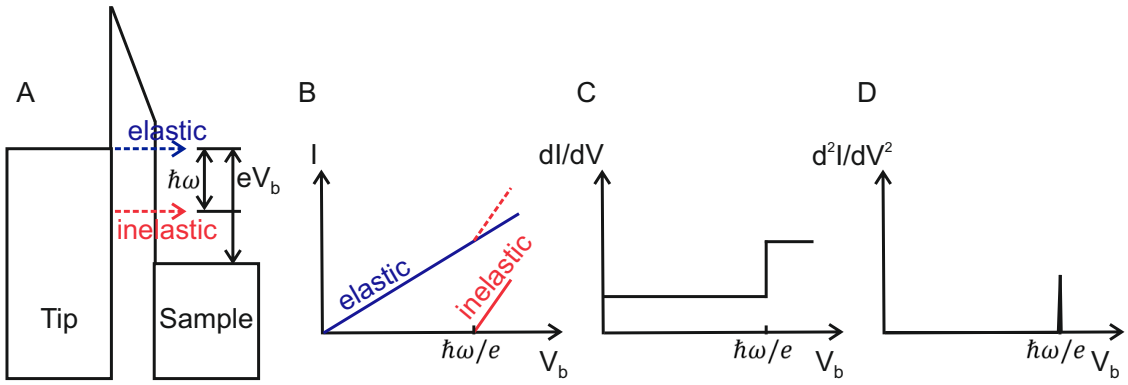

Figure 2.1: Principle of inelastic electron tunneling spectroscopy. (A) Energy band diagram of a tunnel junction with an inelastic excitation. When an electron has a sufficient energy to induce an inelastic process ($E > \hbar\omega$), the electron can either tunnel elastically from the tip to the sample, or transfer part of its energy to occupy a energetically lower unoccupied state. (B) In the $I(V_B)$ curve, the opening of an inelastic conduction channel is translated into a change in the slope for $V_B > \hbar\omega/e$. Inelastic excitation can be better detected in the (C) $dI/dV(V_B)$ curve where it appears as a step and in the (D) $d^2I/dV^2(V_B)$ as a peak.

In experiments, IETS often used to study the electronic or vibrational properties of molecules and materials,excited via certain energy, $\hbar\omega$, including chemical identification, bonding investigation, trace substance detection, and spin-flip excitation [64, 66–69]. Although IETS has been called by different names depending on the specific mechanisms involved, the measurement method remains similar to that used in STS.

2.2 Atomic force microscopy

The limitation of the STM is that only conducting materials can be investigated. Later, Binnig observed that atomic forces played a crucial role in the operation of the STM and suggested that these forces could be harnessed for a new type of microscope capable of imaging insulating surfaces [35, 70]. In 1986 [35], Binnig *et al.* conceptualized and developed the AFM, a revolutionary tool that extended the atomic resolution capability of STM to non-conducting samples [35, 70, 71]. The first AFM successfully imaged insulating surfaces with atomic resolution, paving the way for its widespread application in various fields, including materials science, biology, and nanotechnology.

AFM is well-described in various review papers and books [36, 58, 70, 72] and the following section briefly introduces the main concepts behind the technique mainly based on the explanations in Ref. [36, 51]. AFM operates by measuring the forces between a sharp tip and the sample surface. The tip is mounted on a flexible cantilever with a known spring constant k. The interactions between the tip and the sample surface cause the cantilever to bend. This deflection is then measured and used to image the surface topography.

Depending on how this deflection measurement is detected, AFM operates in several distinct modes, each tailored to different types of measurements and sample properties. The primary operating modes of AFM include three main types, including contact mode, Amplitude Modulation (AM) mode, and Frequency Modulation (FM) mode [36, 70].

The contact mode is the simplest mode of AFM, where the AFM tip remains in continuous contact with the sample surface as it scans. The deflection of the cantilever, Δz, is directly measured, providing topographical maps of the sample. This deflection is related to the force, F, exerted on the cantilever by the interaction between tip and sample through Hooke's law, $F = k\Delta z$, where k is the spring constant of the cantilever. Contact mode is advantageous for hard surfaces but can be less suitable for soft or delicate samples due to potential damage from the constant contact. Despite its limitations, contact mode remains a fundamental technique for obtaining detailed surface information.

The two main dynamic modes are AM mode and FM mode [37, 58]. AM-AFM involves oscillating the cantilever with a constant drive amplitude at a fixed frequency near the cantilever's unperturbed resonant frequency (f_0). The oscillation amplitude is related to the tip-sample interaction forces:

$$A = A_0 \cos(\phi) \tag{2.6}$$

where A_0 is the free oscillation amplitude and ϕ is the phase shift caused by the tip-sample interaction. Therefore, the tip-sample interaction results in a deviation of both the amplitude and phase of the cantilever motion. The changes in the oscillation amplitude or phase provide the feedback signal for imaging. Currently, most AFMs operating in ambient conditions use AM mode, which has the advantage of being conceptually simple, but it also has a few drawbacks.

First, it is impractical for low temperature experiments that usually require the cantilevers to have a high Q factor. The responding time scale of FM-AFM is given by $\tau_{\mathrm{AM}} \approx 2Q/f_0$, and quality factor of the cantilever is defined by $Q = \frac{f_0}{\Delta f}$ where f_0 is the resonant frequency of the cantilever and Δf is the full-width at half-maximum of the resonance peak [36, 47]. For example, the sensor that is used in this thesis, has nearly 50,000 Q factor with a resonance frequency of 37 kHz, then the time scales on which the amplitude change responds to the tip-sample force will be $\tau_{\mathrm{AM}} \approx 2(50,000)/37\,\mathrm{kHz}$ =1.35 s. Second, extracting forces using this method is more complex and usually requires assumptions about the tip-sample contact [37, 73] or about its motion [74]. Third, distinguishing dissipative and non-dissipative parts of the interaction force components is not straightforward with a monotonic feedback signal. In 1990, Albrecht *et al.* proposed FM-AFM to take advantage of cantilevers with a larger Q-value [47], and with this mode, the three points described above can be improved.

2.2.1 Frequency modulation atomic force microscopy

FM-AFM directly measures changes in the resonant frequency of the cantilever caused by tip-sample interaction. This provides a direct relationship between frequency shifts and force gradients, making quantitative analysis more straightforward. The key to this technique is utilizing a phase-locked loop (PLL) to follow the resonance frequency f_0, and drive the cantilever at that frequency [47]. The frequency shift, $\Delta f = f - f_0$, is used as a feedback signal to control the cantilever height. A second feedback loop adjusts the drive amplitude A_{drive} to keep the oscillation amplitude A fixed and independent of the interaction between the tip and the sample. This strictly separates dissipative and non-dissipative interactions [36].

The force sensor oscillating at a constant amplitude can be described by a harmonic oscillator. At far distance, when the force gradient field between the tip and the sample is close to zero, the oscillation frequency is the same as the eigenfrequency of the cantilever:

$$f_0 = \frac{1}{2\pi}\sqrt{\frac{k}{m^*}} \tag{2.7}$$

where k is the stiffness, and m^* is the effective mass of the cantilever. For a smaller distances, when the tip sample interaction F_{ts} is detected, the spring constant will

be changed to $k' = k + k_{\mathrm{ts}}$, where k_{ts} is defined as $k_{\mathrm{ts}} = -\partial F_{\mathrm{ts}}/\partial z$ with tip-sample separation z. If $k_{\mathrm{ts}} << k$, the square root can be expanded as a Taylor series and the shift of the resonance frequency, $\Delta f = f - f_0$, is approximately given as $\Delta f = \frac{k_{\mathrm{ts}}(z)}{2k} f_0$, where z is the tip-sample distance [36].

To convert Δf into force, k_{ts} must be integrated. For a conservative force field, this integration provides the potential energy. When the small-amplitude approximation is not valid, the cantilever's motion must be considered. (When k_{ts} is not constant over the oscillation cycle.) In such cases, the weighted force gradient $\langle k_{\mathrm{ts}} \rangle$ replaces k_{ts} in the formula, and calculating k_{ts} from $\langle k_{\mathrm{ts}} \rangle$ is called deconvolution [75–77]. Common deconvolution methods include the SaderJarvis method [78] and the Giessibl matrix method [77] for normal AFM (oscillating vertically), and Fourier method [79] for lateral force microscope (LFM) (oscillating laterally).

Conservative force between the tip and the sample can be obtained from the frequency shift using above method. When the tip-sample forces vary between forward and backward traces during oscillation, the force field is not conservative anymore. In such cases, the amplitude feedback circuit must adjust its drive signal (A_{drive}) to keep the oscillation amplitude (A) constant [70, 77]. The drive amplitude for a cantilever in a conservative force field is $A_{\mathrm{drive}} = A/Q$ where Q is the quality factor of the sensor, and the energy loss by internal friction in the force sensor is given by:

$$\Delta E_{\mathrm{cl}} = \frac{\pi k A^2}{Q} \tag{2.8}$$

per oscillation cycle. For non-conservative forces, the integral over one oscillation cycle (running from $q' = -A$ to $q' = A$ for forward, and coming back to $q' = -A$ for backward direction), $\Delta E_{\mathrm{ts}} = \int_{-A}^{A} F_{\mathrm{ts}}(x+q')\, dq'$, is nonzero. Here, x is oscillation direction, and is parallel to the surface for LFM cases [56]. Then the adjusted drive amplitude can be written as:

$$A'_{\mathrm{drive}} = A_{\mathrm{drive}} \left(1 + \frac{\Delta E_{\mathrm{ts}}}{\Delta E_{\mathrm{cl}}}\right) \tag{2.9}$$

Therefore, energy dissipation can be calculated by monitoring A_{drive}:

$$\Delta E_{\mathrm{ts}} = \frac{\pi k A^2}{Q} \left(A'_{\mathrm{drive}} - A_{\mathrm{drive}}\right) \tag{2.10}$$

In this thesis, ΔE_{ts} is defined as friction, and labeled E_{diss}.

2.2.2 Forces detected in lateral force microscopy

The frequency shift is determined by the total tip-sample forces, $F_{\mathrm{ts}} = -dV_{\mathrm{ts}}/dx$ where V_{ts} is potential energy between the tip and sample, and x is sensor oscillation direction. While the tunneling current has a very short-range, F_{ts} has both long- and short-range contributions. This section introduces primary tip-sample interactions commonly observed in LFM experiments conducted in ultra high vacuum settings.

The van der Waals interaction is a major long-range force that arises from correlated fluctuations of atomic dipole moments [36]. The potential energy of the vdW interaction between two isolated atoms at a distance z is given by:

$$V_{\mathrm{vdW}}(z) = -\frac{C_{\mathrm{vdW}}}{z^6}, \tag{2.11}$$

where C_{vdW} is the London-van der Waals constant, which depends on the chemical species of the interacting atoms [80, 81]. Although this interaction is fundamentally short ranged, its effects can extend over larger distances when considering macroscopic shape of both tip and sample. In the Hamaker approximation, the total vdW interaction is determined by summing the contributions from all atomic pairs. Therefore, the shapes of the tip and sample also should be considered. For a spherical tip with radius R and a flat sample, the total vdW force is given by:

$$F_{\mathrm{vdW}}(z) = -\frac{\partial V_{\mathrm{vdW}}}{\partial z} = -\frac{A_{\mathrm{H}} R}{z^2}, \tag{2.12}$$

where A_{H} is the Hamaker constant, which depends on the materials of the tip and sample [82]. This formula describes a long-range attractive interaction that decreases as the tip radius R decreases, i.e., if the macroscopic tip shape is sharpened [75]. In this context, many of tip sharpening and shaping methods have been developed, and some of them are introduced in section 3.3.

Most long-range interactions are typically oriented normal to the surface [37], whereas short-range interactions have a strong lateral component. To explicitly measure potential energy using conventional AFM, where the sensor oscillates normal to the surface, it is necessary to account for and subtract the effects of long-

range interactions. This can be done either by estimating the long-range component or by measuring it away from the adsorbate of interest. Thereofre, LFM is ideal for detecting short-range interactions and generally does not require the subtraction of long-range van der Waals and electrostatic interactions.

When the tip-sample distance is smaller, Pauli repulsion should be considered. Pauli Repulsion refers to the repulsive force that arises due to the Pauli exclusion principle, which states that no two fermions (e.g. electrons) can occupy the same quantum state simultaneously. As two atoms come very close to each other, their electron clouds begin to overlap, leading to a strong repulsive force as the electrons are forced into higher energy states to avoid overlapping. This repulsive interaction counters the van der Waals attraction at closer distances and is crucial for understanding the short-range behavior of atomic and molecular systems.

The Lennard-Jones potential describes the interaction between a pair of neutral atoms or molecules. It combines attractive and repulsive forces and is given by:

$$V_{\mathrm{LJ}}(z) = V_0 \left[\left(\frac{\sigma}{z} \right)^{12} - 2 \left(\frac{\sigma}{z} \right)^{6} \right] \tag{2.13}$$

where V_0 is the depth of the potential well, σ is the equilibrium distance at which the potential is zero. The $\left(\frac{\sigma}{z}\right)^{12}$ term represents the repulsive force due to Pauli exclusion, which grows rapidly as atoms approach each other. The $\left(\frac{\sigma}{z}\right)^{6}$ term represents the attractive van der Waals force, which decreases more slowly with distance. The combination of these terms gives rise to a potential that has a minimum, representing the stable interaction distance between the atoms.

The Morse Potential is another model used to describe the interaction between two atoms in a diatomic molecule. It is particularly useful for modeling molecular vibrations and bond dissociation. The Morse potential is given by:

$$V_{\mathrm{Morse}}(z) = D_e \left[1 - e^{-a(z - r_e)} \right]^2 \tag{2.14}$$

where D_e is the dissociation energy, r_e is the equilibrium bond length, and a is a parameter related to the width of the potential well.

The short range electrostatic forces arise from the interactions between charged entities and can be either attractive or repulsive. This has been described in a good approximation by the force acting on a point charge (or a single dipole moment)

representing the tip apex in the electric field of the sample. Coulomb's law describes the electrostatic force F between two point charges q_1 and q_2 separated by a distance r:

$$F = \frac{1}{4\pi\epsilon_0}\frac{q_1 q_2}{r^2}, \tag{2.15}$$

where ϵ_0 is the permittivity of free space ($8.85 \times 10^{-12}\ F/m$). In AFM, if the tip and sample are conductive or charged, these forces significantly influence the cantilever's frequency shift.

2.3 Density functional theory

Density Functional Theory (DFT) is a computational quantum mechanical modeling method used to investigate the electronic structure of many-body systems, primarily atoms, molecules, and solids. It is based on the electron density rather than the wavefunction, making it more computationally efficient for large systems. The central concept in DFT is the electron density ($\rho(\mathbf{r})$), which represents the probability distribution of electrons in a system [83]. The Kohn-Sham equations, a set of self-consistent equations, simplify the many-body problem to a series of non-interacting particles moving in an effective potential [84]. The exchange-correlation functional ($E_{xc}[\rho]$) accounts for the complex many-body effects of electron exchange and correlation.

The total energy $E[\rho]$ of a system within DFT is given by:

$$E[\rho] = T_s[\rho] + V_{\text{ext}}[\rho] + J[\rho] + E_{xc}[\rho], \tag{2.16}$$

where $T_s[\rho]$ is the kinetic energy of a system of non-interacting electrons with density ρ, $V_{ext}[\rho]$ is the external potential energy, $J[\rho]$ is the classical electrostatic (Hartree) energy, representing the energy contribution due to the classical Coulomb interaction between electrons. $E_{xc}[\rho]$ is the exchange-correlation energy. The Kohn-Sham equations, which must be solved self-consistently, are:

$$\left(-\frac{\hbar^2}{2m}\nabla^2 + V_{eff}(\mathbf{r})\right)\psi_i(\mathbf{r}) = \epsilon_i\psi_i(\mathbf{r}),$$

where $V_{eff}(\mathbf{r})$ is the effective potential including the external potential, Hartree

potential, and exchange-correlation potential [85].

The central idea of DFT is to describe the system in terms of its electron density rather than the many-body wavefunction. The electron density, $\rho(\vec{r})$, is a function of spatial coordinates and provides information about the probability of finding an electron. In this thesis, DFT modeling was used to determine the atomic positions of two PTCDA molecules in a super cell on the Cu(111) surface. Calculations were done using the FHI-aims quantum chemistry code [86]. We used a PBE exchange-correlation functional [87] and the TSsurf van der Waals correction scheme [88, 89]. While the experimentally observed superstructure appears to be incommensurate, a commensurate structure was used as has been previously discussed in the literature as a necessary balance between accuracy and computational power [30]. The interaction of the second sliding surface, to study friction in chapter 5, is predominantly via the CO at the apex. To describe this interaction over a range of vertical and horizontal positions, a machine-learning model was used to determine the potential energy for each position of the O atom at the apex assuming a vertically-oriented CO molecule. The training data for this machine-learning model was also calculated with DFT. This potential energy landscape was then one input into a snapping model (in chapter 5) which simulates the oscillation of the tip at a certain point assuming that the CO at the apex responds to applied forces as a torsional spring and that the atoms of the surface are fixed. These assumptions are the same as those fo the successful Probe Particle Model [90], used to simulate df images of normal-force AFM images with a functionalized tip.

DFT can provide detailed atomic-level insights that complement FM-AFM measurements [91]. First, in surface characterization, DFT calculations can predict precise atomic positions and surface reconstructions, aiding in the interpretation of atomic-scale features observed in FM-AFM images. Additionally, DFT offers information on electronic states and the density of states, which helps understand contrast mechanisms in AFM images, especially for conductors and semiconductors.

Second, regarding interaction forces, DFT can calculate the forces between the AFM tip and sample atoms. These calculations assist in understanding the origin of frequency shifts observed in FM-AFM. By mapping potential energy surfaces, DFT predicts how the AFM tip interacts with different sites on the sample, aiding in the quantitative interpretation of data.

Third, for tip-sample interactions, DFT helps identify the chemical nature of

the interaction between the AFM tip and specific sample sites, which is crucial for understanding contrast in AFM images. It also provides detailed insights into bonding characteristics and adhesion energies between the tip and the sample.

DFT is a powerful computational tool that offers detailed atomic and electronic insights into material properties. When used in conjunction with FM-AFM, DFT calculations enhance the understanding of surface interactions, aid in interpreting frequency shifts, and help identify the chemical and electronic properties of the sample, thereby enriching the data obtained from FM-AFM measurements.

3 Experimental setup

This chapter outlines the experimental setup used for the measurements in this thesis. The experiments were conducted using a commercial microscope setup that has been modified for LFM, which is described in section 3.1. This microscope is equipped with a qPlus sensor that enables simultaneous STM and AFM measurements. The sample preparation procedure is detailed in section 3.2. Finally, section 3.3 covers the LFM sensor preparation based on the qPlus sensor, followed by a detailed explanation of the methods for tip preparation and characterization.

3.1 Low-temperature STM/LFM

All experimental data presented in this thesis have been collected on a low-temperature STM/AFM system manufactured by CreaTec Fischer and Co. GmbH that has been modified for LFM sensors, as described in Refs. [49, 92] and section 3.3. The temperature of the STM/AFM head is maintained at 5.2 K for 72 hours using a bath-type cryostat with an outer liquid nitrogen container covering an inner liquid helium vessel. The control electronics are Nanonis electronics manufactured by SPECS Zurich GmbH. To minimize mechanical noise, the entire system is equipped with air-cushion vibration dampers, and the STM/AFM head is supported by three suspension springs with an eddy current damper. The whole system can be separated into three main parts via gate valves: load lock, preparation chamber, and measurement chamber. The load lock chamber enables the transfer of samples and sensors to the UHV system from air without venting the entire system. The pressure of the load lock chamber can be reduced to a low value of 10^{-8} mbar after 12 hours of pumping using a rotary pump and turbo pump. Both the preparation chamber and measurement chamber maintain their UHV condition (2×10^{-10} mbar) via continuously pumping ion pumps. Each ion pump contains titanium sublimation pumps that are regularly flashed. Samples are degassed and prepared on a manipulator

installed in the preparation chamber. The preparation chamber contains two leak valves and one thermal evaporator, which includes two molecular crucibles.

The prepared sample is transferred to the measurement chamber, which houses the cryostat and microscope head, thermally connected to the cryostat. Opration in low temperature minimizes the thermal drift and prevents thermal desorption or diffusion of adsorbates. The control electronics are connected to the microscope head via electric cables that enter the UHV system through UHV feedthroughs at the top of the cryostat. A cryogenic deflection pre-amplifier, the AD8616, is used for the AFM to minimize capacitance to the input signal by reducing the cable length [70]. The tunneling current is measured via the tip using a separate commercial FEMTO transimpedance amplifier. For the work presented in this thesis, the bias voltage is applied to the sample side.

A customized gas line system is additionally equipped, consisting of three separate lines, each connected to the chamber via separate leak valves. The first line is used to dose Argon (Ar) gas into the preparation chamber for Ar-ion sputtering of the samples. The second line can support up to three different gas bottles and is used to dose H_2 and D_2 gases for preparing H/D-terminated Si(100) samples. The third line is connected to the main chamber and is used to dose isotopes of carbon monoxide (CO) gas into the UHV system. Further details on the sample preparation process are described in section 3.2.

3.2 Sample preparation

The measurements performed in this thesis were carried out on (1) single-crystal metallic surface of Cu(111) with evaporated molecules and, (2) Si(100) surface terminated with Hydrogen and Deuterium atoms. Following sections will describe the procedure of the sample preparation and basic surface characteristics.

3.2.1 PTCDA / Cu(111)

The Cu(111) sample is cleaned through repeated sputtering and annealing cycles [62]. For sputtering, the preparation chamber is pumped with a turbo pump, and Ar gas is introduced via a leak valve until pressure reaches around value of 2.0×10^{-6} mbar. The gate valve connected to the ion getter pump is closed during

the sample preparation. The sample is then sputtered for 20 minutes with Ar^+ ions, which are accelerated to a kinetic energy of $E_{\text{kin}} = 1.1\,\text{keV}$ via sputter gun. By directing Ar^+ ions onto the sample surface, contaminants are removed, and multiple atomic layers of the Cu crystal are ablated, generally resulting in a relatively rough surface with only small terraces [93]. This causes an emission current to flow through the sample, and the Ar gas pressure is finely adjusted to achieve an emission current of $2\,\mu\text{A}$. Next, the Ar gas is pumped out of the chamber, and the surface is annealed for 20 minutes at a temperature of approximately 550 °C, resulting in a flat sample surface with single-atom steps and terraces on the order of several hundred nm^2. Depending on the level of contamination, this cleaning cycle (consisting of 20 minutes of sputtering followed by 15 minutes of annealing) is repeated 25 times to clean the Cu single crystal.

Copper crystallizes in a face-centered cubic (fcc) lattice with a cubic lattice constant of $a_0 = 361.5\,\text{pm}$. Hence, the Cu(111) surface shows a hexagonal lattice with a nearest-neighbor distance of $d_{nn} = a_0/\sqrt{2} = 255.6\,\text{pm}$. The distance between (111) planes is $d_{(111)} = a_0/\sqrt{3} = 208.7\,\text{pm}$. Steps on Cu(111) should therefore be integer multiples of $d_{(111)}$, where a step height of $1 \times d_{(111)}$ corresponds to a single-atom step. Figure 3.1A shows an STM topography image of the Cu(111) sample after cleaning with sputtering and annealing, revealing two step edges.

To make a CO functionalized tip, single CO molecules should be adsorbed on the Cu(111) sample. Since CO desorbs from Cu surfaces well at room temperature, CO molecules were dosed on the cold sample inside the microscope head after cleaning and cooled down to 5.2 K. CO gas is leaked into the analysis chamber via the gas line system until the pressure reaches $\approx 3.0 \times 10^{-8}$ mbar. During this process, the gate valve in front of the ion pump is closed. Subsequently, the small thermal shield at microscope head, facing to the CO leak valve, is opened for 13 minutes, depending on the desired amount of CO. A dosage time of 1.5 minutes results in a coverage of about 0.01 ML CO. Single CO adsorbates appear as dark spots in the STM topography when probed with a metal tip at small bias voltages [94], as shown in Fig. 3.1.

A thermal evaporator is used in preparation chamber to deposit molecules onto substrates after the clean surface is scanned. The crucible, which contains the molecules, is heated to a high temperature via a filament that surrounds it until the material sublimates or evaporates. The filament is heated through power supplied

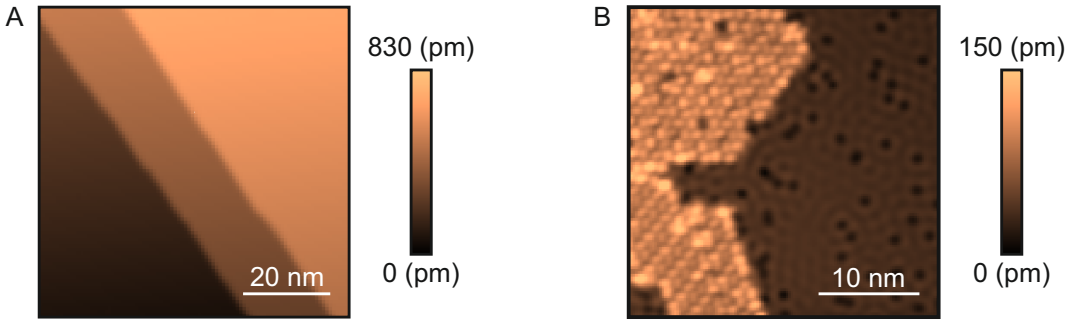

Figure 3.1: The PTCDA/Cu(111) sample with COs. (A) STM topography image recorded of the Cu(111) sample after cleaning with sputter and anneal cycles. Imaging parameter: $V_B = 1\,V$ and $I_{set} = 100\,pA$ (B) STM topography image of the Cu(111) surface after PTCDA and CO adsorption. CO molecules appear as dark features, and PTCDA molecules form islands having herringbone structure. Imaging parameters: $V_B = 100\,mV$ and $I_{set} = 100\,pA$

via a connected feedthrough. The vapor then travels through inside the vacuum chamber and condenses onto the target surface or substrate, forming a thin film. The shutters opening and closing regulate the flow of the molecular beam. In this work, PTCDA (3,4,9,10 - perylenetetracarboxylicdianhydride) molecule was used for chapter 4 and 5.

0.5 ML coverage of PTCDA molecular islands are formed with a heating power of 1.4 A and 5.0 V for a deposition time of 1.5 minutes. During this process, the vacuum in the preparation chamber increased from approximately 2.0×10^{-10} mbar to 3.0×10^{-8} mbar. The evaporator was warmed up for 6 minutes with a same power of deposition prior to opening the shutter. Fig. 3.1B shows the surface with the PTCDA molecular island and dosed CO molecules.

3.2.2 H/D terminated Si(100)

The polished and cut to [110] direction wafer of the highly arsenic-doped Si(100) sample (with resistivity of 0.003 - 0.004 Ω· cm) was used. The sample was placed in the sample holder, gripped at the sides, and adjusted to be perpendicular to the sensor direction, as shown in Fig. 3.2 A. This adjustment allowed LFM measurements in both perpendicular and parallel directions relative to the Si(100) dimer row and the oscillation direction, which will be discussed further in chapter 6. The entire sample was degassed at 600 °C with e-beam heating in UHV for 24 hours to

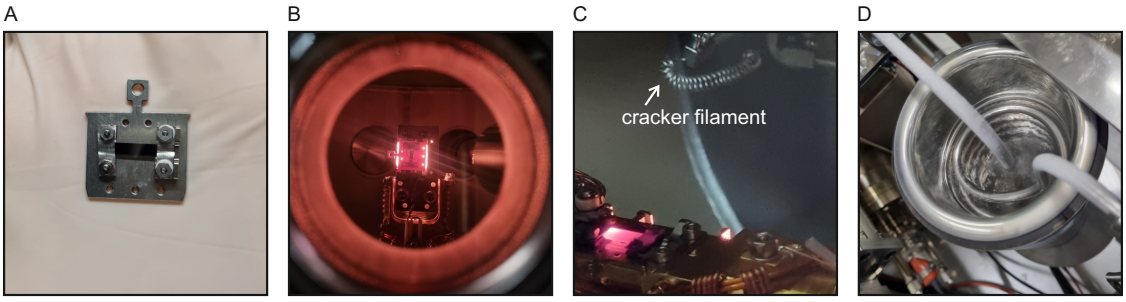

Figure 3.2: Custom-built Si(100) and hydrogen cracker. (A) The wafer, polished and cut in the [110] direction, was adjusted in the sample holder to be perpendicular to the sensor direction, allowing LFM measurements in both perpendicular and parallel directions relative to the Si(100) dimer row and oscillation direction. (B) The sample was degassed at 600 °C using e-beam heating in UHV for 24 hours to remove adsorbed water. (C) Native oxide layers were removed by resistive heating with rapid flashes up to 1150 °C, maintaining the preparation chamber pressure below 5.0×10^{-10} mbar and ensuring a clean surface when flashing pressures did not exceed 2.0×10^{-9} mbar. The surface was then terminated with H or D atoms by exposing the flashed sample to hydrogen gas passed through a homemade cracker at 1×10^{-6} mbar. A tungsten filament at 1900 °C dissociated the hydrogen gas into atomic hydrogen. (D) To ensure the cleanness of H_2 and D_2, the gas line was cooled with liquid nitrogen, minimizing impurities in the gas.

remove any adsorbed water after exposure to air as shown in Fig. 3.2 B. Then, it was resistively heated through rapid flashes up to 1150 °C several times to remove native oxide layers, as presented in Fig. 3.2 C. The temperature was measured using a pyrometer. The preparation chamber pressure was maintained below 5.0×10^{-10} mbar before flashing. A clean sample was typically ensured if the maximum pressure remained under 2.0×10^{-9} mbar during flashing. Between flashes, the sample was cooled to 600 °C for around 5 minutes.

To terminate the surface with H or D atoms, a homemade cracker was used to dissociate H_2 and D_2 molecules dosed in the chamber via a leak valve. The flashed sample was exposed to Hydrogen gas passed through the cracker at a pressure of 1 Œ 10^{-6} mbar, with the ion pump closed. A tungsten filament, maintained at 1900 °C, was used to dissociate the Hydrogen gas into atomic Hydrogen. After waiting for 120 seconds without additional heating, the sample was turned to face the cracker filament, indicated with a white arrow in Fig. 3.2 C. The sample temperature is 330 °C during H-termination, for making the Hydrogen-terminated 2×1 surface reconstruction. After the flashing, the sample remained in the preparation chamber

for around 5 minutes, allowing the pressure to gradually return to the initial base level. As Si(100) is very reactive, the cleanness of H_2 and D_2 molecules are very important. The gas line was cooled with a liquid nitrogen during this process to minimize the impurities in the gas line, as shown in Fig. 3.2 D.

3.3 Tip and sensor preparation

FM-AFM relies on precise frequency changes to measure force gradients, making the stability of the sensor's frequency crucial. Quartz tuning forks, used in quartz watches, are promising candidates for this application due to their stability in keeping time and their ability to provide an electrical deflection signal with low power requirements [36]. This low power consumption minimizes heat generation, making them optimal for low-temperature operation. However, these tuning forks originally have two oscillating prongs, which can cause issues in AFM due to symmetry breaking when a tip is attached. To address this, the qPlus sensor modifies the tuning fork by attaching one prong to a heavy substrate, effectively creating a single-prong oscillator. This change helps to maintain high precision and reduce problems related to mass imbalance and reduced quality factor [70].

In this thesis, the third generation qPlus sensors with a type of S0.8 and S0.6 [70] that has includes top and bottom electrodes, and side electrodes for differential deflection measurement, and a center electrode for an additional STM channel (see Fig. 3.3 A). The center electrode, where a gold wire is attached using conductive epoxy glue (EPO-TEK H20E), biases the tip for STM operation and can optionally excite the sensor's oscillation. As shown in Fig. 3.3 B, a heating plate is used under the microscope, and the gold wire is held in place with tweezers for precise micro-alignment, followed by immediate heating to harden the epoxy. This procedure is repeated for each gold wire, including those for the AFM and STM patches. To prevent electrical contact between the wires, non-conductive epoxy is applied over the conductive glue after it hardens. Once the wires are attached, the entire sensor is mounted onto the home-built sensor holder, as shown in Fig. 3.3 C, using non-conductive epoxy glue (EPO-TEK H70E). To directly measure lateral forces, the sensor was rotated by 90°, so that it can oscillate parallel to the sample surface, as shown in Fig. 3.3 B [37, 49, 50, 95, 96]. The sensor holder is cleaned with acetone

and isopropanol in an ultrasonic bath to remove contaminants and ensure proper adhesion of the glue. The tungsten wire, which will serve as the tip, is attached and electrochemically etched. The etching was started with a longer wire and the etching station was provided by CreaTec Fischer & Co. GmbH, as shown in Fig. 3.3 D. 2M density of KOH was used as the etching solution. After etching, the tip is rinsed with diluted water and checked under the optical microscope. Tungsten is chosen as the tip material because of its high stiffness. This is important because extending the oscillating arm will decrease the spring constant, and a soft tip wire (because of material and/or geometry) can lead to an overall sensor stiffness that is too low. A custom-built ceramic sensor holder was utilized, featuring three holes through which copper wires pass to connect the sensor electrodes to the STM/LFM head. As shown in Fig. 3.3 E, the holder includes a spring that facilitates in-situ sensor installation. Note that the stiff spring is required for the quality factor of the sensor. Although several home-built springs were tested, they proved ineffective, making the use of a spring from Createc essential. The system's wobble stick is equipped with a fork at the apex designed to securely hold the sensor. Insulated copper wires are connected from top to bottom of the holder, and are connected to the gold balls, which will be electrically connected to the sensor patches. After each assembly step, the conductivity is tested to confirm that the electrical pathways are intact. Fig. 3.3 F shows the LFM sensor sitting in the microscope head.

The microscopic tip apex shape can be engineered on a clean Cu(111) sample partially covered with CO molecules. To modify the tip apex shape, the tip is repeatedly poked into a clean area of the Cu(111) sample [97, 98]. After each poke, the tip is moved to a clean spot on the bare Cu surface in STM feedback to assess its sharpness. Fig. 3.4 A shows STM images obtained with a metal tip having a single-atom apex, and Fig. 3.4 B shows the same area scanned after picking up one CO molecule. The depth of a CO molecule on Cu(111) with a single-atom tip is approximately 45-50 pm in constant current STM image when using a scanning condition of $V_{\mathrm{B}} = 10$ mV and a $I_{\mathrm{set}} = 100$ pA. After this fast check, the tip apex is further characterized using the carbon monoxide front atom identification (COFI) method [54, 55, 99], which determines the number of atoms at the tip apex. Achieving atomic resolution requires a sufficiently sharp tip apex, ideally terminating in a single atom as shown in Fig. 3.4 C. Due to the strong distance dependence of the tunneling current and the short-range tip-sample forces, the tip-sample interaction

is predominantly mediated by the front-most tip apex atom [53].

Additionally, the spatial resolution achieved in STM and AFM experiments can be significantly enhanced by picking up an adsorbate, a process known as tip functionalization [100]. Individual atoms and molecules can be picked up from a surface using vertical manipulation [97, 101, 102]. CO-terminated tips, prepared by picking up a single CO molecule from a surface [60], effectively reduce the chemical reactivity of a single-atom metal tip [52, 100]. The use of CO tips in AFM experiments was first demonstrated by Gross *et al.* in 2009, who achieved atomic resolution imaging of a single pentacene molecule [52].

The CO pickup process used in this work is a modified version of the protocol originally proposed by Bartels *et al.* in Ref. [101]. A single-atom metal tip is placed in STM feedback (feedback settings: $V_{\mathrm{B}} = 1\mathrm{V}$, $I_{\mathrm{set}} = 1\mathrm{nA}$) above an isolated CO molecule adsorbed on a Cu(111) surface. With STM feedback loop on, the bias voltage is increased in 100 mV steps until a sudden drop or increase in the tunneling current signal is detected. An increase in I_{set} indicates lateral manipulation of the CO molecule away from the tip-sample junction, whereas a drop signifies that the CO molecule has hopped to the tip apex. Successful CO tip functionalization is confirmed by a change in the STM appearance of CO adsorbates imaged with either CO or metallic tips, as illustrated in Fig. 3.4 A and B.

Typically, the CO pickup process works best with circularly symmetric single-atom metal tips. The sharpness of the tip apex, indicated by the number of metal atoms in the front-most layer, can be initially assessed from the depth of the CO depressions in the STM topography. While CO molecules appear as approximately 50 pm deep depressions with single-atom metal tips, they appear less deep with blunter metal tips. Additionally, the CO molecule may adsorb at the tip apex in a tilted configuration due to inherent asymmetry of the single-atom metal tip apex. Thus, the tip apex must be characterized at the atomic scale before and after the CO pickup attempt. In this work, tip characterization of metal and CO-terminated tips is performed using the COFI method.

In COFI, the tip is scanned at a constant height above a CO molecule adsorbed on a Cu(111) surface [54, 55]. The COFI method takes advantage of the upright adsorption geometry of individual CO molecules on Cu(111). CO molecules adsorb on top sites with the Oxygen atom pointing away from the surface [103]. The resulting constant-height Δf image, known as the COFI image, reveals the atomic

configuration of the tip apex. Initially, different patterns in COFI images were interpreted as signatures of the crystallographic orientation of various single-atom metal tips [53–55, 99]. In 2015, Emmrich *et al.* performed a reverse experiment by imaging single metal adatoms and small metal clusters on a Cu(111) surface with a CO tip [53]. The constant-height Δf images of metal adatoms and clusters showed similarities to COFI images recorded of different metal tip apices. This led to the conclusion that the number of tip apex atoms in the first atomic layer and their geometric configuration are imaged by the COFI method [53].

The COFI image of a single-atom metal tip, shown in Fig. 3.4 C, presents a circular shape attractive feature (dark) with a repulsive ring (bright) around it. The mirror symmetry comes from the lateral oscillation direction of the LFM sensor. This COFI portrait closely resembles the appearance of single metal adatoms when probed with a CO tip [104]. For successful CO-terminated tip preparation, a symmetric single-atom metal tip is required, which can be confirmed by a circularly symmetric COFI portrait. COFI images of CO-terminated tips are also recorded to ensure successful CO tip functionalization and a circularly symmetric tip apex. With a symmetric CO tip, the surface CO also looks very symmetric, as shown in Fig. 3.4 D. The raw image of the CO molecule with LFM (Fig. 3.4 D) revealed a circular shape with a highly localized depression in the middle [95]. In following chapters, CO-functionalized tip is used to directly image the internal structure of a planar molecule and to characterize chemical bonds.

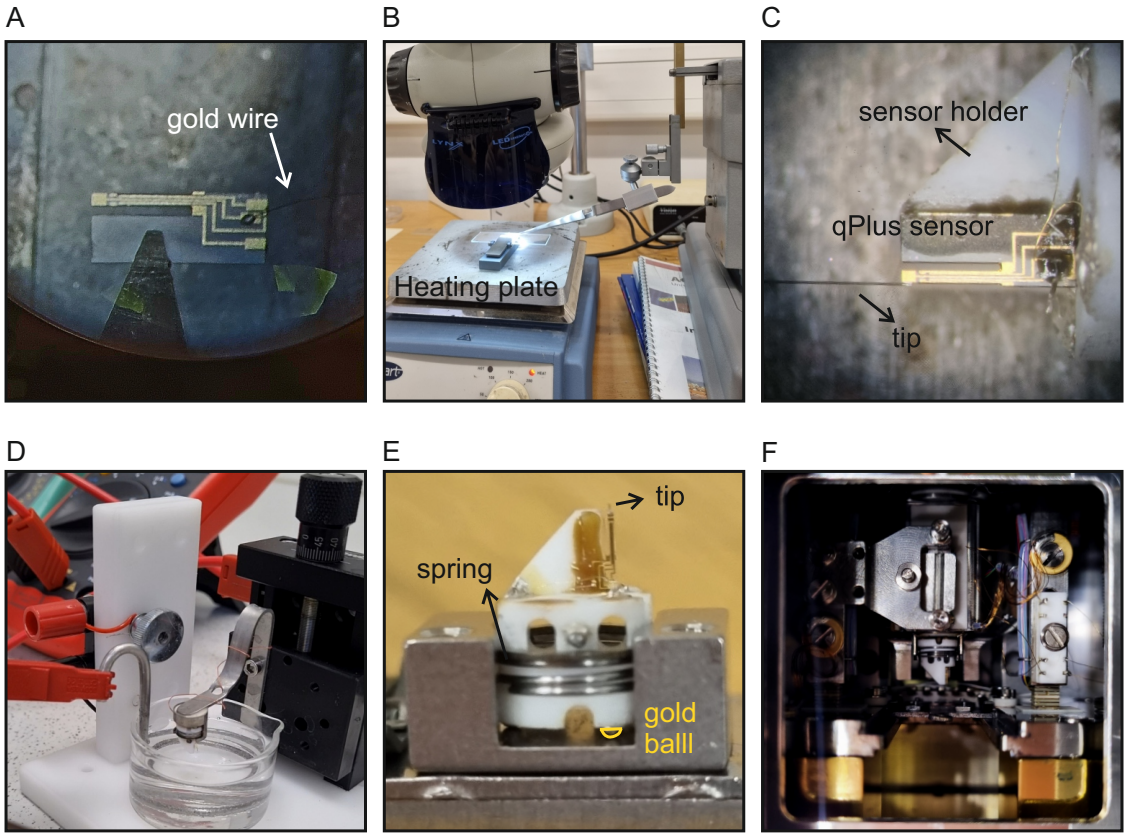

Figure 3.3: Custom-built qPlus sensor. (A) The quartz oscillator with the STM channel contact, where a gold wire is attached using conductive epoxy glue. (B) Micro-alignment of the gold wire under a microscope with tweezers. The alignment was done over the heating plate, allowing direct heating without moving the component after alignment. (C) Sensor (type qPlus S0.8 [70]) mounted onto a custom-built holder using non-conductive epoxy. The sensor has three separate gold electrodes to simultaneously detect the STM and AFM signal. The tungsten tip will be electrochemically-etched after glued with conductive glue to the end of the free prong. (D) Electrochemical etching of the tungsten wire, using 2M KOH solution, to sharpen the tip. The etching station includes a container for the etching solution, a ring-shaped cathode, and a sensor-holding part connected to the anode. During the electrochemical etching process, monitoring the decreasing current flowing through the solution and tip ensures etching process. (E) The sensor holder is assembled with a spring for mounting. The three gold balls underneath the holder are electrically connected to the sensor's contacts through insulated copper wires. (F) The completed LFM sensor positioned in the microscope head.

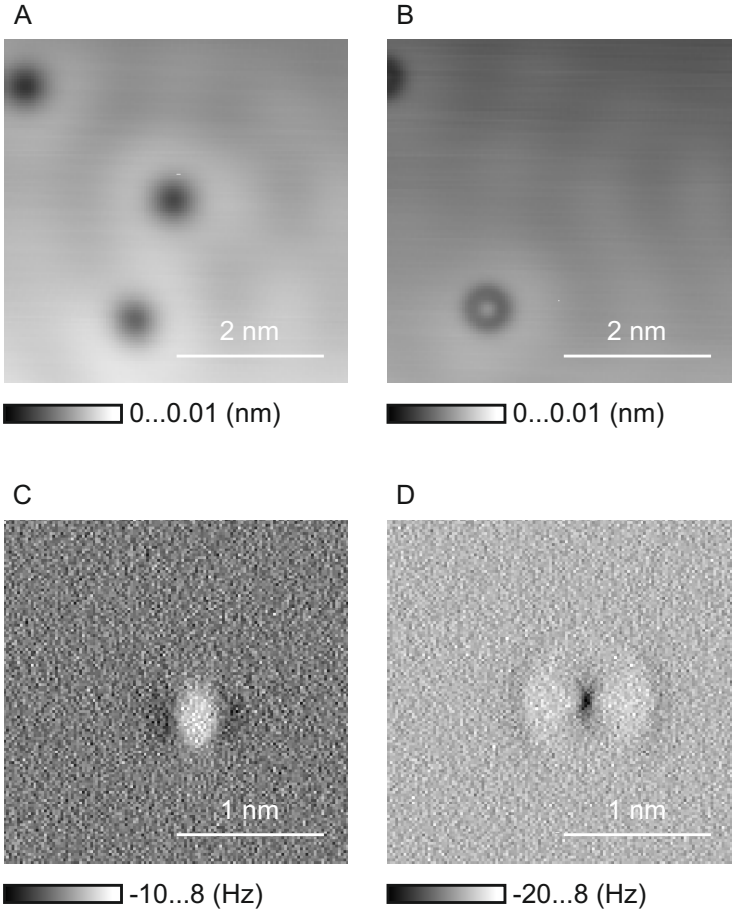

Figure 3.4: COFI process. (A) STM topography image of Cu(111) recorded with a metal tip before CO tip functionalization. (B) STM topography image of the same area as in (A) after picking up the CO molecule. The CO appearance changed with respect to (A). Imaging parameters for both images: $V_{\mathrm{B}} = 100\mathrm{mV}$, $I_{\mathrm{set}} = 50\mathrm{pA}$. (C) LFM Δf image with a single atom tip over CO adsorbate. (D) LFM Δf image obtained over CO adsorbate with a CO tip.

4 Exploring in-plane interaction beside an adsorbed molecule with LFM

Most of the content in this chapter has been published in PNAS [96]. Parts of the text, figures, and interpretations are identical to those in the publication. This work is done with support from the co-authors, Elisabeth Riegel[2], Lukas Hörmann[1], Oliver T. Hofmann[3], Oliver Gretz[2], Alfred J. Weymouth[2], and Franz J. Giessibl[2]. Elisabeth Riegel[2] collected data beside the PTCDA. The code used for the modeling and analysis can be found in the appendix .1.

The resolution and imaging stability in AFM can be significantly enhanced by using well-defined tips, allowing for the scanning of individual atoms and molecules. Traditional AFM/STM experiments often involve gently poking the tip into the sample to create a sharp apex. This process typically results in the apex being covered with a cluster of sample atoms, leaving the tip termination composed of the same material as the sample. Another example of improving atomic-scale contrast involves modifying the tip apex by picking up specific atoms or molecules. Gross *et al.* attached a carbon monoxide (CO) molecule to the tip apex, which was then used to image surfaces [52]. By using this technique, they distinguished between various atoms within a pentacene molecule, a planar structure composed of five

[1]Institute of Solid State Physics, Graz University of Technology, Graz, 8010, Austria; Now at the Institute of Chemistry, University of Warwick, Coventry, CV4 7AL, UK and Institute of Physics, University of Warwick, Coventry, CV4 7AL, UK.
[2]Faculty of Physics, University of Regensburg, Regensburg, 93053, Germany.
[3]Institute of Solid State Physics, Graz University of Technology, Graz, 8010, Austria

benzene-like rings [52]. The CO molecule, being chemically inert and stable, enhances measurement accuracy at short tip-sample distances where repulsive forces dominate. A CO-terminated tip provides a well-defined, atomically characterized apex, facilitating precise and reproducible measurements. However, the flexibility and bending of the CO molecule at the tip apex can complicate image interpretation. The lateral deflection of the CO molecule may result in image distortions and elongated features, emphasizing the importance of understanding the exact characteristics of the probe tip apex.

Since its introduction, the CO-terminated tip has been widely used in this method, making it essential to understand the probe's characteristics for accurate data interpretation and reliable model development. The interaction of a CO-terminated tip with adsorbates has also been extensively studied through theoretical approaches. Early studies concluded that the dominant interaction was Pauli repulsion between atoms [100, 105], which can be well described via empirical potentials [90, 95]. This paved the way for the development of the highly successful Probe - Particle model introduced by Hapala *et al.* [90]. Subsequent AFM investigations of CuN_2 [106] and molecules with strongly polarized groups [107] concluded that the electrostatic interaction between the CO tip and the sample electron density should be considered, revealing that there is a negative charge at the apex of the CO tip. More recently, AFM experiments on ionic crystals with a CO tip showed that the CO tip can have a more complex electric field [108]. The dipole at the metal tip apex (i.e., behind the CO), with a positive pole pointing toward the surface, must be considered to reproduce the measured signal. It is therefore accepted that when imaging charged systems, accounting for the charge at the CO apex and/or the metal dipole is essential for achieving accurate results [106, 108]. However, for weakly polarized molecules, modeling the tip-sample interaction using radially symmetric atomic interactions (e.g., Lennard - Jones or Morse potentials) is generally sufficient to reproduce AFM images [90, 95].

This chapter questions the validity of radially symmetric models as a function of tip height in weakly polarized systems. To do this, an archetypical surface adsorbate, a single adsorbed CO molecule, was used to characterize the CO tip. Data acquisition beside the adsorbed molecule on the surface allowed the probe tip to go closer. LFM [49, 109], in which the tip oscillates laterally across the surface, is an ideal tool to measure in-plane interactions since the recorded frequency shift

Δf is a direct measure of the lateral stiffness. Section 4.1 introduces the procedure of LFM data acquisition and analysis beside the molecule in detail. To explain the data shown in section 4.1, section 4.2 starts by quantifying parameters of an interaction between two CO molecules previously modeled [95] including torsional springs, and empirical potential. The model is then extended by including electrostatic interaction to explain the observed additional feature at lower tip height (beside the molecule). Another system, PTCDA (3,4,9,10-perylene-tetracarboxylic-dianhydride), was studied in section 4.3 to determine if this result can be generalized to weakly polarized systems. In this process, the sensitivity of the LFM is additionally proven by probing single Hydrogen atoms within the PTCDA molecule. This knowledge about the validity of radially symmetric interaction later helps improve the accuracy of friction measurements, which will be discussed in chapters 5 and 6. This leads to more detailed insights into the mechanisms governing friction with single atom resolution.

4.1 Validity of radially symmetric interaction

CO-terminated tips were prepared on a Cu(111) surface and the tip apex was characterized with the COFI method before and after picking up CO via the process described in section 3.3. The background image in Fig. 4.1 shows an LFM Δf image acquired above an adsorbed CO molecule on a Cu(111) surface.The CO-CO interaction results in Δf images characterized by a mirror symmetric circular shape with a highly localized dark feature at the center. The mirror symmetry of LFM images is due to the direction of the sensor's oscillation (same direction as the solid red line), which directly affects the sensitivity of the measurement. The sharp dark feature at the center of the CO results from the LFM techniques high sensitivity of the Δf measurement to changes in the total lateral force. It is reported that this sharp feature was not feasible by using only normal force AFM data [95]. After the tip was prepared and characterized, three-dimensional (3D) data sets were collected above and beside the CO molecule with 5 pm tip-sample distance difference between each slice. Fig. 4.1 shows the schematic concept of the measurement process. All images were acquired in constant height mode with zero bias voltage to prevent crosstalk with tunneling current [110]. The middle

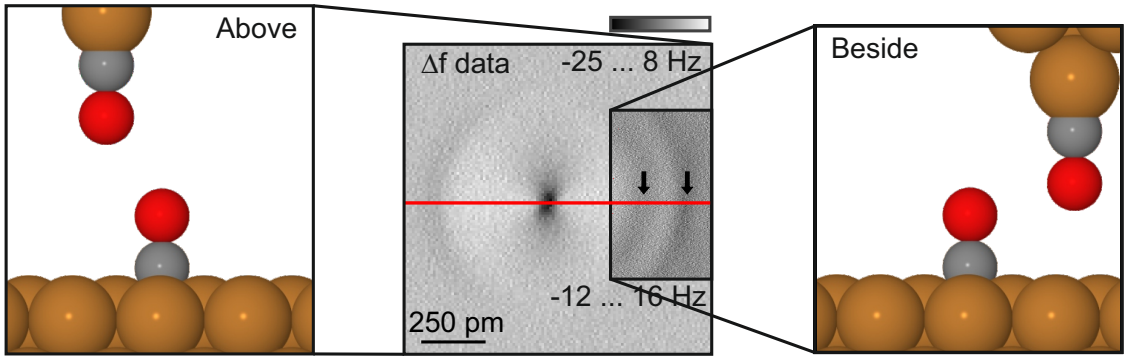

Figure 4.1: Schematic depiction of the system. 3D dataset was acquired above and beside the molecule. Two CO molecules are depicted with Oxygen (red), Carbon (gray), and Copper (ochre) atoms. Constant height LFM images of a CO molecule, scanned with a CO-terminated tip, are shown in the middle.The tip height is 450 pm for the larger image and 320 pm for the inset image. The color scale and length scale are indicated in the figure. At the closer distance shown in the inset, an additional dip appears (marked with black arrows in the figure). The red solid line intersects the center of the CO (the dark feature in the middle) and extends to one side along the direction of tip oscillation.

figure shows raw data of two slices within a 3D data set, taken at $z = 445$ pm and $z = 320$ pm as examples. Below a height of $z = 445$ pm, data must be acquired at the side of the CO adsorbate, otherwise, it will laterally move on the surface. The z-values are defined as the distance between Oxygen of the tip CO and the Cu surface when the CO is assumed to be unrelaxed, taken from theory, which will be discussed later. The background image (acquired above CO) is identical with Fig. 3.4 in section 3.3. LFM image acquired at the side of the CO (inset in Fig. 4.1) reveals an additional dip, highlighted with black arrows.

To physically interpret the interaction between the tip and surface CO, the data along the red line in Fig. 4.1 were extracted for all images in the 3D dataset and converted into lateral force, as shown in Fig. 4.2. Since the extracted Δf line aligned with the direction of the tip oscillation, it could be deconvoluted and integrated to obtain the lateral force in that direction. The lateral force was deconvolved using the Fourier decomposition method for data obtained above the molecule [79], and the Sader-Jarvis method for data collected at the side of the molecule [78]. While the Sader-Jarvis method [78] is commonly used for FM-AFM data to convert the observed Δf data into force and energy, the Fourier decomposition was recently developed considering the physical FM-LFM setup [79]. In general, the Fourier

method is superior for LFM data due to the high number of inflection points but can only be used on data where the opposite sides of the image (defined by the oscillation direction) are the same, as it enforces periodic boundary conditions in the potential energy [79]. This is why Sader-Jarvis method is used for data acquired at the side of the molecule. This process was repeated for various tip-sample distances.

The lateral force on the CO molecule is depicted in Fig. 4.2, which shows the force as a function of both lateral and vertical positions. The lateral force presents an attractive interaction as the CO molecules approach each other, changing to a repulsive interaction when the distance is smaller than the equilibrium distance. Assuming the CO bends to relax, bending is expected at all positions except where the lateral forces are zero. The lateral and vertical positions where the lateral forces are zero were calculated and fit to a circle, as shown in Fig. 4.2. $x = 0$ is defined as the center of the adsorbed CO on the surface, determined by the maximum energy point for each image in the dataset. Since the positions of zero net force correspond to energy minima, the bond length between two Oxygen atoms can be determined. Assuming that the CO molecules do not tilt at these positions, the radius of the circle represents the bond length σ between the two Oxygen atoms. Then, the absolute tip heights can be determined using the measured bond length σ = 340 pm from the data and and the known CO adsorbate length $l_{\mathrm{CO}} = 302\,\mathrm{pm}$ [111]. The z-scale in Fig. 4.2 denotes the calculated absolute heights of the Oxygen atoms at the tip apex above the Cu surface. These heights were determined by fitting a circle to the zero net force points, which are indicated by the white dots.

Above a height of $z = 350\,\mathrm{pm}$, the zero crossings fit well to a circle with a radius of $\sigma = 340\,\mathrm{pm}$. The radius from the circular fit deviates by approximately 11.7 % from the previously reported value of 385 pm [95]. The difference might arise from the different energy convolution method in terms of methodology, and variations in the metal tip apex as a physical factor. Defining the surface normal as 0°, a circular fit is valid up to a large angle of $\alpha = 82°$, as indicated in Fig. 4.2. It means that a radially symmetric interaction of CO-CO interaction (such as a Morse potential) is valid for a rather large interaction angle. In this range, there is attractive interaction outside the zero-crossing circle and repulsive interaction inside the circle, as well-described by a Morse potential. This indicates that the radially symmetric model only becomes invalid at tip heights where measurements beside the molecule are required, since it is no longer possible to acquire images above the molecule

without manipulating the adsorbed CO. The primary question will be then how this angle of $\alpha = 82°$was determined. This is done by evaluating the agreement between experimental data and the model which is discussed in the next section.

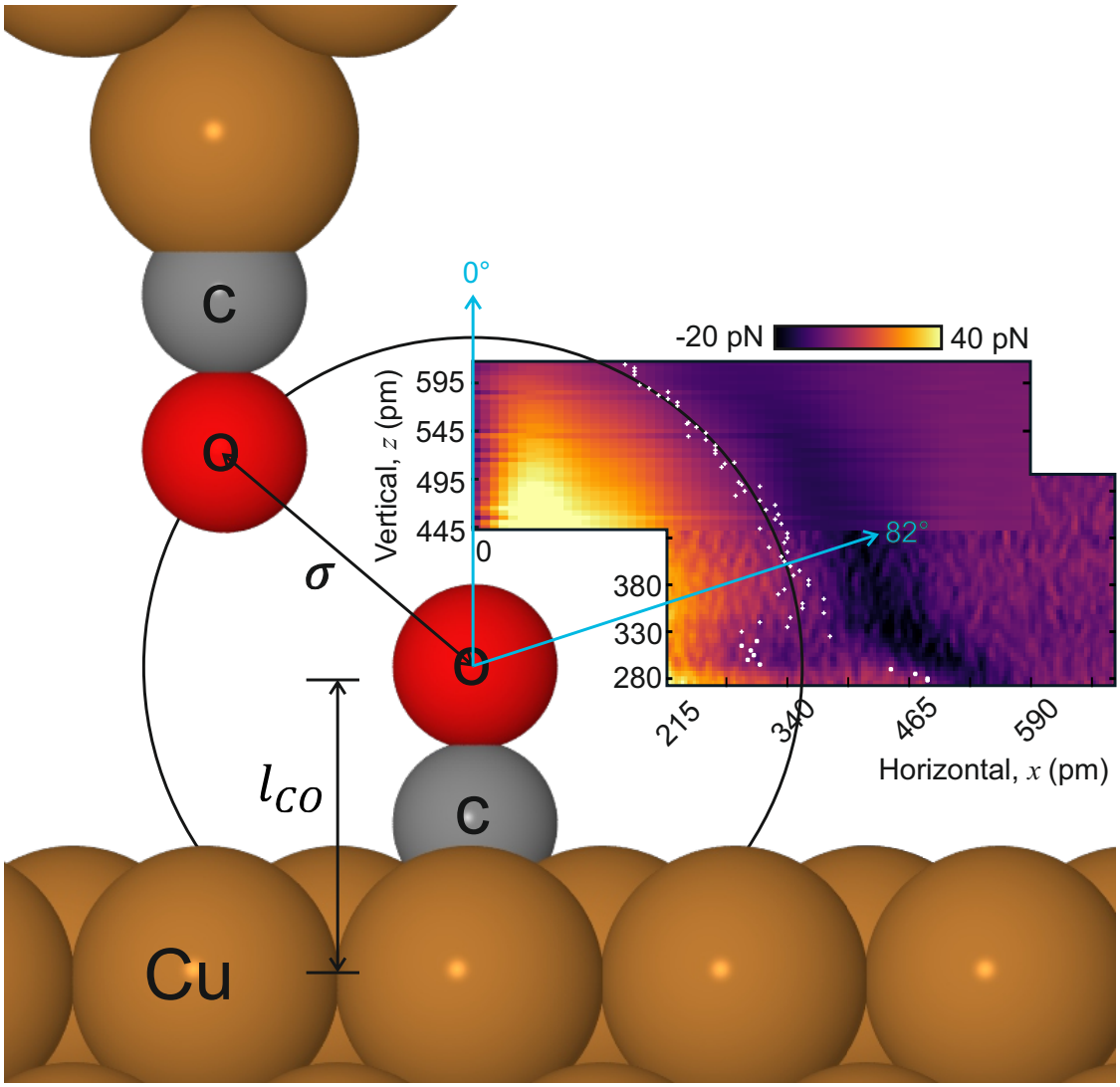

Figure 4.2: Approaching at the side of CO. The lateral force data on the right were obtained by deconvolution at various tip heights along the red line in Fig. 4.1. White dots indicate points of zero lateral force. Above a height of $z = 350\,\text{pm}$, these can be fit by a circle centered on the Oxygen of the sample CO. Going closer, the crossings start to deviate from the circle. The transition point corresponds to an angle of 82°with respect to the surface normal. The bond length (σ) between two Oxygens, $z = 340\,\text{pm}$, and CO length (l_{CO}), 302 pm, are also shown.

4.2 Model simulation

This section will start with a simulation that had previously been very successful in describing the LFM image [95]. Then, the duration for which this model remains valid will be determined, and a new model will be introduced in section 4.2.2 to explain the non-validated regime.

4.2.1 Previous model

The previous model described the interaction between tip and sample only between the two O atoms of the CO molecules as an interatomic interaction, and the CO molecules were allowed to be relaxed as torsional springs with different spring constants. These total interaction can be separated by three components: (i) interatomic interaction described by Morse potential [112] between the two Oxygen atoms, (ii) the relaxation of the tip CO molecule, and (iii) the relaxation of the surface CO molecule. The total energy of the system with the exclusion of any electrostatic interactions, E_{noES} , was therefore:

$$\begin{aligned} E_{\mathrm{noES}} &= E_{\mathrm{Morse}}(E_{\mathrm{B}}, \sigma, \lambda, r) \\ &\quad + E_{\mathrm{Spring}}(k_{\mathrm{T}}, \theta_{\mathrm{T}}) + E_{\mathrm{Spring}}(k_{\mathrm{S}}, \theta_{\mathrm{S}}) \\ &= E_{\mathrm{B}} \left(-2 \exp\left(\frac{-r-\sigma}{\lambda} \right) + \exp\left(-2 \frac{r-\sigma}{\lambda} \right) \right) \\ &\quad + \frac{1}{2} k_{\mathrm{T}} \theta_{\mathrm{T}}^2 + \frac{1}{2} k_{\mathrm{S}} \theta_{\mathrm{S}}^2 \end{aligned} \tag{4.1}$$

The term describing the Morse potential, E_{Morse}, is a function of the bond energy E_{B}, the bond length σ, the decay length λ, and the distance between the atoms r. $E_{\mathrm{B}} = 8.4\,\mathrm{meV}$ and $\lambda = 47\,\mathrm{pm}$ are values previously determined via FM-AFM measurement of $\Delta f(z)$ [95]. σ is determined from Fig. 4.2. The torsional spring constants for the tip CO and the surface CO are $k_{\mathrm{T}} = 22\,\mathrm{zNm}$ and $k_{\mathrm{S}} = 150\,\mathrm{zNm}$, respectively. A moment arm of 302 pm was used for both COs [111]. The CO tilting angles are denoted as θ_{T} and θ_{S}. At each position of the metal tip apex, θ_{T} and θ_{S} are relaxed to minimize E_{noES}.

The schematic of this model is shown in Fig. 4.3 A. With all the required parameters from the previous model known, the mean squared error (MSE) between the model and the data can be evaluated, as shown in Fig. 4.3. The MSE is calculated

by averaging the sum of the squared differences across data points for various tip heights. The MSE values for each tip height are provided in Fig. 4.3. The discrepancy between the model of E_{noES} and the data begin to appear at a height of $z \approx 350\,\mathrm{pm}$, as shown in Fig. 4.3 C. As the tip height decreased, the additional dip in the data becomes deeper, and is no longer fitting the model of E_{noES}. The values of MSE are then plotted as a function of tip height (see Fig. 4.3 B). The point where the error significantly increases, indicated with an arrow at $z = 350\,\mathrm{pm}$, marks the limit where the model becomes invalid.

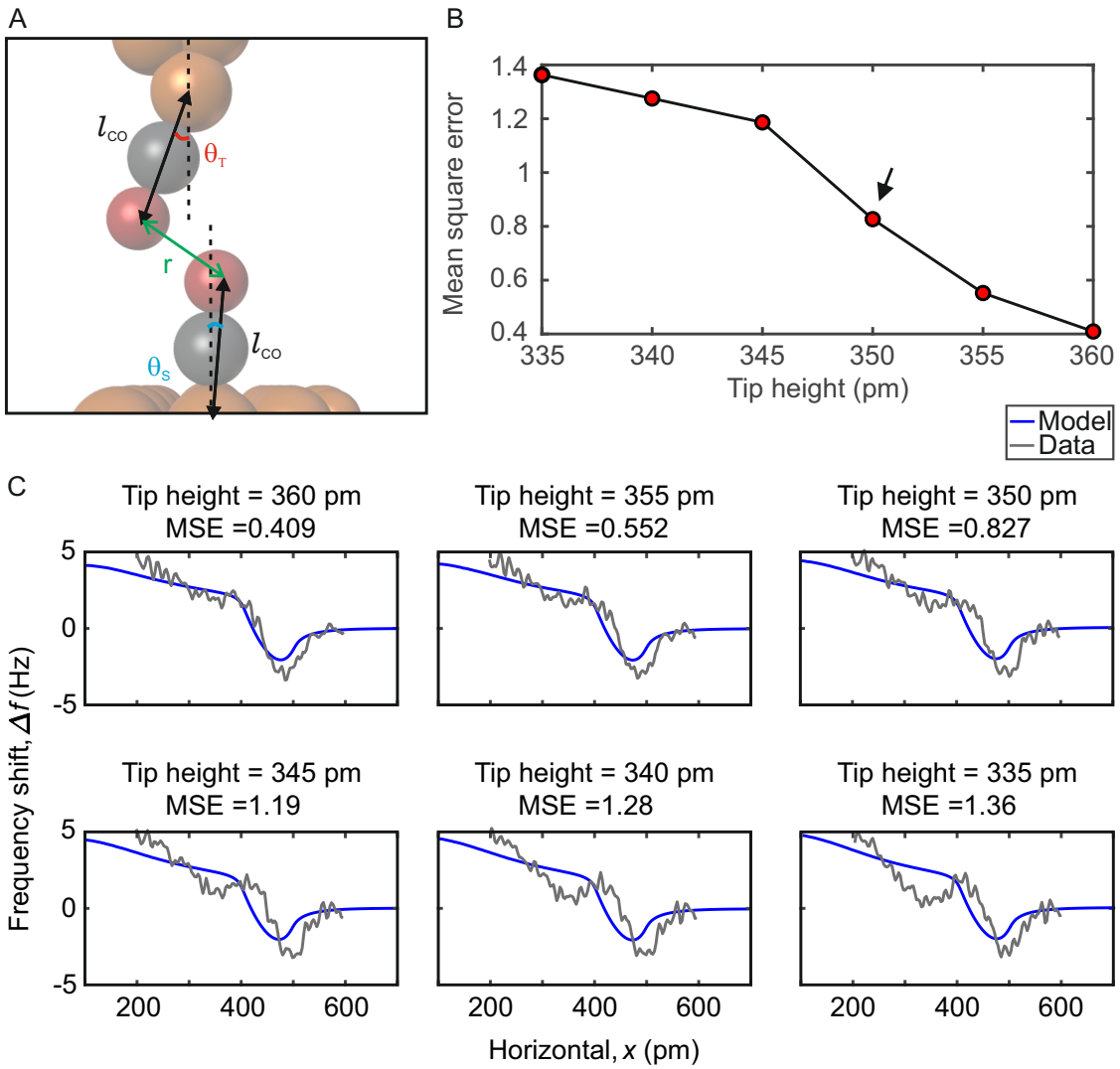

Figure 4.3: Evaluating the accuracy of radially symmetric model with a CO adsorbate. (A) Schematic figure of the model described by E_{noES} [95] (see equation 4.1). The CO molecule at tip side is allowed to relax by an angle θ_{T}, and the surface CO molecule is allowed to relax by an angle θ_{S}. (B) By comparing the Δf data acquired at various heights to a model without electrostatic interactions (E_{noES}), the sum of the squared differences averaged over the number of data points (mean square error, MSE) are calculated. The data used here are identical to those in Fig.4.2 from the parts acquired at the side of the molecule. The MSE is calculated for several tip heights and plotted as a function of tip height. The point where the error starts to substantially increase at $z = 350\,\mathrm{pm}$ is defined as the point where this model is no longer valid. This height corresponds to the angle $\alpha = 82°$, as indicated in Fig. 4.2. (C) Some examples of discrepancies between the data and previous model outputs. Data are plotted in gray, and the model output is plotted in blue. The data used here are identical to those in Fig.4.2 and were acquired at the side of the molecule.

4.2.2 New model with an electrostatic interaction

To explain the additional dip observed, as presented in the inset of Fig. 4.1 and discrepancies shown in Fig. 4.3 C, another interaction should now be considered in the model. Although the system of a single CO molecule on Cu(111) is not highly polarized, the electrostatic interaction between the tip and the CO molecule on the surface is additionally considered, adopting a concept similar to that used in previous studies [106, 108].

The electrostatic potential energy, E_{D}, between two point dipoles $\mathbf{p}_1$ and $\mathbf{p}_2$ is given by:

$$\begin{aligned} E_{\mathrm{D}}(\mathbf{p}_1, \mathbf{p}_2, \vec{r}) &= \frac{k_e \left(\mathbf{p}_1 \cdot \mathbf{p}_2 - 3(\mathbf{p}_1 \cdot \hat{r})(\mathbf{p}_2 \cdot \hat{r})\right)}{r^3} \\ &= \frac{k_e p_1 p_2 \left(\cos\theta - 3\cos\theta_1 \cos\theta_2\right)}{r^3} \end{aligned} \tag{4.2}$$

where $\mathbf{p}_1$ and $\mathbf{p}_2$ are the dipole moments of the two interacting dipoles, having the magnitudes of p_1 and p_2. $\hat{r}$ is the unit vector in the direction of the line connecting the two dipoles, and r is the distance between the two dipoles, and k_e is Coulombs constant. If the dipoles have an angle θ between them, the interaction energy can be expressed in terms of this angle. θ_1 and θ_2 are the angles between each dipole moment and the line connecting the dipoles.

The interaction energy depends on the relative orientations of the dipole moments and their positions with respect to the line connecting them. The term $\cos\theta$ reflects how aligned the dipole moments are relative to each other, while $\cos\theta_1$ and $\cos\theta_2$ adjust for the angles between the dipole moments and the line connecting them. The energy decreases with the cube of the distance between the dipoles, indicating that the effect of dipole-dipole interactions diminishes rapidly as the distance increases. For example, if the dipoles are aligned head-to-tail ($\theta = 0°$), the interaction is generally attractive. If they are aligned side-by-side ($\theta = 90°$), the interaction is typically repulsive.

A schematic figure of this new model is shown in Fig. 4.4 A and B. The position of the metal tip atom, which does not relax, is defined as ($\mathrm{x_{tip}}$, $\mathrm{z_{tip}}$), relative to the Cu atom below the adsorbed CO, which is at (0,0), as shown in Fig. 4.4 A. If the CO bends clockwise relative to its original position, indicated by the dotted line in Fig. 4.4 A, the angle is defined as a positive value for both θ_{T} and θ_{S}. Fig. 4.4 B

illustrates the dipoles considered in the model. On the tip side, there is one dipole located at the Oxygen atom of the CO, denoted as $\vec{P}_{\text{tip}}^{\text{CO}}$, and another at the metal tip apex, denoted as $\vec{P}_{\text{tip}}^{\text{metal}}$. The CO on the surface has one dipole, $\vec{P}_{\text{sample}}^{\text{CO}}$, located at the Oxygen atom of the CO.

Therefore, two dipole-dipole interactions are considered in the new model:
1) between the CO at the tip apex and the CO on the surface, having a distance of $\vec{r}_{\text{O-O}}$ and
2) between the metal tip apex and the CO on the surface, having a distance $\vec{r}_{\text{tip-O}}$.
The total potential energy including electrostatic interaction is:

$$E_{\text{tot}} = E_{\text{noES}} + E_D(\vec{P}_{\text{tip}}^{\text{CO}}, \vec{P}_{\text{sample}}^{\text{CO}}, \vec{r}_{\text{O-O}}) + E_D(\vec{P}_{\text{tip}}^{\text{metal}}, \vec{P}_{\text{sample}}^{\text{CO}}, \vec{r}_{\text{tip-O}}) \tag{4.3}$$

For the calculations, the tip dipole $\vec{P}_{\text{tip}}^{\text{metal}}$ is positioned at the center of the Cu atom, (x_{tip}, z_{tip}), with a magnitude of 4 D as shown in Fig. 4.4 B [113, 114]. $\vec{P}_{\text{tip}}^{\text{CO}}$ is positioned at the center of the Oxygen atom and points toward the Cu atom [108], with a dipole moment of 0.166 D [106]. The free parameters in the model were the dipole moment and dipole direction of the CO on the Cu(111) surface, $\vec{P}_{\text{sample}}^{\text{CO}}$. The second term of equation (4.3), $E_{\text{D}}(\vec{P}_{\text{tip}}^{\text{CO}}, \vec{P}_{\text{sample}}^{\text{CO}}, \vec{r}_{\text{O-O}})$ then include ϕ_1 - θ_{S}, as the angle between the two dipole directions located at O, as shown in Fig. 4.4 B. The third term of equation (4.3), $E_{\text{D}}(\vec{P}_{\text{tip}}^{\text{metal}}, \vec{P}_{\text{sample}}^{\text{CO}}, \vec{r}_{\text{O-O}})$ corresponds to the dipole-dipole interaction between the metal tip apex of the CO-functionalized tip and the CO at the sample. The angle between these two dipoles is ϕ_2 - θ_{S}, as the angle between the two dipole directions as shown in Fig. 4.4 B.

By varying the position of the metal tip apex, (x_{tip}, z_{tip}), the total energy of the system can be calculated as a function of the bending angle of the CO molecules, θ_{T} and θ_{S}. For each tip position (x_{tip}, z_{tip}), the energy is minimized with respect to θ_{T} and θ_{S}, resulting in the energy of the system at that position. The determined bending angle can then be used to obtain the force and force gradient. The force gradient is convoluted with a semicircular weight function to account for cantilever motion and multiplied by $\frac{f_0}{2k}$ to explicitly determine Δf, which can be directly compared with experimental data.

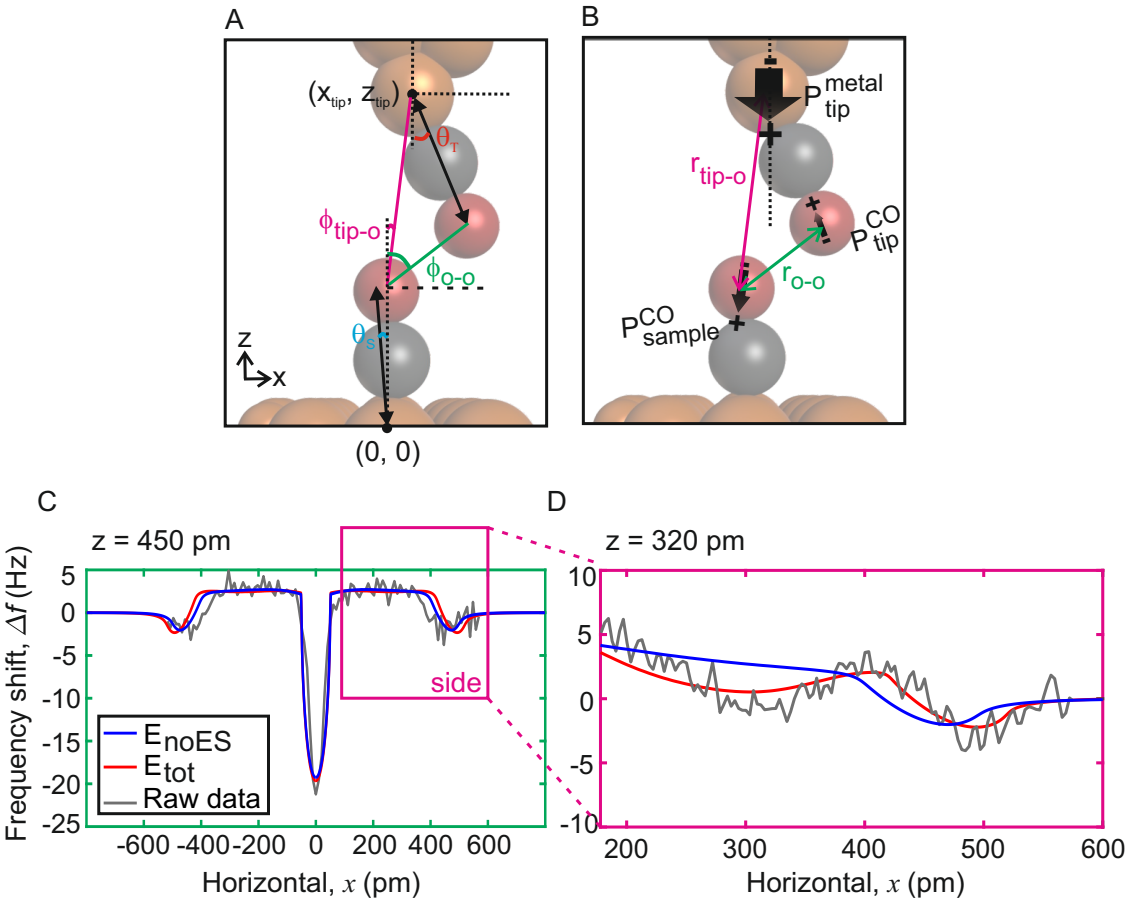

Figure 4.4: New model description. (A) Definition of the angles used in the model. The position of the metal tip atom, which does not relax, is defined as (x_{tip}, z_{tip}), relative to the Cu atom below the adsorbed CO, which is at (0, 0). θ_{S} is a tilt angle of the surface CO from +z, which is defined as th1 in the appendix .1. θ_{T} is the tilt angle of the CO on the tip from -z, which is defined as th2 in the appendix .1. Then, the angle between the two COs can be defined as $\theta_{\mathrm{S}} + \pi - \theta_{\mathrm{S}}$ (defined as th3 in the appendix .1). $\phi_{\mathrm{O\text{-}O}}$ is the angle between the dipole moments located at the Oxygen atoms, and $\phi_{\mathrm{tip\text{-}O}}$ is the angle between the dipole moment at the metal tip apex and the Oxygen atom of the surface CO molecule. $\phi_{\mathrm{O\text{-}O}}$ and $\phi_{\mathrm{tip\text{-}O}}$ can be obtained by the known distances between the dipoles, as shown in Fig. (B). (B) Definition of the distances and the directions of the dipoles in a new model, E_{tot}. The tip has two dipoles, one at the O-atom ($\vec{P}^{\mathrm{CO}}_{\mathrm{tip}}$), allowed to tilt, and one at the metal tip apex, $\vec{P}^{\mathrm{metal}}_{\mathrm{tip}}$. $\vec{P}^{\mathrm{metal}}_{\mathrm{tip}}$ points toward the surface with a 4 D dipole moment. $\vec{P}^{\mathrm{CO}}_{\mathrm{tip}}$ has a negative pole at the O-atom with a 0.166 D dipole moment [106]. (C) A line scan through the center of the CO molecule at $z = 450$ pm and (D) a line scan at the side of CO at $z = 320$ pm. Gray line is raw data, red line is model output with an electrostatic interaction, and blue line is model output without an electrostatic interaction. Model output has an additional dip at the lower tip height, $z = 320$ pm, only with electrostatic interaction as shown in (D).

Then Δf is calculated as a function of height and lateral distance. Fig. 4.4 C and D show the comparison between experimental data and model output at two representative tip heights in the direction of the tip oscillation, along the red line in Fig. 4.1. The data were plotted as gray lines. For the higher tip height, at $z = 450\,\mathrm{pm}$ (Fig. 4.4 C), the additional dip is not present. Both the E_{noES} model and the E_{tot} model agrees well with the data.

Good agreement with the data was obtained with a dipole moment of the CO on the surface pointing toward the surface with a value of 0.8 D, as shown in Fig. 4.4 B. This means that the dipole is asserted to be in the opposite direction to what has previously been proposed [115]. However, sensitivity in the model is likely limited to the interaction at the very apex of the CO molecule on the surface, and the actual charge distribution is likely very complex [108, 114]. It is possible that the dipoles at the tip (both metal and CO) change as a function of tilt, as well as due to the proximity of the nearby CO molecule on the surface. Likewise, the dipole of the surface CO could change. Nevertheless, the model with fixed (static) value of dipoles for the metal tip and both CO molecules is sufficient to explain the additional dip in the measurement, where the E_{noES} model fails.

By separating the contributions of each force component considered in the model, the contrast change and the emergence of the additional dip at lower tip heights can be explained, as shown in Fig. 4.5. At $z = 450\,\mathrm{pm}$, where the image was scanned above the entire CO and do not observe the additional dip, the total force is dominated by the Morse interaction with a maximum force of 40 pN. The electrostatic interaction between the metal tip apex and the CO on the surface plays only a small role with a maximum magnitude of 8.0 pN. The CO-CO dipole interaction has an even smaller effect with a maximum magnitude of only 1.0 pN. Therefore, and not surprisingly, the total interaction can be well described only with a Morse potential at these distances. Also, note that the metal tip-CO dipole interaction is much larger than the CO-CO dipole interaction.

Approaching to the surface, the tilting angles of the COs increase [90, 116] and the saddle points toward the minima of the potential energy surface become sharper as shown in Fig. 4.5B. At $z = 320\,\mathrm{pm}$, which is a height where an additional dip was observed in the image, the Morse force component is more than twice as big with a maximum value of 90 pN. However, the total force has a narrower repulsive region beside the adsorbed CO compared to the larger tip-sample distance. The dipole

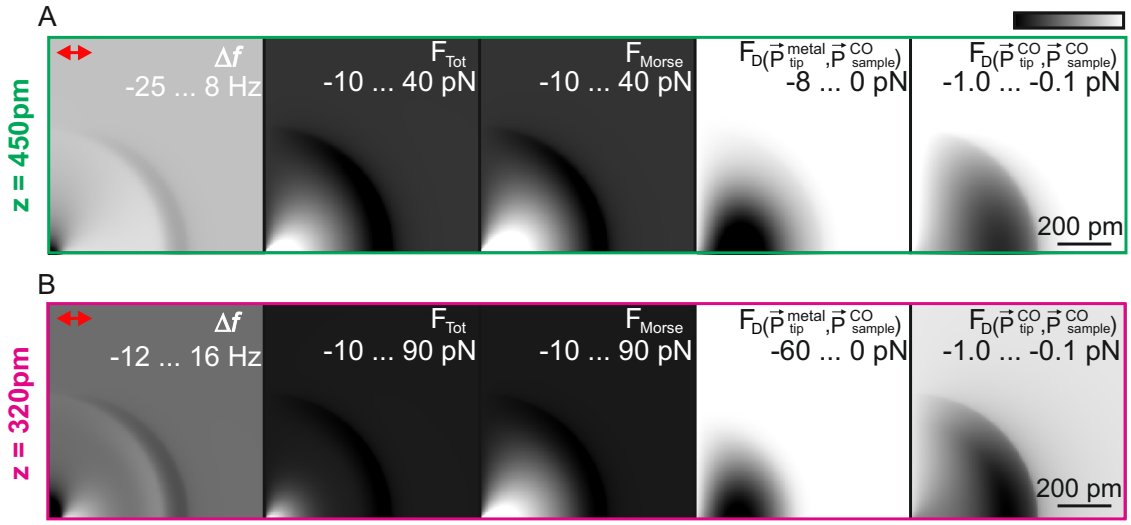

Figure 4.5: Force contributions with the new model. Δf and force decomposed images in terms of the interactions are shown for (A) $z = 450\,\text{pm}$ and (B) $z = 320\,\text{pm}$. The main contribution of the total force comes from the Morse interaction for both tip heights. The parameters of the Morse interaction are given in the main text. However, for small distances (B), the contribution from the metaldipole interaction is also significant and is the origin of the additional dip in the Δf images. The red arrow shows the tip oscillation direction.

interaction between the metal tip and surface CO has also substantially increased and has a maximum magnitude of 60 pN at $z = 320\,\text{pm}$. In comparison, the dipole-dipole interaction between the CO molecules shows a maximum magnitude of only 1.0 pN.

Therefore it is shown that the dominant dipole-dipole interaction is again between the metal tip apex and the adsorbate, where the relative magnitude of this metal tip-adsorbate dipole interaction, the main factor of the additional dip, becomes comparable with the Morse contribution at the closer distance. To prove that the additional dip does not come from the interaction between the two COs acting as dipoles, Fig. 4.6 A-C shows a simulation ignoring the metal tipadsorbate interaction, $E'_{\text{tot}} = E_{\text{noES}} + E_D(\vec{P}^{\text{CO}}_{\text{tip}}, \vec{P}^{\text{CO}}_{\text{sample}}, \vec{r}_{\text{O-O}})$ This result does not show the additional dip.

Additionally, the interaction ignoring the electrostatic interaction between the CO molecules, $E''_{\text{tot}} = E_{\text{noES}} + E_D(\vec{P}^{\text{metal}}_{\text{tip}}, \vec{P}^{\text{CO}}_{\text{sample}}, \vec{r}_{\text{O-O}})$, is simulated to confirm that the additional dip is mostly from the metal tip dipole, as shown in Fig. 4.6 D-F. Moreover, the model did not show the additional dip when the direction of the CO dipole on the sample is changed, as shown in Fig. 4.6 G-I. Therefore, it is concluded

that the additional dip appears only in the case of 1) the existence of the metal tip dipole and 2) the negative pole of the sample CO dipole at its Oxygen apex, which is allowed to be tilt in the model.

The tilting behavior of the CO has a strong influence on the scanned image features since the tilted angle of COs increases as they get closer to each other (the direction of close to Horizontal, $x = 0$), as shown in Fig. 4.7 A-C. These angles are the values generated during the simulations process of the Fig. 4.4 C and D. If the CO bends clockwise relative to its original position, as indicated by the dotted line in Fig. 4.7 A, the angle is defined as a positive value. Therefore, for the case of Fig. 4.7 A, both θ_S and θ_T have negative value of angles as they are rotating to the counterclockwise relative to their original position. Note that the original positions of the two CO molecules are different. When the two COs are far from each other ($x \approx 600\,\text{pm}$ for both tip heights), the tilted angles θ_S and θ_T are zero. As the COs get closer ($x \approx 450\,\text{pm}$), θ_T increases because the attractive term of the Morse potential dominates over other interactions in this regime, for both tip heights, as shown in Fig. 4.7 B and C. As the distance decreases further, towards $x = 0$, θ_T bends counterclockwise, as repulsive interactions become dominant. The CO at the tip apex is bent at a larger angle compared to the sample CO due to its smaller stiffness. While θ_S does not change much in Fig. 4.7 B, at a closer tip height, θ_S shows a significant increment and decrement, as shown in Fig. 4.7 B, due to the influence of the attractive interaction with the metal tip dipole.

Further comparison between this new model, E_{tot}, and the experimental data are shown in Fig. 4.7 D and E. The image contrast regime is consistent between the simulation image and the data, as indicated in the figures. This provides a clear explanation of the model output with precise values and its comparison with experimental data across various tip heights.

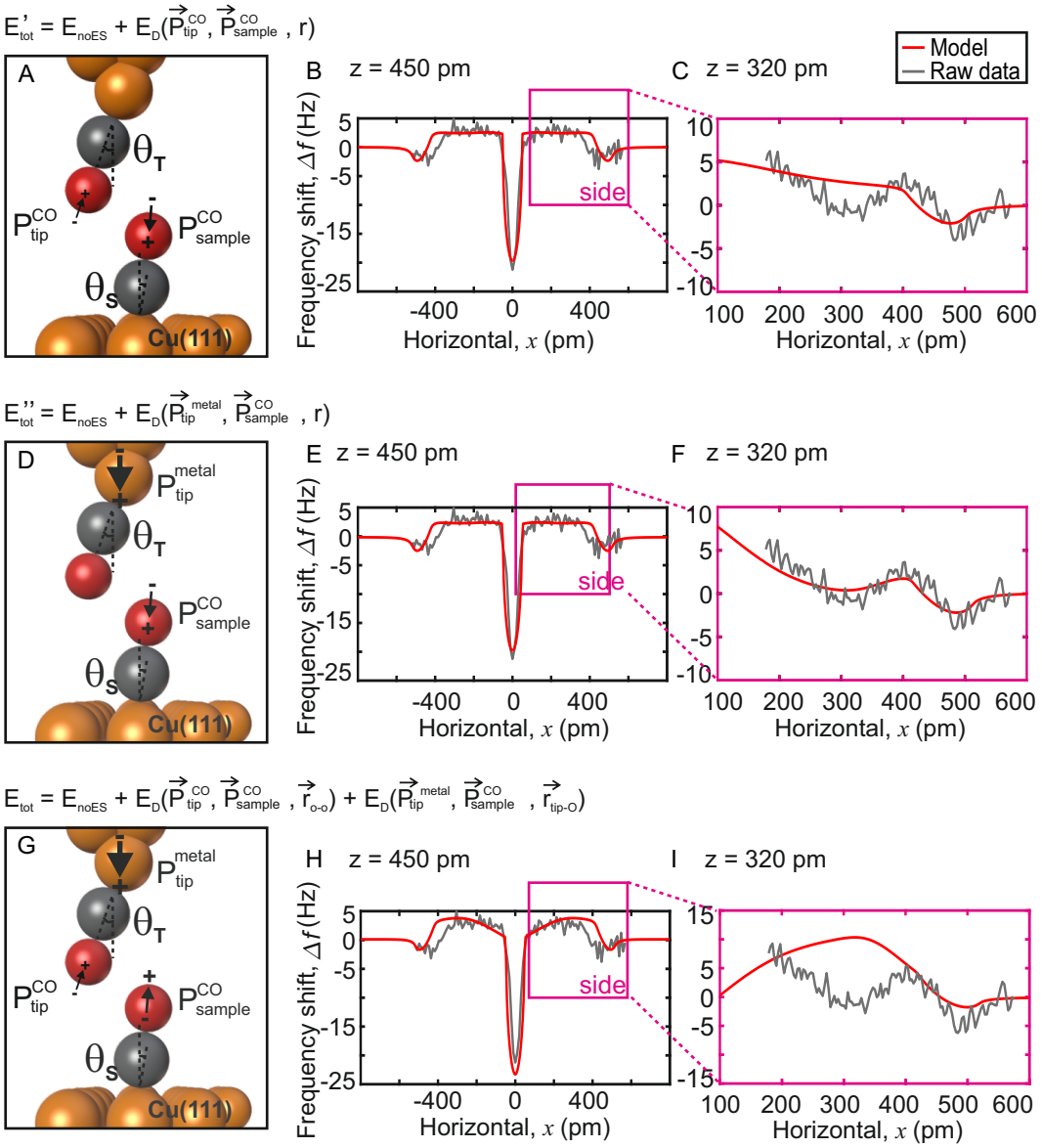

Figure 4.6: Additional trials with the CO-CO model. To prove that the additional dip is mainly from the metal tip apex, three more cases are simulated. (A) Schematic of the model ignoring the metal tip dipole. (B) Simulation and experimental data at $z = 450\,\text{pm}$ agree well. (C) The simulation at $z = 320\,\text{pm}$ does not show the additional dip observed in the data. (D) Schematic of the model ignoring the dipole of the CO at the tip. (E) Simulation and experimental data at $z = 450\,\text{pm}$ agree well. (F) Simulation and experimental data at $z = 320\,\text{pm}$ agree well, implying that the tip CO dipole is not significant in these measurements. (G) Schematic of the model with the sample CO having a dipole moment in the opposite direction. (H) The simulation and experimental data at $z = 450\,\text{pm}$. (I) The simulation at $z = 320\,\text{pm}$ does not reproduce the second dip.

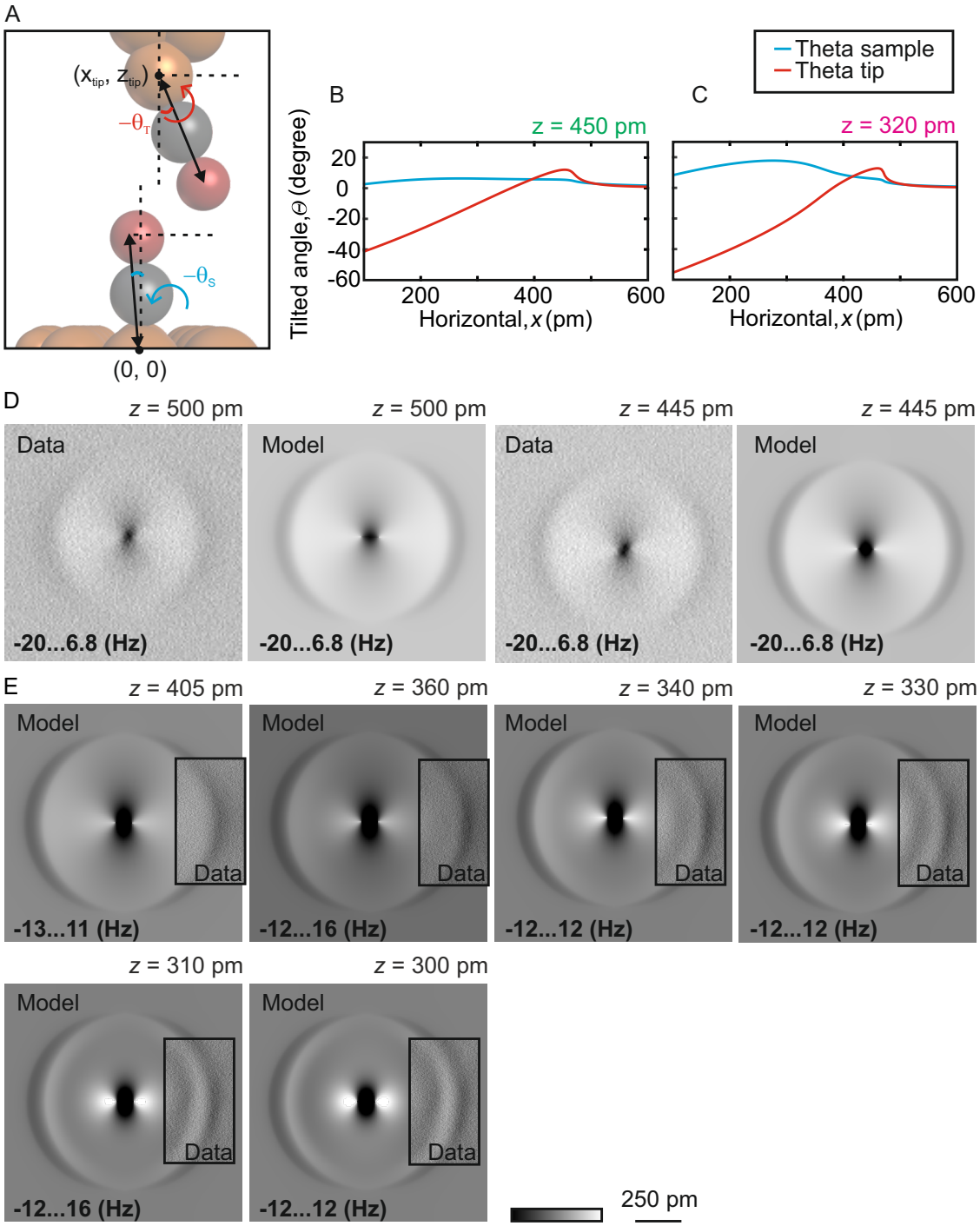

Figure 4.7: CO relaxation angles. The tilting angle of the COs are extracted from the simulation at each tip height. (A) Definition of the bending angle, θ_T and θ_S. The x-axis is defined same as in other figures ($x = 0$) corresponds to center of the CO on the surface), for (A)-(C). The angle of the CO at the tip, θ_T, side is plotted with a red color, and the angle of the CO at the sample, θ_S, side is plotted with a sky blue color for both tip heights. (B) The tilt angle at $z = 450$ pm. (C) Tilt angles at $z = 320$ pm. (D)-(E) Further comparison between simulation results and experimental data for various tip heights. The image contrast regime is identical, as indicated in the figures.

4.3 In-plane interaction beside the PTCDA molecule

In section 4.1, it is shown that LFM is ideal for measuring in-plane interaction and short range interactions. The data is explained well with a simple model introduced in section 4.2. The large angle of the radially symmetric interaction is validated with a previous model [95]. Furthermore, the additional feature is fit via a new model (see section 4.2.2) [96]. This indicates that, contrary to formal expectations [106, 115, 117], induced electrostatic interactions through the metal tip must be accounted for, even in weakly polarized systems.

To more generally validate the observed influence of the metal dipole at the tip apex [108], another weakly polarized system, PTCDA (3,4,9,10 - perylenetetracarboxylicdianhydride), is investigated in this section. PTCDA is a good test sample because it has a stable and planar molecular structure that forms a well-ordered mono layer, making it easy to get 3D data sets beside the molecule without manipulating the molecule [118, 119]. Additionally, the mechanism of Hydrogen atom spatial resolution could be unveiled.

PTCDA forms a Hydrogen-bonded, herringbone-like structure when adsorbed on Cu(111) at room temperature [120]. Fig. 4.8 A shows a Δf LFM image of the edge of a self-assembled PTCDA molecular island on Cu(111), measured with a CO-terminated tip in constant height mode. In the Δf image, the internal structure of the molecule is visible, with the inner five rings corresponding to the perylene core of the molecule. The spatial contrast is particularly strong over carbon bonds that are perpendicular to the oscillation direction ($\pm$ x-direction in Fig. 4.8 A). Image contrast inside the C_6 rings is relatively even at this height, z = 600 pm, showing that PTCDA lies approximately flat on Cu(111) [119]. At the height at which this image was acquired, inside the C_6 rings, the signal appears relatively constant.

To investigate the lateral interaction of the CO with the sides of the adsorbed molecules, 3D data sets were acquired over a z range of $z = 460$ pm to 600 pm with a vertical spacing of 10 pm in the regions indicated by the black rectangles in Fig. 4.8 A. These regions were chosen because one is closer to the O-side of a PTCDA molecule and the other is closer to the H-side. Fig. 4.8 B is a schematic figure of the measurement process. The starting height of 3D measurements is denoted as $z = 600$ pm. This z-value describes the unrelaxed height of the O atom of the tip. Tip height $z = 0$ pm is defined as the average height of the nuclear positions of the

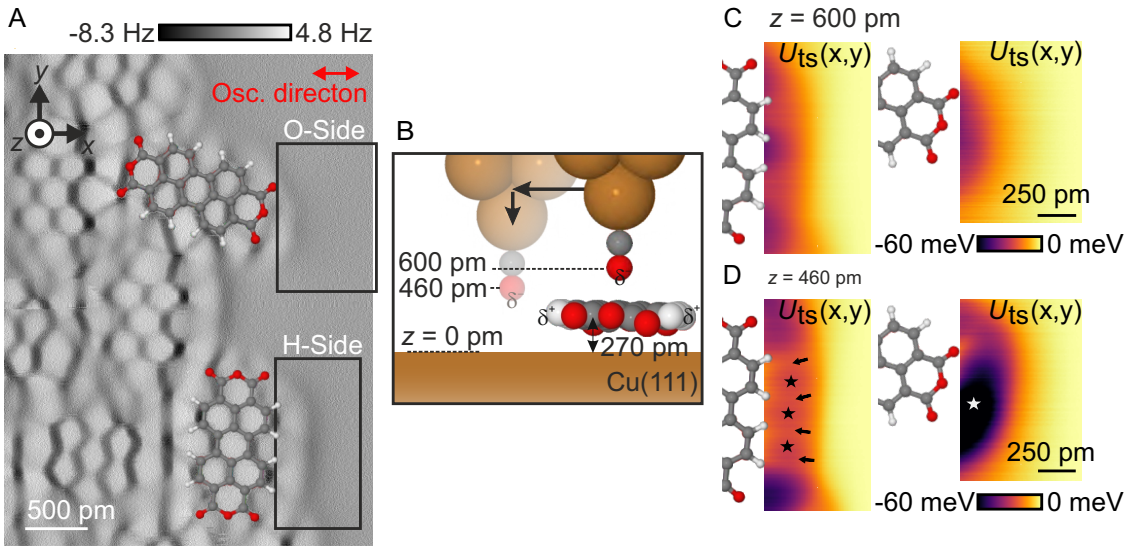

Figure 4.8: Experimental observations of PTCDA on Cu(111). (A) Constant height Δf LFM image of the side of a PTCDA island probed with CO-terminated tip. This imaging height is referred to as $z = 600\,\mathrm{pm}$. The oscillation direction of the sensor is along the $\pm x$-direction. The oscillation amplitude was 50 pm. Ball and stick models of two PTCDA molecules are shown with Oxygen (red), Hydrogen (white), and Carbon (gray) atoms. The schematic figure of the tip heights is shown in (B). At the side of the island, over the areas indicated by black boxes near the H-side and O-side of PTCDA molecules in (A), Δf images were collected at lower heights. The negative partial charge at the CO tip apex is indicated by $\delta-$, and the positive partial charge at the H-side is indicated by $\delta+$. (C) Potential energy maps at the H-side and at the O-side at $z = 600\,\mathrm{pm}$. The color bar and the scale bar are the same for both sides. (D) Potential energy maps at the H-side and at the O-side at $z = 460\,\mathrm{pm}$. The color bar and the scale bar are the same for both sides. Stars and arrows, indicating local potential energy minima and maxima, are discussed in the main text.

Cu(111) surface atoms. The atoms of the PTCDA molecules are found on average $z = 270\,\mathrm{pm}$ above the top surface plane of Cu atoms via theoretical simulation, as will be discussed later. This is very similar to the previously reported height of 268 pm [119].

Acquired Δf data were then converted to potential energy, U_{ts}, by deconvolution along the direction of the tip oscillation (i.e. in-plane) using the Sader-Jarvis method [78]. At the height of $z = 600\,\mathrm{pm}$, similar magnitudes of potential energy are observed on both the H-side and O-side, as shown in Fig. 4.8 C. When the tip approaches lower, the potential energy map on the H-side at $z = 460\,\mathrm{pm}$ shows three local minima marked by stars in left column of Fig. 4.8 D. They have a magnitude

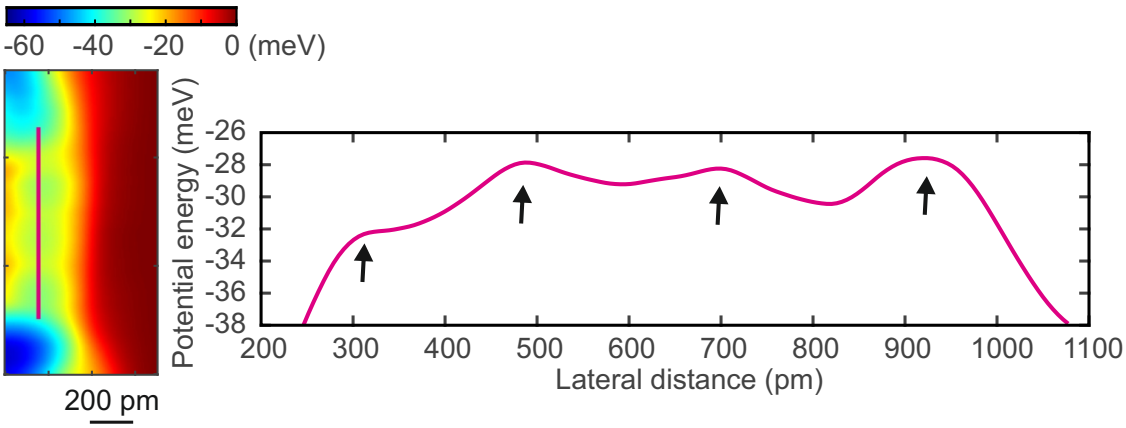

Figure 4.9: Location of the H atoms from experimental data. A linescan in the potential energy map shows the locations of the four hydrogen atoms, indicated by arrows. The potential energy is calculated from the obtained Δf data via Fourier method [79]. Data was acquired at the tip height of $z = 460$ pm.

of approximately -30 meV and are separated by lines of higher potential energy of approximately -28 meV indicated by arrows. The increased potential energy corresponds to the positions of the four individual Hydrogen atoms. A linescan of these data is shown in Fig. 4.9, illustrating the individual features. These observations of local potential energy maxima over the positions of H-atoms show that LFM can clearly identify the position of H-atoms via Pauli repulsion on a flat-lying organic molecule.

On the O-side, however, there is much stronger attraction of approximately -70 meV, as shown in Fig. 4.8 D. In other words, the attractive interaction between the CO-terminated tip and the O-side of the molecule is significantly larger than that of the H-side. Considering the relatively negative Oxygen at the tip apex [106], it was expected to form a weak hydrogen bond with the Hydrogen atoms on the H-side. Thus, the stronger attraction observed on the O-side was unexpected. This observation underscores the need to consider the interaction between the metal tip apex and the CO on the surface, as discussed in the previous section 4.2.2. At this height, even though PTCDA is not a strongly polarized system, the influence of the metal tip's dipole may need to be factored into the analysis [108].

To further understand this, the system and the tip-sample interaction are modeled based on DFT calculations. DFT simulations were performed using a PBE exchange-correlation functional [121] and the TSsurf van der Waals correction scheme [118,

122] to determine the relaxed atomic positions of PTCDA on a Cu(111) surface. To focus on the side site of a molecular island, the system was modeled with two PTCDA molecules in a large supercell.

The unit cell of the calculations is shown in the Fig. 4.10 A, including the heights of all Oxygen atoms. A non-planar adsorption geometry had been previously proposed by the x-ray standing-wave technique [119], and the DFT results indicate that the molecules do not lie perfectly flat. This explains why the data at the O-side in Fig. 4.8 D do not appear mirror-symmetric around the long axis of the PTCDA molecule: The white star in Fig. 4.8 D shows the location of the energy minimum on the O-side which does not perfectly correspond to the location of the Oxygen atom. The PTCDA molecules were placed in a herringbone arrangement and at a distance of approximately 1 nm between the H-side of one molecule and the O-side of another, before the two molecules were allowed to fully relax. To gain more insight into the electrostatic interaction, a Mulliken charge decomposition on the PTCDA is determined, as shown in Fig. 4.10 B. The Mulliken charge decomposition will be explained later. The two molecules are in total slightly negatively charged by -0.21 e. The Oxygen atoms are negatively charged, while the Hydrogen atoms become slightly positively charged. The Carbon atoms to which the Hydrogen atoms are bonded receive a small negative charge. Based on these observations, it can be concluded (given that atomic charges are not directly observable) that the negative sign of the electrostatic potential results from the overall negative charge distribution within the molecules. Although Hydrogen atoms exhibit a small positive charge, this charge is likely balanced by the minor negative charge on adjacent Carbon atoms and the stronger negative charge on the Oxygen atoms. Charge decomposition further clarifies the effect of the electrostatic potential when moving laterally along the O-side towards the molecule's backbone. Specifically, beyond the molecule, the negatively charged Oxygen atoms provide electrostatic attraction, whereas within the molecule, the total potential encompasses the influence of the positively charged Carbon atoms.

Then the atomic positions obtained by DFT are used to calculate the expected LFM Δf signal using a model very similar to the Probe-Particle model introduced by Hapala *et al.* [90]. At each position of the metal tip atom, we sum the interactions of all PTCDA atoms with the O atom at the tip apex. As a starting point, the tip-sample interactions are described solely by Lennard-Jones empirical functions to

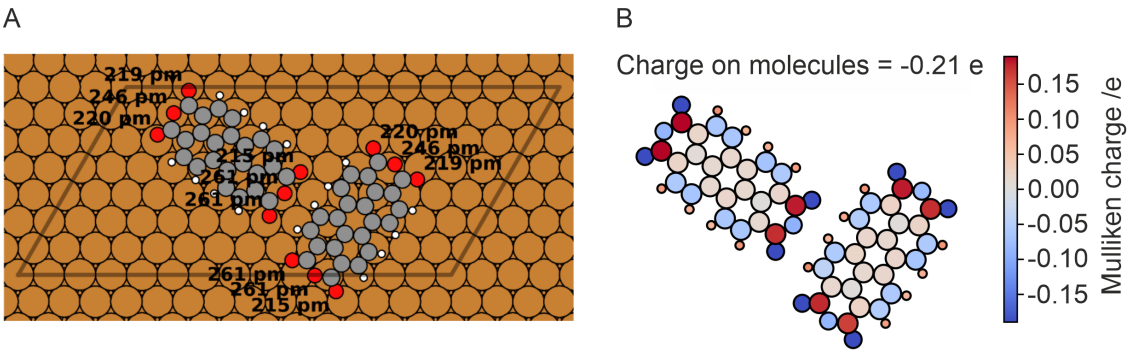

Figure 4.10: Calculated features of PTCDA molecules on Cu(111). (A) Calculated structure of PTCDA molecules on Cu(111). Unit cell of the relaxed atomic positions of two PTCDA molecules on a Cu(111) surface from DFT calculation. Oxygen (red), Hydrogen (white), Carbon (grey), Copper (gold) atoms are depicted with circles. The heights of the O-atoms above the Cu plane are indicated for each atom. (B) Mulliken charge decomposition on the PTCDA molecules adsorbed on the Cu(111) surface. Cu surface not explicitly shown.

determine whether the increased attraction near the O-side is purely due to van der Waals forces. The CO molecule is then allowed to relax to minimize the potential energy, and the lateral forces on the tip are calculated. This process is repeated for 64 different positions of the tip apex during the oscillation cycle. This model has two notable distinctions from the Probe-Particle model [90]:

1. The oscillation direction of the tip is set to be lateral in our model, allowing for a more straightforward comparison between theory and experiment.

2. The code directly outputs the potential energy, U_{LJ}, facilitating a more direct comparison between theory and experiment.

To determine the corresponding z-value in the simulations for the experimental tip height, simulated LFM images are compared with experimental data. Fig. 4.11 A shows a simulated LFM image at the height that most closely matches the experimental results shown in Fig. 4.8 A ($z = 600\,\mathrm{pm}$). At closer distances, the Δf signal is no longer constant within the C_6 rings. The calculated potential energy maps at the heights $z = 600\,\mathrm{pm}$ and $z = 460\,\mathrm{pm}$ (corresponding to the determined experimental heights) are shown in Fig. 4.11 C, E, and G ($z = 600\,\mathrm{pm}$) and Fig. 4.11 D, F, and H ($z = 460\,\mathrm{pm}$). The calculated area is indicated by the black box in Fig. 4.11 A. The LFM simulation can output the potential energy landscape as a result of purely

Lennard-Jones interactions at various heights. Since LFM is not sensitive to vertical forces, the comparison to theory is straight forward and does not require a subtraction of long-range interaction. The calculated potential energy near the O-side and H-side at $z = 600\,\mathrm{pm}$, shown in Fig. 4.11 C, considering only Lennard-Jones interaction (U_{LJ}), agrees well with our observations in Fig. 4.8 C. At $z = 460\,\mathrm{pm}$, the positions of the individual H-atoms on the H-side can again be clearly observed via repulsive interaction. This is further proof that LFM is indeed directly observing H-atoms at the sides of the PTCDA as a result of Pauli repulsion, as no electrostatics are included in U_{LJ}. However the attractive potential energy calculated near the O-side and H-side based only on Lennard-Jones interactions, shown in Fig. 4.11 D, appears very similar. This is in stark contrast to the observations shown in Fig. 4.8 D where there is much stronger attraction near the O-side. This indicates that there is another tip-sample interaction that must be taken into account. One possible mechanism that can explain these observations is the influence of the large dipole of the metal tip apex [113] as previously discussed with CO-CO interaction.

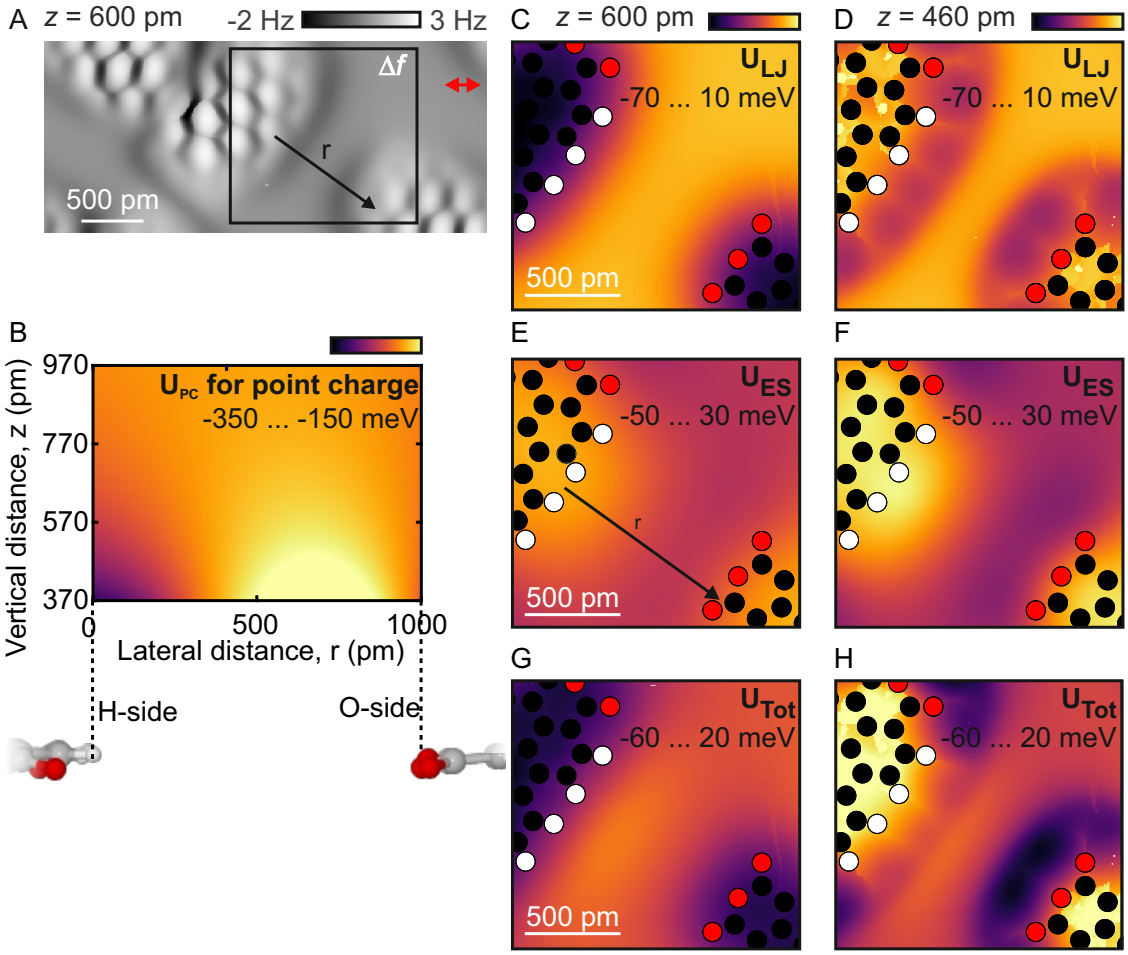

Figure 4.11: Modeling of the sides of a PTCDA molecule. (A) Δf calculated from the DFT relaxed positions of a PTCDA pair with a supercell chosen so that there is 1 nm between two neighboring adsorbates. (B) Electrostatic potential energy from the DFT calculations of an electron as a function of lateral distance r (defined in (A)) and height. (C) Map of the potential energy contribution from Lennard- Jones interactions of the area marked in (A) at a height of 600 pm, (D) as (C) but for a height of 460 pm. (E) Electrostatic potential energy contribution from a metal tip 250 pm above the imaging plane of the area marked in (A) for a height of 600 pm. (F) As (E) but for a height of 460 pm. (G and H) Sum of the upper two panels.

From the DFT calculations, the electrostatic potential energy experienced by a single electron, $U_{\mathrm{PC}}(\vec{r})$, is obtained, as shown in Fig. 4.11 B. This enables the calculation of the electrostatic potential energy experienced by the metal tip dipole,

U_{ES}. The relevant heights are presented in Fig. 4.11 E and F.:

$$U_{\mathrm{ES}}(\vec{r}) = [U_{\mathrm{PC}}(\vec{r}) - U_{\mathrm{PC}}(\vec{r} - \delta z\hat{z})] \left(\frac{|\vec{p}_{\mathrm{tip}}|}{q_{\mathrm{e}}\delta z} \right) \tag{4.4}$$

where δz is the spacing between vertical slices from the DFT output, and q_{e} is the elementary point charge. U_{ES} is calculated at a height of $\vec{r} = \vec{r}_{\mathrm{tip}} - 0.5\ \hat{z}$, where $\vec{r}_{\mathrm{tip}}$ is the location of the apex metal atom of the tip, as previously suggested [108]. However, the previous investigations have shown that this magnitude can vary significantly depending on the shape of the metal tip [114]. For this calculation, a metal tip dipole with a magnitude of $|\vec{p}_{\mathrm{tip}}| = 3\,\mathrm{Debye}$, which is consistent with values reported in the literature [108, 113, 115], produced results that agree well with our data. The sum of U_{ES} and U_{LJ} is shown in Fig. 4.11G and H.

At a height of $z = 600\,\mathrm{pm}$, the additional U_{ES} contribution does not significantly change the contrast of the overall potential energy landscape. In other words, the electrostatic contribution from the metal tip apex does not strongly affect the LFM contrast at a typical imaging height. This has also been observed in general for FM-AFM data [117]. At the closer tip height of $z = 460\,\mathrm{pm}$, the total calculated potential energy, $U_{\mathrm{Tot}} = U_{\mathrm{LJ}} + U_{\mathrm{ES}}$, agrees very well both quantitatively and qualitatively with LFM observations (compare Figs. 4.11 I to 4.8 D). Here, there is clearly more attraction at the O-side. Near the H-side, the four lines of increased potential energy that correspond to the four Hydrogen atoms can also clearly be seen.

As shown in Fig. 4.11 B, the contribution of the electrostatic interaction increases the closer the approach is to the molecular plane. A priori, it was not clear what the dominant interaction terms would be: the van der Waals attraction and Pauli repulsion, modeled by Lennard-Jones interactions; the electrostatic interaction of the dipole from the metal apex; or the electrostatic interaction from the CO at the tip. To estimate the interaction of the dipole moment of the CO, the potential energy of a 0.166 D dipole moment was calculated [106], pointing in the z-direction at 600 pm and 460 pm, shown in Fig. 4.12.

At $z = 600\,\mathrm{pm}$, the contribution has a magnitude of 5 meV and is negligible. At 460 pm,the contribution is also much smaller than the electrostatic interaction from the metal apex. Therefore, we conclude that the electrostatic interaction with the dipole from the metal apex of the tip as well as CO bending, and van der Waals attraction and Pauli repulsion are the significant contributions to the total

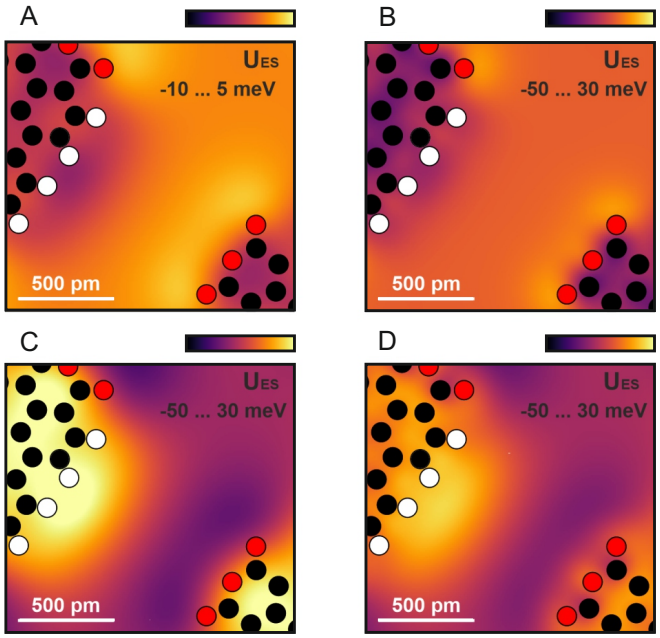

Figure 4.12: Interaction of the dipole moment of the CO. The potential energy of a CO at tip apex, having a dipole moment of 0.166 D, pointing in the z-direction for a tip height of (A) $z = 600$ pm and (B) at $z = 460$ pm. CO was not allowed to be tilt at this simulation therefore the calculated values could be overestimated. (C) The potential energy of a metal dipole for a tip height of $z = 460$ pm. (D) Sum of the metal dipole interaction + CO dipole interaction for a tip height of 460 pm. The metal dipole is located 50 pm lower from the core of the tip atom.

interaction when the tip approaches closer beside an organic adsorbate.

4.4 Discussion

In section 4.1, imaging of a single CO molecule revealed that a radially symmetric description of the atomic interactions is valid for a large angle of 82° from the surface normal, corresponding to a solid angle of 5.4 sr. Generally, when imaging over weakly polarized systems, it suffices to consider CO bending and the short-range attraction and repulsion, which can be modeled by torsional spring and the empirical radial functions such as Morse or Lennard-Jones potentials. However, when approaching closer to gain insight into the in-plane interactions, the electrostatic interaction with the metal dipole cannot be neglected, as shown in section 4.2.2. Previous work has noted the importance of the metal dipole with FM- AFM for strongly polarized materials and molecules [107], including defects in ionic crystals [108] and hexagonal boron nitride [114]. However, it is commonly accepted that for normal AFM measurements of molecular adsorbates on metal surfaces, the effect of the metal tip can be ignored [117]. Throughout the chapter, it is shown that when investigating in-plane interactions, this effect must be considered with both a single CO adsorbate and PTCDA.

Furthermore, the mechanism of H atom imaging was unveiled in section 4.3. Hydrogen, the smallest and most abundant element in nature, plays a vital role in many molecular interactions. Their positions can determine the interactions with neighboring molecules in the form of Hydrogen bonds. While atomic force microscopy can image the internal structure of flat lying molecules, H atoms are difficult to directly image due to their size. Kawai *et al.* were able to directly observe H atoms by carefully choosing a nonplanar molecule so the H atoms pointed out perpendicularly from the surface [123]. While Peng *et al.* were not able to directly identify the location of H atoms of flat lying water molecules via their repulsive signature, they made use of the strong dipole of the water molecule to determine their positions [124]. Unfortunately, neither of these strategies is generally applicable to identify the positions of H atoms terminating the sides of flat lying (approximately planar) molecules. Section 4.3 introduce a new strategy to investigate H atoms at the sides of flat lying molecules. LFM data were collected beside the molecule at heights that are inaccessible when performing constant height imaging above the molecule. Each H atom were observed, clearly showing their locations via Pauli repulsion. LFM, in which the AFM sensor is modified so that the tip oscillates

laterally above the surface [49] and is only sensitive to the lateral component of the force on the tip [51, 125, 126]. A lateral oscillation means that the recorded frequency shift is a direct measure of the lateral forces, which have strong contrast at the terminal edges of planar molecules. It also remains in the plane where these interactions are maximum, in contrast to normal AFM in which a vertical oscillation moves it out of the plane of interest. Interestingly, a previous study with normal AFM where data were collected at the sides of molecules [127] did not report the observation of H atoms but did report imaging instabilities that were attributed to the strong lateral forces that normal AFM is not directly sensitive to. Therefore it is an ideal tool to probe short-range in-plane interactions that have strong lateral force components [109].

5 Sliding friction over single chemical bonds

Most of the content in this chapter has been submitted. Parts of the text, figures, and interpretations are identical to those in the submitted manuscript. This work is done with support from the co-authors, Lukas Hörmann[1], Oliver Gretz[2], Oliver T. Hofmann[3], Franz J. Giessibl[2], and Alfred J. Weymouth[2]

The study in chapter 4 focused on the sensitivity of LFMs in-plane molecular interaction measurements, enabling the imaging of individual H atoms. This can be expanded by exploring interactions beyond conservative forces. In this chapter, the CO-terminated tip, along with the quantized understanding from the previous chapter, has been used to observe dissipative lateral forces, referred to as friction. The advantage of frequency modulation mode, with its additional feedback that keeps the oscillating amplitude constant, allows for the simultaneous and separate measurement of both conservative and non-conservative interactions (see section 2.2.1).

Most friction is well described through established laws, but when it comes to the molecular or atomic scale, friction becomes a complex phenomenon governed by interactions between individual atoms and molecules. This has significant implications for the fields of nanotechnology, where components operate at dimensions where atomic interactions dominate, and for surface science, where the precise control of friction can lead to innovations in lubrication and material performance. Sliding friction, specifically, is influenced by a variety of factors, including the

[1]Institute of Solid State Physics, Graz University of Technology, Graz, 8010, Austria; Now at the Institute of Chemistry, University of Warwick, Coventry, CV4 7AL, UK and Institute of Physics, University of Warwick, Coventry, CV4 7AL, UK.
[2]Faculty of Physics, University of Regensburg, Regensburg, 93053, Germany.
[3]Institute of Solid State Physics, Graz University of Technology, Graz, 8010, Austria

nature of the surfaces in contact, their relative orientation, and the microscopic features of the surface, such as roughness and atomic-scale irregularities.

One intriguing approach to studying friction at the atomic level is to focus on single chemical bonds. These bonds, which represent the most fundamental interactions between atoms, can provide a clear and detailed understanding of the mechanisms driving friction. This approach not only enhances our understanding of atomic-scale friction but also sheds light on the relationship between bond strength, bond order, and frictional behavior. In this context, the study of sliding friction over single chemical bonds is not just a scientific curiosity but a crucial step toward enhancing frictional control in advanced material systems.

This chapter is dedicated to exploring the phenomenon of sliding friction over single chemical bonds using a specific model system, PTCDA on Cu(111), with several key factors that make it particularly suitable for this study. First, PTCDA is a stable molecule that exhibits consistent behavior during LFM measurements, as demonstrated in prior studies [56, 96]. This stability is crucial for obtaining reliable and reproducible data when investigating friction at the atomic scale. Second, the Cu(111) surface provides an optimal balance between reactivity and inertness, which is essential for conducting precise measurements. The surface's characteristics allow for the effective use of a CO molecule to characterize the metal tip apex through the COFI method (see section 3.3). This method ensures that the metal tip ends in a single atom, which is necessary for making a similar functionalized tip [53].

In the gas phase, PTCDA is planar, and it adsorbs approximately flat on the Cu(111) surface. This flat adsorption reduces the complexity associated with bond tilt in the normal direction. Moreover, PTCDA incorporates a variety of chemical bonds, including intermolecular hydrogen bonds (O⋯H) and intramolecular covalent bonds (C - C). This creates a diverse array of covalent bonds with varying bond orders, providing unique features to study friction as a function of both in-plane angles and bond order. Notably, one of the Oxygen atoms in the PTCDA molecule forms a bond with the Cu(111) surface, resulting in the buckling of the bond, which reveals another interesting point.

The chapter is structured as follows: section 5.1 provides an introduction to the PTCDA/Cu(111) system, highlighting its suitability for studying sliding friction at the atomic level. This section also introduces the key concepts and techniques used

to measure energy dissipation across various chemical bonds. section 5.2 delves into the methodology for calculating the energy dissipated over each bond during sliding. This includes a detailed explanation of the computational approach employed using DFT and a machine learning system. Finally, section 5.3 highlights the relationship between energy dissipation and bond order by combining the results from sections 5.1 and 5.2.

5.1 Mapping sliding friction over single chemical bonds

In frequency-modulation LFM, as described in section 2.2.1, the amplitude of oscillation is set, and the drive signal required to maintain this amplitude is recorded. If the drive signal increases, it indicates that there is energy loss during the tip's oscillation, referred to as energy dissipation [36]. Energy dissipation (E_{diss}) represents the work done on the cantilever during one oscillation cycle and is measured in units of meV/cycle. This signal is recorded separately from the frequency shift (Δf, unit of Hz), which reflects the conservative interaction between the tip and the sample. Dissipation can be caused by various forces acting on the tip as it moves forward and backward direction during a single oscillation cycle [56, 128]. While this hysteretic behavior has been previously reported in systems with various mechanisms [129–132], a notable example of LFM work is the snapping model demonstrated by Weymouth *et al.* through the functionalization of the tip apex [56]. To measure dissipation accurately, it is crucial to understand the characteristics of the driven surface, which, in this case, is a CO-terminated tip. The snapping model explains the physical mechanism of dissipation by describing how the CO molecule, when driven to slide laterally over a pair of atoms or a chemical bond, behaves like a torsional spring. It stores energy as it stretches over the bond and releases it when it snaps back during each oscillation cycle. The snapping model describes the physical mechanism of dissipation when the CO molecule is driven to slide laterally over a pair of atoms or a chemical bond between two atoms. The CO molecule, pulled by LFM, behaves like a torsional spring as it stretches over the bond and then snaps back during each oscillation cycle. The behavior of the CO as a torsional spring is discussed in the previous chapter 4, and this chapter expands

on that discussion with the snapping model.

Fig. 5.1 A shows the basic concept of the snapping model. The model assumes that both the surface atoms and the metal tip atoms, except for the CO molecule at the apex, remain static. The position of the metal atom at the tips apex is fixed, while the tip oscillates laterally in space. In the middle of Fig. 5.1 A, the total lateral force is plotted for various lateral distances from the chemical bond over one oscillation cycle. The horizontal-axis represents the position of the metal tip relative to the chemical bond, which is located at $x = 0\,\mathrm{pm}$. As the metal tip moves, the potential energy landscape changes until the CO molecule snaps down. At certain positions, there are two local low-energy solutions. However, the CO molecule at the tip does not always find the thermodynamic minimum solution. To observe energy dissipation, the CO at the tip must be trapped between two surface atoms. Therefore, at each position, the model calculates the low-energy angle of the CO molecule at the apex based on its previous position, relaxing only to the local energy minimum rather than the global one.

During the simulation, the metal apex is moved step wise across the surface. At each step, the CO tip adopts an equilibrium deflection angle. The force resulting solely from the interaction between the tip and the surface (excluding the torsion spring) is then calculated [90]. Energy dissipation is determined by convolving the force $F(t)$ acting on the CO tip with the phase of the oscillation. This energy dissipation signal is detectable only within a narrow range of a few tens of picometers [51, 56], while atomic resolution in Δf data can be acquired over tip heights of hundreds of picometers [133]. As dissipation starts to occur at much lower heights, the CO molecule at the tip apex is easily lost if the tip is brought too close to the surface. The criteria for losing a CO molecule at the apex also vary depending on the specific tip apex geometry, showing that the method outlined in section 3.3 is crucial for making a stable and symmetric tip.

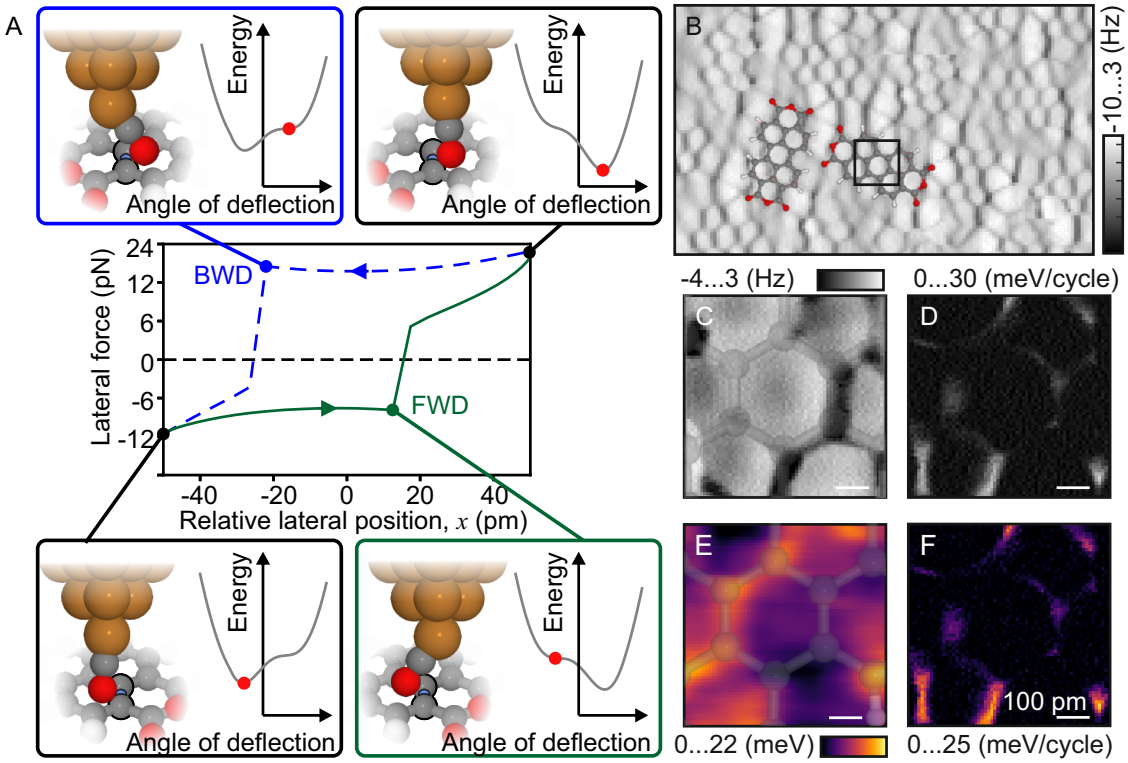

Figure 5.1: Sliding friction over a single chemical bond. (A) A functionalized tip oscillating laterally forward and backward over a single covalent bond (blue feature between two C atoms) can be used to measure the corresponding energy dissipation. At each relative lateral position of the metal tip apex, the CO bends (exaggerated in the sketches). As it does, depending on the sliding direction, the Oxygen atom at the apex can be trapped. The area enclosed in the hysteresis loop is the energy dissipated as the tip oscillates over the bond. (B) LFM Δf image of a PTCDA island. Raw data of (C) Δf image and (D) the simultaneously measured excitation image, obtained over the area outlined in (B). These images are then converted to (E) potential energy (E), and to (F) dissipated energy (E_{diss})

The sample preparation procedure is the same as that used in chapter 4. The Cu(111) sample was cleaned using standard sputter and anneal cycles, and PTCDA molecules were deposited from a home-built evaporator. CO molecules were then leaked into the chamber to functionalize the tip with a CO molecule. Before and after the CO pickup, the tip was checked using the COFI method [53].

Fig. 5.1 B shows a LFM (Δf) image acquired with a CO-functionalized tip over an island of PTCDA molecules. The ordering of PTCDA on Cu(111) appears to be herringbone, which describes a lattice with a unit cell involving two molecules, as shown in Fig. 4.10 in section 4.3. While this seems accurate for nearby molecules, a

true supercell that includes the underlying substrate cannot be observed in the Δf image. Incommensurate layers have also been previously reported [134]. Hydrogen bonds between adjacent molecules and covalent bonds within the molecules can be directly identified via the Δf image. Fig. 5.1 C and D show raw data of a Δf image and the simultaneously measured excitation image. These images are then converted to potential energy (E) via the Fourier method [79], as shown in Fig. 5.1 E, and to dissipated energy (E_{diss}) via the method described in section 2.2.1, as shown in Fig. 5.1 F. Interestingly, the magnitude of both E and E_{diss} are not uniform across the molecules, which also means they are not always consistent over the chemical bonds. While the E_{diss} acquired by the driving signals clearly indicate the locations of the bonds, the raw data cannot perfectly avoid random background noise, as shown by gray plot of Fig. 5.2 A. To minimize this effect, data were acquired as two lines along both the backward and forward scanning directions. These four lines of data were then averaged, and the 2D images, as a function of tip height, were filtered using a Gaussian filter with a standard deviation of 0.5 pixels (the black line of Fig. 5.2 A). The filter was applied using a square Gaussian kernel. The lateral distance is same with Fig. 5.2 B, 300 pm. Fig. 5.2 B shows data acquired as a function of lateral (x) and vertical (z) position of the tip over the area indicated by the red line in Fig. 5.2 C ($z =$ -3 pm).

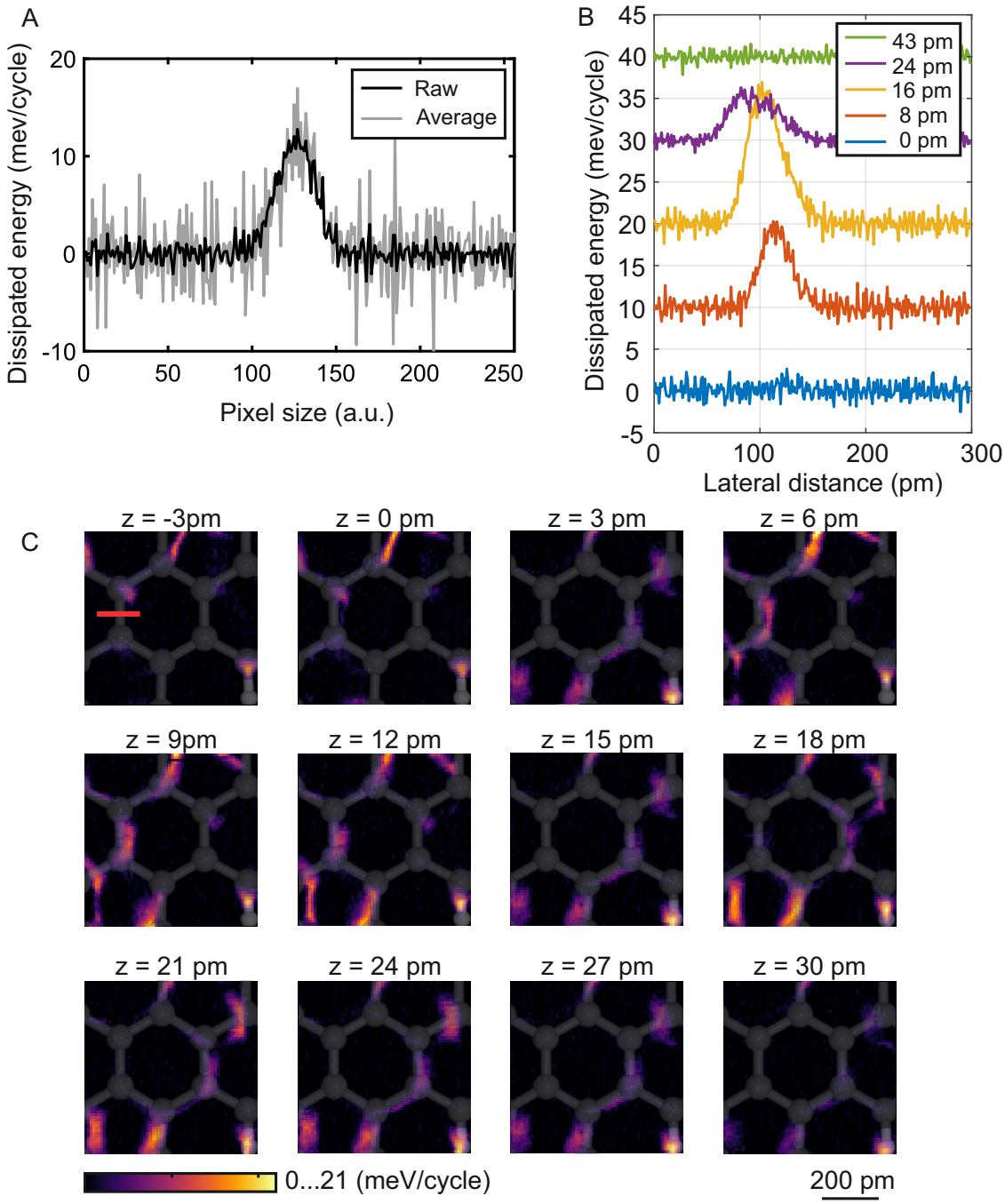

Figure 5.2: Data acquisition and analysis. (A) Comparison between raw data (gray) and averaged data (black). Two lines of data were acquired for both forward and backward scanning directions consisting of 256 pixels. These four lines of data were then averaged, and the 2D images, as a function of tip height, were filtered using a Gaussian filter with a standard deviation of 0.5 pixels. The filter was applied using a square Gaussian kernel. (B) Over each bond, energy dissipation data are measured as a function of lateral and vertical position. Curves at different relative heights (Δz) are offset by 10 meV/cycle for clarity. The acquired position is indicated in the first figure of (C) as a red line. (C) E_{diss} images for each tip height, corresponding to the same location as in Fig. 5.1 C.

The labeled height is a relative height, defining z= 0 pm as the point just before E_{diss} completely disappears. E_{diss} begins to appear as a peak over the chemical bond and increases as the tip approaches closer (from green to yellow in Fig. 5.2 B), and starts to decrease at even smaller distances (from yellow to blue). This strong distance dependence is related to the width of the hysteresis loop (Fig. 5.1 A) and the height of the energy barrier as the tip approaches the bond [56]. The increased width of the hysteresis loop causes the CO molecule to store more energy before it is released. Once the tip gets too close, the CO can no longer snap over with each oscillation cycle, causing E_{diss} to decrease.

The 3D data of E_{diss} show varying magnitudes and widths over covalent bonds, depending on the tip height, as shown in Fig. 5.2 C. To compare the energy dissipation characteristics of different chemical bonds, the data were analyzed by plotting only the maximum values of the line scans shown in Fig. 5.2 B as a function of tip height. These data were collected over several bonds, as labeled in Fig. 5.3. From the positions optimized using DFT and the electron density distribution, it is observed that the system exhibits both 180° rotational symmetry and inversion symmetry (details are described in section 5.2.1). These symmetries define equivalent bonds being mapped onto each other. Data were collected over several years, with the analysis detailed in this manuscript based on three datasets obtained from two different sample areas.

E_{diss} was measured with a tip height difference of 1 pm. Multiple datasets were acquired over the same bond, and used to calculate averages (thick purple line in Fig. 5.4). Theses data sets include bonds that are symmetrically equivalent, as defined by the theoretical two-molecule unit cell, which will be described in the next section. The shaded purple area in Fig. 5.4 represents the standard deviation between the multiple data sets and the average of them. The vertical distances (horizontal-axis) represent the simulated heights of the metal apex (the terminal Cu atom) relative to the plane of the PTCDA. The tip height of the averaged data was adjusted through calculation (bar plot with a yellow color) so that the maximum value aligns with the same tip height. (The details about the DFT calculation is described in the next chapter.) As previously reported [56], energy dissipation increases exponentially as the tip height (z) decreases, followed by a decrease at even lower heights. This behavior occurs because, below a certain height, the CO molecule can no longer oscillate freely from side to side and instead becomes

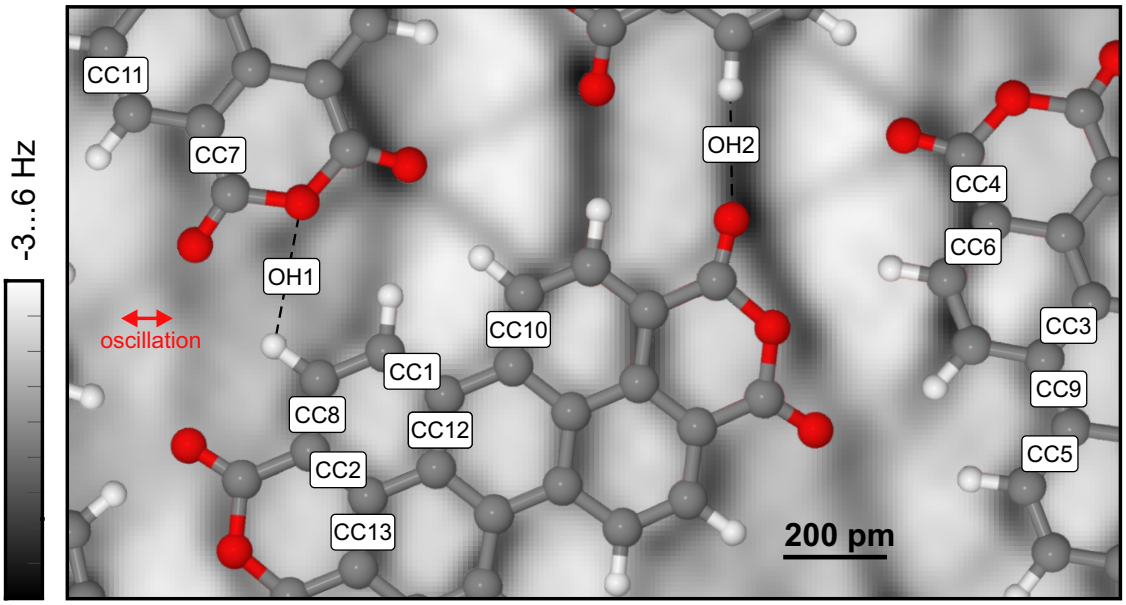

Figure 5.3: Sliding friction measurement over single bonds. The LFM Δf image of PTCDA molecules allows the identification of covalent and hydrogen bonds. (B) Comparison of experimental and simulated energy dissipation over various bonds, as labeled in (A). Energy dissipation measurements were taken with a tip height difference of 1 pm. Multiple datasets were acquired for each bond to calculate averages, shown as the thick purple line. The experimental maximum of $E_{\mathrm{diss}}(z)$ was vertically offset to align with the theoretical model (yellow bar plot) for each bonds. The shaded purple area represents the half standard deviation among the datasets and their average. The horizontal-axis shows the simulated heights of the metal apex (the terminal Cu atom) relative to the PTCDA plane. Numbers indicate the maximum values.

trapped on one side of the bond. Interestingly, the maximum energy dissipation values vary across different types of chemical bonds, as shown in Fig. 5.4. If it were assumed that the interaction of the CO molecule occurs predominantly with the two nearest carbon atoms [56], one would expect that the energy dissipation as a function of height would exhibit uniform characteristics across all covalent bonds. Specifically, this means that the peak width and maximum value of the energy dissipation should be consistent, as long as the covalent bonds are oriented in the same direction relative to the oscillation of the CO molecule (e.g. CC 12 and CC 13 in Fig. 5.3). However, the maximum values of energy dissipation across various chemical bonds are not uniform, and this variations suggest that the interaction of the CO molecule with different covalent bonds is more complex than initially

assumed. Further data was also collected on other bonds, including the O···H bond.

The widths of the peaks resulting from DFT shown in Fig. 5.4 are in excellent agreement with the experimental data, with both measurements indicating peak widths on the order of tens of picometers. This agreement confirms that the distance dependence of inter atomic interactions is accurately represented in the simulation. Additionally, the magnitudes of the maximum values, as explicitly listed in Fig. 5.4 align very well with the experimental results for the various covalent bonds.

It is also important to note that the maximum energy dissipated is not always higher for covalent bonds compared to hydrogen bonds. This adds complexity to understanding energy dissipation. Even though covalent bonds usually involve stronger interactions because of shared electrons, this does not always mean they will show greater energy dissipation than the weaker hydrogen bonds. This finding suggests that energy dissipation is affected by more than just bond type and strength, possibly due to differences in: the orientation of the bonds, the spatial arrangement of the molecules, bond strength, or the specific electronic environment surrounding each bond. A detailed approach including calculation is needed to understand observed dissipated energy, considering both the nature of the bonds and their position in the molecular structure, which is described in the next section.

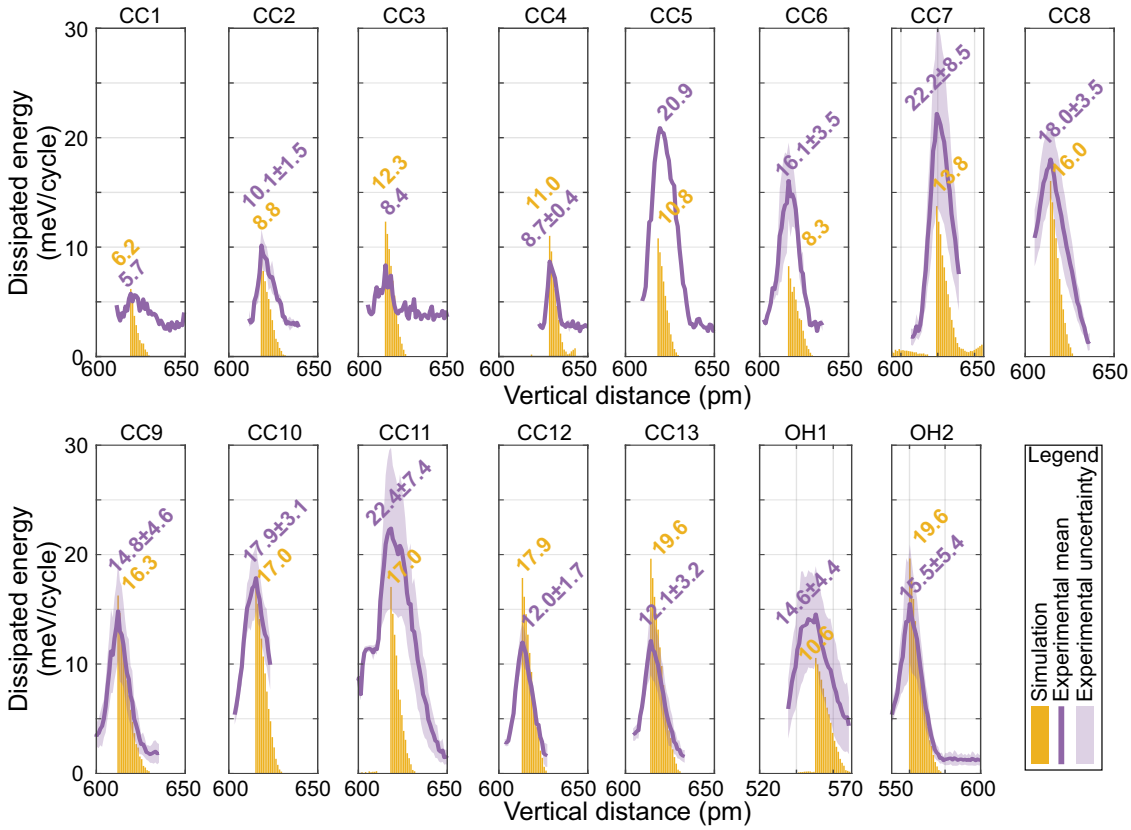

Figure 5.4: Sliding friction measurement over single bonds. Comparison of experimental and simulated energy dissipation over various bonds, as labeled in Fig. 5.3. Energy dissipation measurements were taken with a tip height difference of 1 pm. Multiple datasets were acquired for each bond to calculate averages, shown as the thick purple line. The experimental maximum of $E_{\mathrm{diss}}(z)$ was vertically offset to align with the theoretical model (yellow bar plot) for each bonds. The shaded purple area represents the half standard deviation among the datasets and their average. The horizontal-axis shows the simulated heights of the metal apex (the terminal Cu atom) relative to the PTCDA plane. Numbers indicate the maximum values.

5.2 Modelling sliding friction

To ascertain the properties of a chemical bond that correlates with higher energy dissipation, simulations of the sliding surfaces were conducted with Density Functional Theory (DFT) calculations and the mentioned snapping model. The Potential Energy Surface (PES) experienced by the CO tip is crucial for understanding the different dissipation mechanisms. It is carefully calculated for every bond using DFT combined with Machine Learning methods, which is described in section 5.2.1. Subsequently, the snapping model was applied, as presented in section 5.2.2. This involves analyzing the calculated PES by varying the tip's vertical and lateral positions, the stiffness of the CO tip, and the angle of the bond relative to the tip's oscillation direction. Finally, this chapter will conclude with an analysis of bond order correlation (section 5.2.3) in relation to energy dissipation.

5.2.1 Atomic structure determination

Density Functional Theory modeling was used to determine the atomic positions of PTCDA molecules as an adlayer structure within a supercell on the Cu(111) surface, as shown in Fig.5.5 A. Although the superstructure observed experimentally appears to be incommensurate, a commensurate structure was used in this simulation. This approach aligns with previous discussions in the literature [134], which suggest that using a commensurate structure represents a necessary compromise between achieving accuracy and managing computational resources. In this context, choosing a commensurate supercell is justified because it offers a reasonable approximation of the system while keeping computational demands manageable.

To determine the structure of the adlayer, two PTCDA molecules were positioned within the unit cell according to the geometry suggested by experimental observations. To find the energetically most favorable structure, a geometry optimization was performed starting from this experimental configuration. Both the PTCDA molecules and the first two layers of the copper substrate were allowed to relax, following common practice in such simulations to ensure that the system reaches an optimal and physically realistic arrangement. This was carried out using the FHI-aims quantum chemistry code [135]. The calculation used the PBE exchange-correlation functional [121] and the TSsurf van der Waals correction

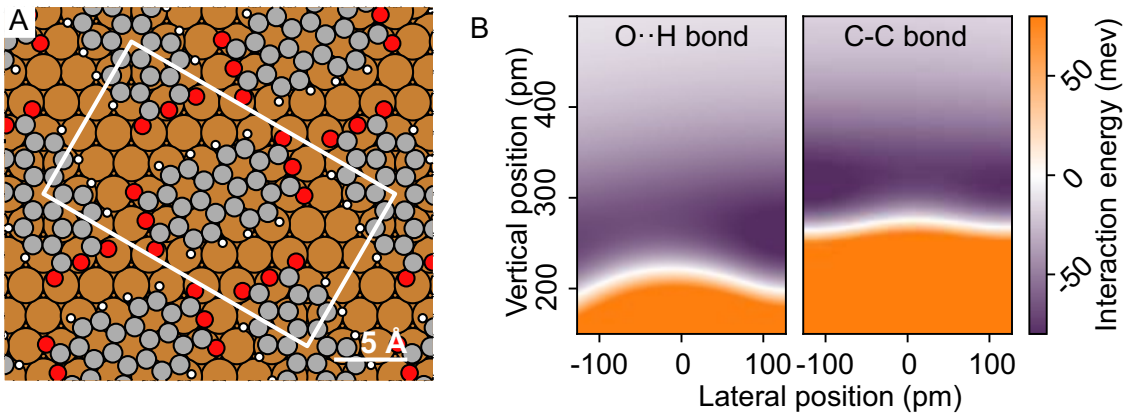

Figure 5.5: DFT calculation process (A) Calculated structure with the supercell. (B) An example of the calculated potential energy landscape over hydrogen and covalent bonds.

scheme [118, 122]. Default tight species settings were applied, and the generalized Monkhorst-Pack k-grid [136] with 44 k-points was used for a reliable sampling of the Brillouin zone.

The substrate was modeled using a repeated slab approach, where the surface was approximated by a slab consisting of five layers of copper atoms. During geometry optimization, all atoms were relaxed until the residual forces on each atom fell below 0.01 eV/Å. The resulting molecular adsorption geometries can be seen in Fig. 5.5 A as a ball and stick representation. For electronic friction calculations, the default light species settings were used due to the high computational demand of these calculations. This choice is typical for such studies to balance computational resources with the necessary accuracy.

The tip interacts with the surface mainly through the CO molecule at the tip apex [49]. To accurately map the potential energy landscape, it is necessary to calculate how the CO interacts at each lateral and vertical position above each chemical bond using a theoretical model that includes quantum mechanical interactions. Because the interaction mainly involves the Oxygen atom [95, 105], the potential energy landscape was calculated with a vertically-oriented CO molecule.

To computationally determine energy dissipation, PES for the interaction between a CO molecule and the sample surface are calculated, as shown in Fig. 5.5 B. Fig. 5.5 B shows slices of the PES, which reveal interactions over hydrogen and covalent bonds. Above the CC bond, the interaction energy has a broader shape,

and high values of energy (repulsive interaction) start to appear at higher heights compared to the O···H bond.

PES were calculated using a machine-learning model based on Gaussian process regression and radial distance functions, a methodology previously applied to describe PES of organic/inorganic interface systems [137]. The training data for these PESs were obtained through DFT calculations, using the same settings as described earlier. For each chemical bond probed, separate PES were generated. Between 250 and 300 data points were used to train the PES for each specific bond. The training data was chosen such that it reached a prediction accuracy (based on a leave-one-out cross-validation error, with a root-mean-square error) of 2 meV for the interaction between the CO molecule and the sample surface. This potential energy landscape was then used as one of the inputs for a snapping model.

5.2.2 Snapping model

The snapping model simulates how the LFM tip oscillates at a specific point. In this simulation, the CO molecule at the tip apex is modeled as a torsional spring that responds to applied forces, while the atoms on the surface are assumed to be fixed [56, 95, 96]. This approach is similar to the well established probe particle model [90], which is widely used to simulate images from normal (oscillation direction relative to the substrate surface) AFM measurements with a functionalized tip.

The snapping model extends the probe particle model by forcing the CO molecule to remain in a local energy minimum, allowing for energy dissipation, as briefly introduced in Fig. 5.1 A. Fig. 5.1 A shows the calculated lateral forces over one oscillation cycle as the tip interacts with a covalent bond. The observed hysteresis loop, representing the difference between the forces during forward and backward motion, supports the hypothesis that energy dissipation results from the mechanical deformation of the tip apex. Specifically, as the CO molecule is cocked and then snaps over a single bond, energy is lost. The area within this hysteresis loop quantifies the amount of energy dissipation occurring during this process [56].

Energy dissipation was analyzed by calculating it as a function of both average lateral and vertical positions, mirroring the way the data were obtained experimentally. This approach accounts for the fact that the chemical bond is not always

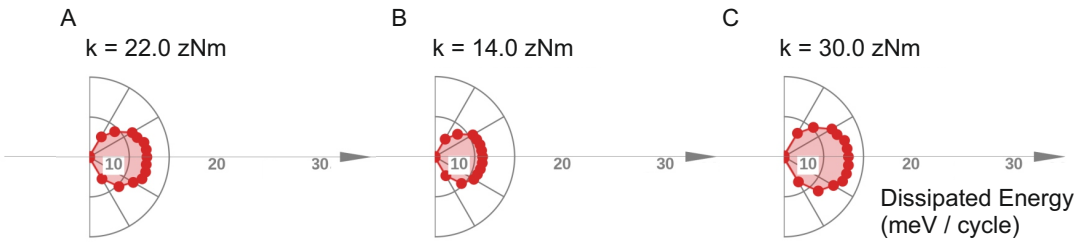

Figure 5.6: Calculated dissipated energy with a various angle and CO stiffness. Dissipated energy (E_{diss}) is calculated by changing the bond angle relative to the tip oscillation direction. The dependence of the stiffness of CO at the tip apex was also evaluated for k values of (A) 22 zNm, (B) 14 zNm, and (C) 30 zNm. The calculation results were obtained for the CC 2 bond.

perfectly perpendicular to the direction of oscillation [50, 138]. Table 5.1 shows the bond angle relative to the oscillation direction applied to the calculation. Fig. 5.6A shows a bond angle (structural) dependent friction calculation over CC 2 bond for an example. The horizontal-axis is the magnitude of the dissipated energy. Vertical-axis presents the angle between the chemical bond and the tip oscillation direction as a range of $-\pi/2$ to $+\pi/2$. Energy dissipation has a largest value when the bond angle is perpendicular to the tip oscillation direction.

Bond Name	Angle (degrees)
CC 1	-60
CC 2	-60
CC 3	45
CC 4	-15
CC 5	45
CC 6	45
CC 7	-15

Bond Name	Angle (degrees)
CC 8	0
CC 9	-15
CC 10	0
CC 11	0
CC 12	0
CC 13	0
OH 1,2	0

Table 5.1: Bond angles. This table lists the bond names and their corresponding angles in degrees. The bonds are presented in two separate columns for easier comparison.

Another crucial parameter in this simulation is the stiffness of the CO tip. Although the stiffness of the CO molecule at the tip apex has been known as k = 22.0 zNm [90, 95], its effect on the simulation is further evaluated by using the different stiffness values as shown in Fig.5.6 B and C. When the stiffness of the CO tip is increased, the amount of energy dissipated during the snapping event also increases. This is

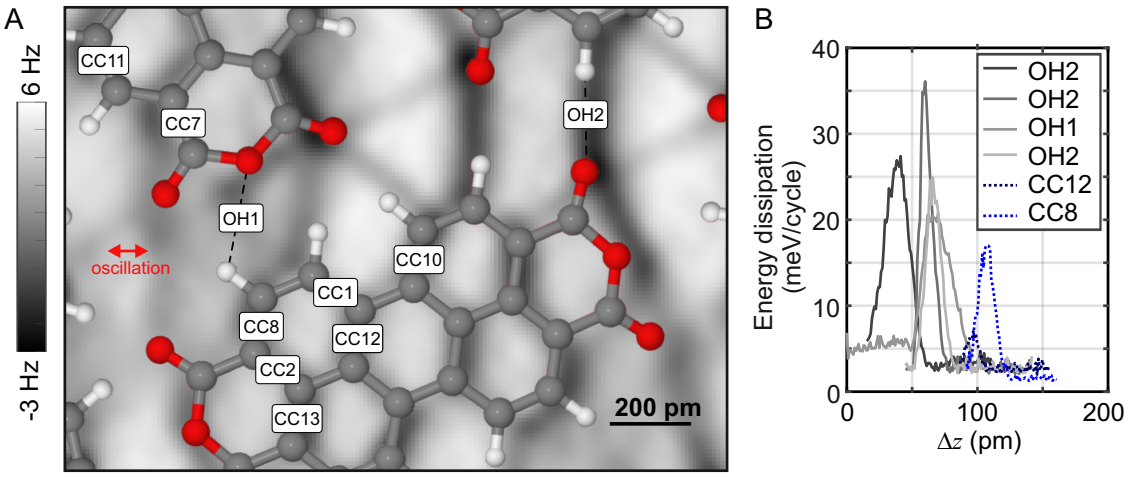

Figure 5.7: Z height difference between OH bond and CC bond. (A) Bond names over the measured area. (B) Energy dissipation over hydrogen (OH) and covalent (CC) bonds showing that the maximum dissipation is observed at higher heights over covalent bonds.

because a stiffer CO tip can store more energy before it snaps, resulting in greater energy dissipation during the snapping process.

To revisit the comparison between experimental measurements and simulations, as shown in Fig. 5.4, it remains to address the question of why the maximum energy dissipated is not always higher for covalent bonds compared to hydrogen bonds. Notably, the simulation results (Fig. 5.4 OH 1 and OH 2) show that energy dissipation over hydrogen bonds occurs at lower tip heights compared to covalent bonds. Although accurately determining the absolute tip height in measurements is challenging, the relative height remains meaningful for comparing the height differences between C-C bonds and O···H bonds. Fig. 5.7 shows the collected data sets over the labeled bonds within a short time frame, allowing for the assumption that vertical drift can be neglected. Additionally, the thermal drift was checked by scanning and comparing the large area before and after acquiring data.

This can be attributed to two main factors: First, the Oxygen atoms in hydrogen bonds are situated lower than the carbon atoms in the PTCDA molecule. Second, the significant interaction in hydrogen bonds is primarily with the atomic cores rather than with the bond itself. Through section 5.1, it is shown that the magnitude of energy dissipation (E_{diss}) varies across different bonds, including different types of bonds. Then section 5.2.1 provides insights into how dissipation differs

between bond types and what factors influence these differences using DFT calculation based on the snapping model. The various magnitudes of E_{diss} are fitting well with a simulation.

However, the key question remains unanswered.: whether there is a noticeable rule or pattern governing the magnitude of energy dissipation and, if so, what that pattern might be. To address this, it is crucial to explore whether the observed dissipation behavior aligns with specific trends or relationships related to the properties of the bonds, such as bond order, bond type, or interaction characteristics.

5.2.3 Bond order

Previous research has established a correlation between the apparent length of a covalent bond and its bond order [116]. This correlation suggests that the potential energy landscape experienced by the CO molecule at the tip apex depends on the bond order. Fig. 5.8 A shows bond orders calculated by DFT.

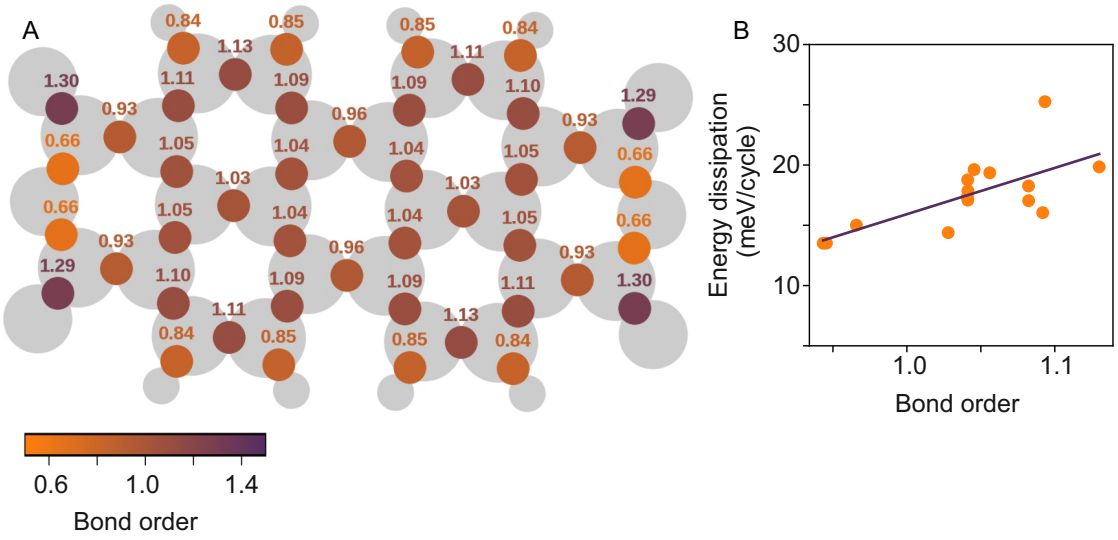

Figure 5.8: Characterizing sliding friction.(A) The bond order calculated for each covalent bond of the PTCDA molecule on Cu(111). (B) Energy dissipation from the simulation as a function of bond order over covalent bonds, with a linear fit.

The bond order was determined using the Mulliken population analysis based on orbital populations calculated with the FHI-aims quantum chemistry code. The FHI-aims code represents the electronic wave function as a linear combination of atom-centered orbitals, described by spherical harmonics and radial functions, with cut-offs applied at large distances [135]. The wave function is expressed as a series expansion in the basis of atom-centered functions:

$$\phi_i = \sum_r c_{ri}\chi_r \tag{5.1}$$

where ϕ_i represents the wave function, χ_r denotes the atom-centered basis functions, and c_{ri} are the expansion coefficients.

To determine the total number of electrons N, the expansion coefficients c_{ri} and the overlap matrix S_{rs} are used:

$$N = \sum_r \sum_s 2c_{ri}^* c_{si} S_{rs} = \sum_r P_{rs} S_{rs} \tag{5.2}$$

where $P_{rs} = \sum_i 2c_{ri}^* c_{si}$. By separating the summation into contributions from all basis functions centered on atoms A and B, the bond order q_{AB} is determined as follows:

$$N = \sum_r \sum_s P_{rs} S_{rs} + \sum_r \sum_s P_{rs} S_{rs} = \sum_r q_A + \sum_r q_{AB} \tag{5.3}$$

Here, the second term q_{AB} represents the bond order between atoms A and B, reflecting the bond strength and nature. This method provides a measure of bond order for any pair of atoms, including hydrogen bonds, even though bond order is not typically applied to them.

Fig. 5.8 B shows the energy dissipation as a function of bond order for covalent bonds within the PTCDA molecule. The analysis considered fifteen covalent bonds. To assess the relationship between bond order and energy dissipation, the Pearson correlation coefficient r is first determined. In this case, the correlation coefficient is found to be $r = 0.68$. This value indicates a moderate to strong positive linear relationship between bond order and energy dissipation. To evaluate whether this correlation coefficient is statistically significant, a Student's t-test is employed. The t-score is calculated using the formula:

$$t_{score} = r \cdot \sqrt{\frac{n-2}{1-r^2}} \tag{5.4}$$

where n represents the sample size, and r is the Pearson correlation coefficient. The next step is to determine the confidence level associated with the t-score. This is done by evaluating the cumulative distribution function of the Student's t-distribution using the computed t-score. A one-tailed test is used because the focus is on validating the significance of a positive correlation coefficient. In this analysis, a significance level of 99.8 % is obtained. This high level of significance indicates that there is a very low probability (0.2 %) that the observed correlation is due to random chance.

5.3 Discussion

This chapter aimed to quantitatively characterize the relationship between the magnitude of energy dissipation over single chemical bonds and the nature of those bonds using molecular snapping. The snapping technique, previously introduced to study friction at the single-atom level between sliding surfaces [56], was qualitatively established using a simple empirical model.

Building on this work, simulations based on DFT were employed. While Lennard-Jones interactions provide a basic description of atomic interactions, DFT offers greater precision by treating atoms as electron clouds, allowing for a more detailed calculation of interactions. Machine learning methods were used to optimize computational efficiency in these simulations.

Using a well-characterized tip functionalized with a CO molecule, energy dissipation over individual chemical bonds, including both covalent and hydrogen bonds, was mapped. The DFT simulations closely matched the experimental results, validating the mechanism of molecular snapping.

Interestingly, the nature of a chemical bond cannot be fully determined by the magnitude of dissipated energy alone. It was observed that hydrogen bonds dissipate energy at lower tip heights compared to covalent bonds, likely due to interactions with atomic cores rather than the bonds themselves.

Section 5.1 covers energy dissipation measurements over various chemical bonds. Multiple 3D data sets were acquired in a highly stable environment to ensure reproducibility. Aditionally, the data were collected with different CO tips and re-prepared surfaces. Defining equivalent chemical bonds on the incommensurate surface was challenging, but symmetry was identified by comparing E_{diss} data sets acquired with different CO tips and molecular islands. The system has a 180ř rotation symmetry and an inversion symmetry, and confirmed again via DFT-relaxed positions and electron density.

Section 5.2 details the calculation steps. DFT calculations were performed, and a machine learning model was trained to refine these predictions. Separate PESs were calculated for each bond, and the snapping model was applied to determine energy dissipation. The results also accounted for the angle relative to the sensors oscillation direction. DFT simulations agreed well with the experimental data and confirmed that hydrogen bonds dissipated energy at lower heights than covalent

bonds, likely due to interactions with atomic cores. Finally, analyzing covalent bonds within the PTCDA molecule showed a clear correlation between bond order and energy dissipation. Higher bond orders resulted in greater energy dissipation, with an approximately linear trend.

In conclusion, the investigation of friction over single chemical bonds within the PTCDA molecule demonstrates that sliding friction over covalent bonds increases with bond order.

6 Phononic contribution to friction

Friction, as described by Newton's laws of motion, arises when two surfaces slide against each other, leading to the conversion of kinetic energy into other forms of energy. A common example of this is rubbing our hands together, where the kinetic energy from the motion is transformed into heat, raising the temperature of our skin. This heat generation results from the microscopic interactions at the interface of the sliding surfaces.

At the nanoscale, frictional energy dissipation becomes even more complex due to various mechanisms, including phononic, electronic, electromagnetic, and quantum effects. These mechanisms depend on factors like the material properties, sliding velocity, and temperature. However, current theoretical models often consider these mechanisms in isolation, leading to a fragmented understanding of friction. For instance, the widely used Prandtl-Tomlinson model [43, 44] effectively describes atomic-scale friction but may obscure the underlying processes that contribute to energy dissipation.

Experimental evidence shows that different mechanisms, such as phononic or electronic friction, can dominate under specific conditions. Despite this, a unified theoretical framework that consistently accounts for these diverse mechanisms remains elusive, and direct experimental validation is still needed. It is also crucial to differentiate between the loss of momentum and the conversion of energy into heat, as these processes can occur at different scales and involve various internal degrees of freedom within the materials.

The debate over the mechanisms contributing to friction, particularly the role of phonons, has been a significant point of contention. For example, experiments by Cannara *et al.* on Hydrogen and Deuterium covered surfaces suggested that phononic contributions are significant, with Hydrogen-covered surfaces exhibiting higher friction due to higher vibrational energy [139]. In contrast, Mo *et al.*, through molecular dynamics simulations, found no clear trend between the mass of the

terminating layer and frictional force, suggesting that other factors might explain the differences in friction rather than phononic effects alone [140]. Their debates began a decade ago and have been revisited until now [141–144].

These experiments were conducted using friction force microscopy (FFM), a technique that, while capable of producing atomic-scale contrast, typically involves multiple atomic contacts. Around the same time, atomic resolution experiments using STM and nc-AFM were conducted on Hydrogen-terminated surfaces, advancing our understanding of surface interactions at the atomic level [145, 146].

Building on these concepts, we employed LFM to directly measure friction with single-atom resolution. Unlike previous studies focusing on Hydrogen adsorption and desorption, our approach combines the high-resolution capabilities of AFM with a focus on phononic contributions to friction. By comparing friction measurements using Hydrogen-terminated tips with those using Deuterium-terminated tips, the study aims to isolate and understand the role of phonons in friction at the atomic scale.

To examine phononic effects exclusively, isotopes of different masses are used in this chapter. In section 6.1, isotopes of CO molecules at a tip apex as is described as an extension of the previous chapter 5. Section 6.2 covers a simple theory about phononic friction and discuss the isotopes used in this chapter. Section 6.3 presents the energy dissipation measurement over the surfaces of Hydrogen- and Deuterium-terminated Si(100) with a single atom resolution. This final chapter takes another step toward resolving the debate [139–141].

6.1 Vibrational properties of a CO tip

The oscillation frequencies of a molecule on a surface are defined by the distribution of mass within the molecule and the restoring forces generated when the molecule bends [147, 148]. These restoring forces arise from atomic-scale interactions both within the molecule and with the surface, and are crucial to the molecule's dynamics and reactivity [141].

One way of changing the distribution of mass within the molecule without changing its chemical properties is the use of isotopes [139]. To this end, identical bonds were probed using tips terminated with different CO isotopes, as an extension of

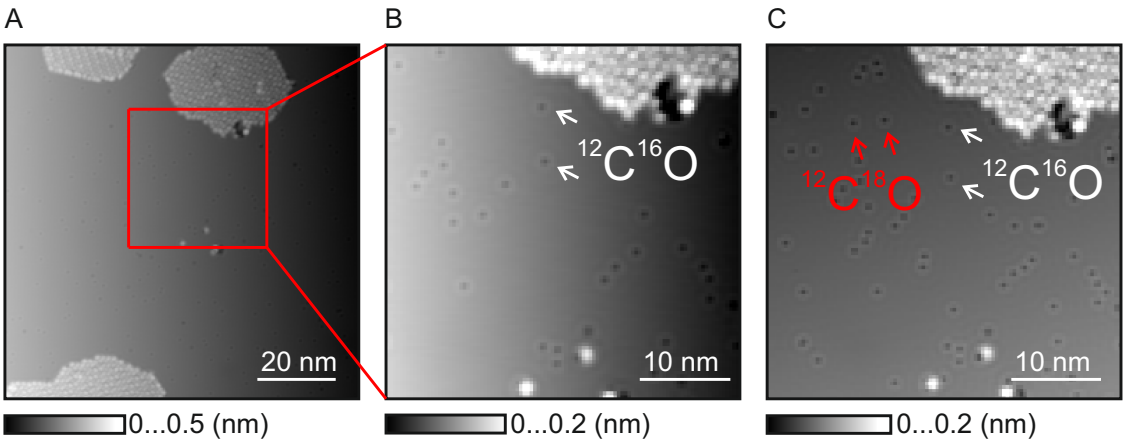

Figure 6.1: CO isotopes on Cu(111). (A) Large size STM image of the Cu(111) surface with $^{12}C^{16}O$ and PTCDA islands. (B) Zoomed in area of the surface in (A), indicated with a red rectangle in (A). (C) Same area scanned after dosing $^{12}C^{18}O$ additionally. By comparing with (B), $^{12}C^{16}O$ and $^{12}C^{18}O$ can be recognized. Scan parameters were set identically for each image, $V_B = 400\,mV$, $I_{set} = 50\,pA$.

the previous chapter. The isotopes used in this study are $^{12}C^{16}O$, which was also used for the experiments presented in the previous chapters, and $^{12}C^{18}O$. Fig. 6.1 A and B show Cu(111) after the adsorption of $^{12}C^{16}O$. The area indicated with a red rectangle in Fig. 6.1 A is the same area shown in Fig. 6.1 B and C. After scanning Fig. 6.1 B, the tip was retracted and $^{12}C^{18}O$ was carefully dosed. The tip was only slightly retracted (around 10 steps with a z-piezo walker) to stay at the same location over the sample, and $^{12}C^{18}O$ was dosed in for a short time of 1 minute to prevent the tip from crushing into the sample due to an increase in temperature. By comparing the images before and after the dosing, $^{12}C^{16}O$ and $^{12}C^{18}O$ were recognized as shown in Fig. 6.1 C. Additionally, techniques such as inelastic scattering (e.g. with helium atoms or electrons) can be used to distinguish the isotopes since the vibration frequencies of the molecules are different due to their different masses. The energy lost by the scattering particles corresponds to the vibrational excitations of the molecules (see section 2.1) [149, 150].

Isotope-specific vibration spectra of individual molecules have been mesured with Inelastic Electron Tunneling Spectroscopy (IETS) [67]. The excited vibrational states can be observed as peaks in the second derivative of the current-voltage curve [67, 151]. These peaks correspond to the vibrational excitations of the adsorbed molecule in the experiment described in this section. Furthermore,

a uniform and well-characterized single atom tip was used, checked by the COFI technique [152] before the IETS measurements, as described in section 3.3 and 2.1 for each. This is important because optimizing both the apex structure and material of the tip enhances the resolution of the IETS signal [152]. To measure the differential conductance ($\frac{\mathrm{dI}}{\mathrm{dV}}$) and IET signals ($\frac{\mathrm{d}^2 I}{\mathrm{d}V^2}$), a modulation voltage (496 Hz with a 3 mV rms amplitude) is applied to the sample, and detected harmonics are processed via a lock-in amplifier integrated within the Nanonis system.

Fig. 6.2 A and B show normalized IETS measured over CO molecules including isotopes. The normalized IETS are calculated as the second derivative of the current-voltage curve divided by the conductance. This normalization helps to isolate the vibrational features from the overall conductance and provides a clearer picture of the vibrational states [151, 152]. Additionally the IETS on a flat Cu(111) surface has been subtracted from that measured on top of the CO molecules. Fig. 6.2 B shows spectra acquired with higher resolution, in a narrower voltage range. This regime corresponds to the frustrated translational (FT) modes ($E_{\mathrm{FT}} = 4.2\,\mathrm{meV}$), one of two lateral vibrational modes, as shown in Fig. 6.2 C [153]. The corresponding energy of frustrated rotational (FR) modes of CO is $E_{\mathrm{FR}} = 35.4\,\mathrm{meV}$ [152–155]. The spectra were recorded at a height corresponding to a setpoint of $V_{\mathrm{B}} = 50$ mV and $I_{\mathrm{set}} = 5\,\mathrm{nA}$. The energy states of the FT mode were identified by looking at the peak with the highest IETS value around 4.2 meV and finding its corresponding V_{B}. This yields $^{12}\mathrm{C}^{16}\mathrm{O}$ has an E_{FT} value of 4.7 meV, while $^{12}\mathrm{C}^{18}\mathrm{O}$ has 4.3 meV and 4.2 meV, as shown in Fig. 6.2 B.

Although two vibrational modes are nicely measured, it requires further data processing (e.g.normalization and subtraction) to recognize the small difference between the peaks. For this study, the bias line is connected to the Nanonis controller at room temperature ($\approx 300\,\mathrm{K}$), which results in thermal noise of $\frac{300K \times k_{\mathrm{B}}}{h} \approx 6\,\mathrm{THz}$ where k_{B} is the Boltzmann constant and h is the Plank constant. The RF noise causes the V_{B} to smear out, leading to a broadening of the spectroscopic features along the V_{B} (energy) axis. This decrease the precision in determining the peak positions [153, 156]. To minimize this effect, it is recommended to use appropriate low-pass filters, properly grounded and shielded pre-amplifier and shielded cables. Therefore, the isotopes were identified using both IETS and scanning [156]. Their locations were reconfirmed by comparing the images obtained before and after isotope dosing.

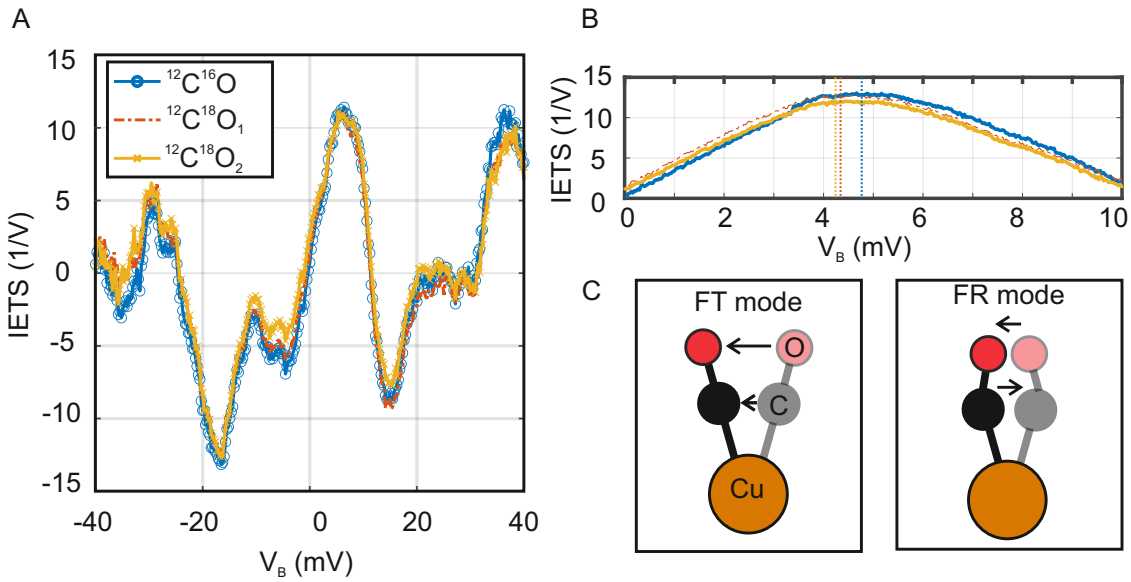

Figure 6.2: Measurements of the vibrational energy of CO isotopes. (A) Normalized IETS measured over three different CO molecules, including isotopes. The spectra were obtained from the molecules indicated in Fig. 6.1 C. (B) Normalized IETS of the FT mode. Measured over the same molecules used in (A), but within a narrower voltage range. The energy states of the FT mode were identified by examining the peak with the highest IETS value, around 4.2 meV, and determining its corresponding voltage, V_B. This yields that $^{12}C^{16}O$ has an E_{FT} value of 4.7 meV, while $^{12}C^{18}O_1$ has 4.3 meV and $^{12}C^{18}O_2$ has 4.2 meV (C) Schematic images of FT mode (left) where the C and O atoms deflect in the same direction and FR mode (right) where they deflect in opposite directions. The setpoint durng measurement was $V_B = 50$ mV and $I_{set} = 5$ nA. The lock-in modulation voltage was 3 mV.

PTCDA molecular islands on Cu(111) were selected as the test system to probe with isotope CO-functionalized tips, extending the study from the previous chapter. Fig. 6.3 illustrates the measurement region and the corresponding dissipated energy. Bond 1, which is relatively perpendicular to the tip oscillation direction (indicated by the red arrow in Fig. 6.3 A), was selected due to its rigidity, allowing for an accurate measurement. Bond 2 is located near the O atom, where it forms a bond with an underlying Cu atom and exhibits a buckling effect. These two bonds were examined due to this additional interesting characteristic.

The tip was functionalized after distinguishing the CO isotopes via IETS and comparing the scanned images of the same area before and after isotope dosing. The CO pick-up conditions were identical for both isotopes as shown in section 3.3. After pick-up, the tip was moved to the same location, and the same bond of the same

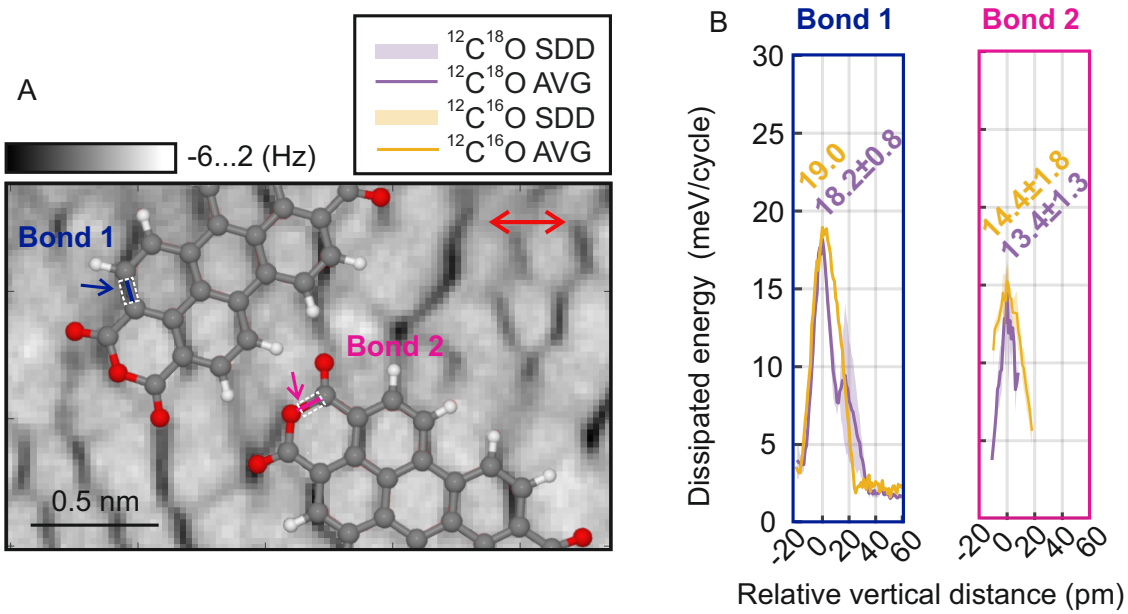

Figure 6.3: Dissipated energy measured with CO isotope tips. (A) The locations of the bonds where dissipated energy was measured. Energy dissipation was recorded with a tip height spacing of 1 pm. Multiple datasets were collected from the same bond to calculate the averages. (B) The thick purple line represents the averaged data (AVG) acquired with a $^{12}C^{18}O$ tip, while the thick yellow line shows the averaged data with a $^{12}C^{16}O$ tip. Measurements over Bond 1 are shown on the left, and Bond 2 on the right, as indicated in Fig. 6.3 A. The shaded area represents half of the standard deviation (SDD) of the multiple datasets and their average. The numbers indicate the maximum value of the averaged dissipated energy and half of the standard deviation.

molecule was measured to ensure a direct and accurate comparison. The locations of the measured bonds are indicated in Fig. 6.3 A, and the measured dissipation energy is shown in Fig. 6.3 B.

The dissipated energy was measured with a tip height spacing of 1 pm. Multiple datasets were acquired over the same bond, and used to calculate averages. The thick purple line in Fig. 6.3 B represents averaged data (AVG) acquired with $^{12}C^{18}O$ tip and the thick yellow line shows averaged data acquired with $^{12}C^{16}O$ tip. The left side figure of Fig. 6.3 B is measurement over Bond 1 and the right side is measurement over Bond 2, indicated in Fig. 6.3 A. The shaded area represents the half standard deviation (SDD) of the multiple data sets and the average of them. The written numbers are the maximum value of the averaged dissipated energy and half standard deviation.

The vertical distances (horizontal axis) represent the relative tip heights, with 0 defined as the height at which the maximum value of dissipated energy was acquired. The measurements with the $^{12}C^{16}O$ tip has a wider peak width, and larger maximum value. However, the difference is within the standard deviation, so it is hard to clearly distinguish them. To understand how phonons contribute to energy dissipation, the next section will discuss simplified phononic friction theory, following Persson's idea [2].

6.2 Simple Theoretical Derivation

Our current understanding of atomic-scale friction remains semi-phenomenological. While mechanisms involving phonons [157–161] or electronic [162–164] interactions are frequently cited, several crucial questions about friction are still unresolved. Firstly, what is the timescale over which energy and momentum losses become irretrievable? Specifically, how does kinetic energy convert into heat distribution, and what is the duration of this conversion process? Another important question is how and on what timescale mechanical energy transitions into heat, particularly through phonon interactions. How swiftly does this conversion occur once the mechanical energy is transformed into heat?

In this section, these mechanisms will be addressed using a simplified model, aiming to bridge the gap between theoretical predictions and experimental findings. The model incorporates elastic collisions and estimates the propagation of energy from the excited atom based on the speed of sound within the material. The model is based on the framework developed by Persson [2], which simplifies the adsorbate oscillation as a collision with the substrate. Persson developed a model to explain the phononic contribution to friction, specifically focusing on the interaction between an adsorbate monolayer and a single moving surface [2]. In this model, friction arises from inelastic collisions between vibrating adsorbates and the surface. While this setup does not perfectly align with the conditions observed in AFM measurements, where confined atoms are chemisorbed to one surface and interact with the other under load, the authors in Ref. [139] suggest that the model still offers valuable qualitative insights.

The applicability of this model to real-world systems, such as AFM experi-

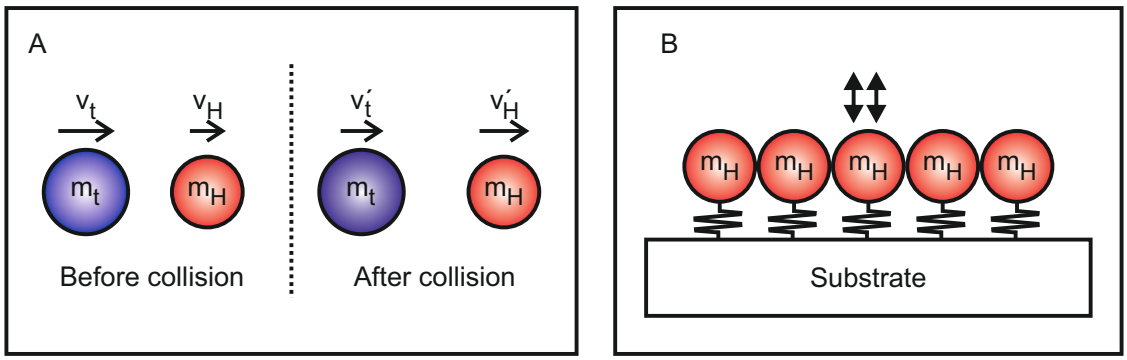

Figure 6.4: Model description with collision. (A) The elastic collision process between the tip and a surface Hydrogen atom. m_t denotes the effective mass of the tip portion involved in the collision, moving with velocity v_t. The massm_t collides with a stationary Hydrogen atom, with mass m_H, adsorbed on the surface. As a result of the collision, the Hydrogen atom gains energy. The total momentum is conserved before and after the collision. (B) A schematic of the frictional interface. Vibrating adsorbates collide with and dissipate kinetic energy from the moving tip at a rate that depends on the adsorbates frequency and thus its mass.

ments, also raises important questions regarding the timescale of inelastic collisions. Whether it can be measured, and what exactly is being measured during such experiments, are crucial considerations. These inquiries continue to drive research into friction mechanisms. After the model description, the concept of the speed of sound within the material is employed to provide a brief understanding of the timescale associated with phononic contribution to friction.

When a body slides over a surface, the kinetic energy of the moving body (tip) is partially converted into the vibrational energy of the surface atoms, which can be represented as phonons. This increase in vibrational energy contributes to heat generation, and as friction generates heat, it raises the local surface temperature. The first mechanism is illustrated using an elastic collision, as shown in Fig. 6.4 A.

Fig. 6.4 A illustrates the simple one-dimensional elastic collision process. m_t represents the mass of the portion of the tip effectively involved in the collision. The tip, moving with a velocity v_t, collides with a Hydrogen atom adsorbed on the surface, which has a mass m_H and an initial velocity as zero. As a result, the collided Hydrogen atom gains energy. The total momentum is conserved before and after the collision:

$$m_\mathrm{t} v_\mathrm{t} = m_\mathrm{t} v'_\mathrm{t} + m_\mathrm{H} v'_\mathrm{H} \tag{6.1}$$

where v'_{t} and v'_{H} are the velocities of tip and adsorbed H atom after the collision. The total kinetic energy is conserved before and after the collision:

$$\frac{1}{2}m_{\mathrm{t}}v_{\mathrm{t}}^2 = \frac{1}{2}m_{\mathrm{t}}v_{\mathrm{t}}'^2 + \frac{1}{2}m_{\mathrm{H}}v_{\mathrm{H}}'^2 \tag{6.2}$$

By substituting v'_{t} from Eq. 6.1 into Eq. 6.2, the velocity of Hydrogen after the collision, v'_{H}, can be derived as $v'_{\mathrm{H}} = \frac{2m_{\mathrm{t}}v_{\mathrm{t}}}{m_{\mathrm{t}}+m_{\mathrm{H}}}$. Then, the kinetic energy of Hydrogen after the collision, $\frac{1}{2}m_{\mathrm{H}}v_{\mathrm{H}}'^2$, is $\frac{2m_{\mathrm{H}}m_{\mathrm{t}}^2v_{\mathrm{t}}^2}{(m_{\mathrm{t}}+m_{\mathrm{H}})^2}$. The same process is applied to the D atom. To compare both systems, the ratio of the kinetic energy of the atoms after the collision can be obtained as follows:

$$\frac{E_{\mathrm{D}}}{E_{\mathrm{H}}} = \frac{(m_{\mathrm{t}}+m_{\mathrm{H}})^2}{(m_{\mathrm{t}}+m_{\mathrm{D}})^2}\frac{m_{\mathrm{D}}}{m_{\mathrm{H}}} \tag{6.3}$$

The mass of the portion of the tip effectively involved (m_{t}) and the initial velocity of that portion (v_{t}) are assumed to be the same for both cases.

Assuming $m_{\mathrm{t}} >> m_{\mathrm{H,D}}$ where the effectively involved tip mass is much larger than the mass of the adsorbed atom, this can be interestingly rewritten as

$$\frac{E_{\mathrm{D}}}{E_{\mathrm{H}}} \approx \frac{m_{\mathrm{D}}}{m_{\mathrm{H}}}. \tag{6.4}$$

This simple model predicts that an D-terminated substrate will dissipate twice the energy per collision compared to a H-terminated substrate. However, this shows opposite results to Persson's model, which is described in Ref. [2] and has been used to explain the experimental results [139, 165]. While Persson and Cannara *et al.* explained similar systems using a rate of energy dissipation per unit time [2, 139], the elastic collision model in this section focuses on the kinetic energy resulting from the different masses of the adsorbates in a single collision. A description of Persson's model can be found in appendix .2

When applying the same theory to the case of CO isotopes (see section 6.1), equation 6.4 gives:

$$\frac{dE_{^{12}C^{18}O}}{dE_{^{12}C^{16}O}} = \frac{m_{^{12}C^{18}O}}{m_{^{12}C^{16}O}} \approx \frac{30u}{28u} \approx\ 1.07 \tag{6.5}$$

Using the measured maximum values of dissipated energy from Fig. 6.3, the ratio of dissipated energy can be calculated, yielding for the measurement over Bond 1,

$\frac{dE_{^{12}C^{16}O}}{dE_{^{12}C^{18}O}} = \frac{19.0}{18.2} = 1.04$, and for the measurement over Bond 2, $\frac{dE_{^{12}C^{16}O}}{dE_{^{12}C^{18}O}} = \frac{14.4}{13.4} = 1.07$. These values agree better with the Person's model output in appendix .2. However, the experiment requires a very high signal-to-noise ratio since the mass ratio is very small between $^{12}C^{16}O$ and $^{12}C^{18}O$. While the average value from multiple measurements shows good agreement, the standard deviations of these data sets overlap, as shown in Fig. 6.3.

Using a surface terminated with H/D would result in a larger difference in energy dissipation, as calculated above. The mass of the H atom is nearly half that of the D atom, and their relative masses compared to the surface atom are also significantly larger. In section 6.3, H/D terminated Si(100) is used. While the Si(100) surface is very reactive because of unsaturated bonds, it allows for a controlled and reproducible termination of the surface with H or D atoms. Additionally, the surface can be terminated with a single layer of atoms, making it easier to study the effects of different terminants.

Then, the second question was how quickly the generated phonon modes dissipate after a collision. The speed of sound within the material provides a framework for understanding this process (see Fig. 6.4 B).

Previous studies have investigated the lifetimes of vibrational levels of hydrogen adsorbed on the Si(100) surface. These studies reveal that the lifetimes of the lowest vibrational levels differ significantly depending on the mode: stretching modes have lifetimes on the order of nanoseconds, while bending modes lie in the picosecond range, as shown by computational models in Ref. [83]. For example, the lowest stretching mode has a lifetime of 2130 ps, and the lowest bending mode has a lifetime of 1.35 ps at zero temperature in their calculation. Their calculation of the the lifetimes of stretching modes is consistent with available experimental observations [83], range from 6 ns to 1.2 ns, depending on temperature.

However, AFM operates in the much slower kHz measurement regime. Therefore, what we are measuring is not the effect of a single collision, but rather the average outcome of multiple collisions.

This time scale can again be checked by comparing it with the peak width of CO's FR mode. In Fig. 6.2, the peak width is around 5 meV. Note that the IETS peak contains more than a single phonon mode and depends on the tip shape. Also, the use of a AC voltage amplitude of 3 mV introduces an artificial broadening in the measurement, which means the observed linewidth is wider than the actual

(natural) linewidth. According to the Heisenberg Uncertainty Principle, $\Delta E \cdot \Delta t \geq \frac{\hbar}{2}$, where ΔE is the uncertainty in energy, Δt is the uncertainty in time, $\hbar$ is the reduced Planck's constant ($\hbar = \frac{h}{2\pi} \approx 1.055 \times 10^{-34}\,\mathrm{J \cdot s}$). By substituting the values, $\Delta t \geq \frac{1.055\times10^{-34}\,\mathrm{J{\cdot}s}}{2\times(5\times10^{-3}\,\mathrm{eV}\times1.602\times10^{-19}\,\mathrm{J/eV})} = 6.59 \times 10^{-14}\,\mathrm{s}$, and $\Delta f = \frac{1}{\Delta t} \approx 15.2\,\mathrm{THz}$. Since the measured linewidth includes contributions from the applied AC voltage, the calculated lifetime, which is based on this linewidth, underestimates the true lifetime of the system. Therefore, it provides only a brief understanding of the vibration mode's time scale.

6.3 Friction measurement over H/D -Si(100)

The Si(100) surface, in its clean and unsaturated state, exhibits rows of silicon dimers [166, 167]. These dimers, consisting of pairs of silicon atoms, bond together and align in parallel rows across the surface. On an atomic terrace, these dimers line up in one direction, while on a lower terrace, which is one step down, the dimer rows are orthogonal to those on the upper terrace. This creates a regular, patterned arrangement visible in STM images as shown in Fig. 6.5 A. The unsaturated dimers are highly reactive, often buckling or bending due to their high reactivity and the strain in surface bonds [166, 168–171]. Fig. 6.5 B and C are LFM Δf images of the unsaturated surface measured over the same region, different tip height. Fig. 6.5 C is a measurement 20 pm closer to the surface, and shows that the tip changed during scanning (indicated with a red arrow). The height variations, related to dimer buckling and step edges between terraces, make it challenging to scan bare Si(100) surfaces without changing the tip.

When the Si(100) surface is terminated with Hydrogen or Deuterium (H/D-Si(100)), the Si dimers become saturated with H or D atoms [172]. Fig. 6.6 A shows a STM image after deuterium termination. H or D termination causes the surface to rearrange into a 2×1 symmetric pattern, as shown in Fig. 6.6 B. The preparation process is described in Sec. 3.2. Different patterns such as 3×1 or 2×2 can be achieved by varying the temperature of the Si(100) surface during the termination process [172, 173].

The STM image of a H/D-Si(100) typically shows a periodic array of bright spots corresponding to H/D atoms bonded to the Si atoms [166]. The STM resolution can

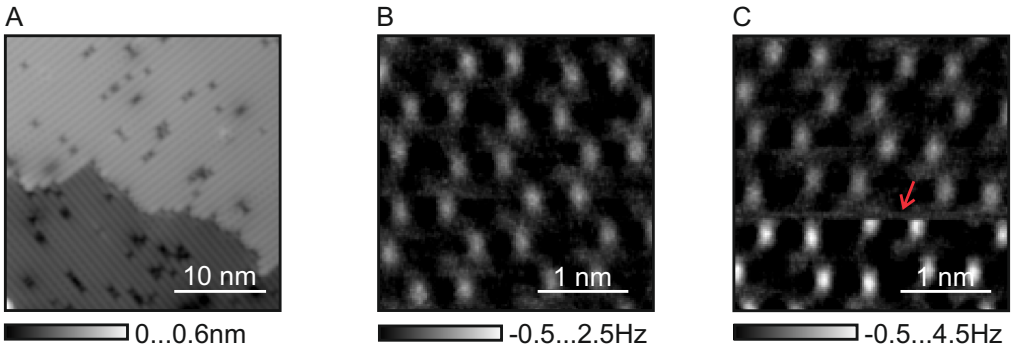

Figure 6.5: Bare Si (100). (A) STM image of a Si(100) surface showing dimer rows. The dimer rows on the lower terrace are orthogonal to those on the upper terrace. V_B = -800 mV, I_{set} = 30 pA. (B) LFM image scanned with an oscillation amplitude of 50 pm. White dots correspond to the location of Si atoms. (C) Same area as (B), tip height is 20 pm lower. Tip changed at the area indicated with the red arrow. For LFM measurements, V_B was set to zero.

be high enough to resolve individual H atoms and the underlying Si atoms [174].

H/D termination makes the surface much less reactive, thus more stable. LFM images usually reveal a more even surface with less chemical reactivity, resulting in less tip changes, as shown in Fig. 6.6 B and C.

When the sample is aligned such that the tip oscillation is parallel to the Si dimer rows on a given terrace, moving to a higher or lower terrace allows for data collection with the tip oscillating perpendicular to the dimer rows, as shown in, Fig. 6.6 A. This setup allows the investigation of frictional stiffness both parallel and perpendicular to the dimer rows [50]. This section will focus more on exploring phononic friction by comparing H-Si(100) and D-Si(100), rather than examining the directional dependence of friction.

By slicing the Si wafer along the [011] plane, the [011] direction can be aligned with the tip oscillation inside the vacuum chamber. The sample was cut by hand and placed on a sample holder before being put in the vacuum chamber. The angle between the dimer rows and the tip oscillation direction is approximately 8ř (or 98ř) degree, measured from the obtained LFM image, Fig. 6.6 C. The tip oscillation direction is indicated with a red arrow.

To ensure a known tip apex configuration, a single D atom was picked up before acquiring the 3D data set. Accurate tip positioning is crucial, as incorrect positioning can lead to improper Hydrogen removal [174]. Both STM and LFM images

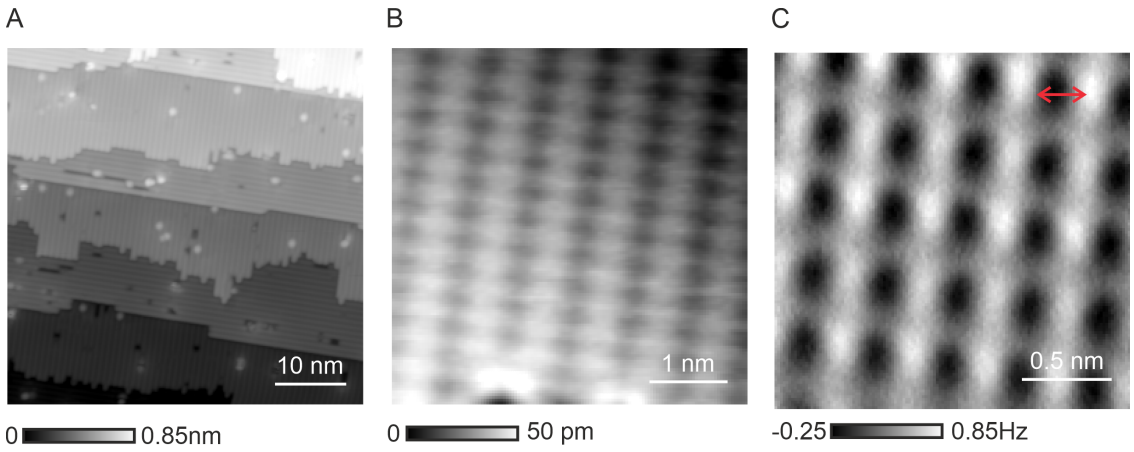

Figure 6.6: D terminated Si (100). (A) STM image of the D-Si(100) surface showing dimer rows. The dimer rows on the lower terrace are orthogonal to those on the upper terrace. V_B = -800 mV, I_{set} = 30 pA. (B) STM image over a single terrace. Dimer row has a perpendicular direction relative to the oscillation direction for this image. (C) LFM constant height Δf image scanned with oscillation amplitude of 50 pm. $V_B = 0$ to prevent the tip crushing into the surface. The scanned area is the same as in (B), but smaller image size. White dots correspond to the location of D terminated Si atoms. The detailed location will be discussed in the next figure. Tip oscillation direction is indicated with a red arrow.

were used to precisely locate the tip above a Hydrogen atom. After checking the location of the atoms with LFM imaging and positioning the tip, the STM feedback was turned on with parameters of 1.3 V and 50 pA for the H/D pick-up process. Fig. 6.7 A and B show the STM and LFM images before the D pick-up. To pick up a single H or D atom, a short voltage pulse was applied while the STM feedback was on. As illustrated in Fig. 6.7 C, this results in the selective desorption of the H or D atom under the tip apex, which is often transferred to the tip. Fig. 6.7 shows a typical STM image of the created single dangling bond. In accordance with earlier studies, the removed H/D creates a dangling bond that appears as a bright protrusion as a change in the local tunneling current [145, 146]. If the tip successfully picks up a H/D atom and becomes bonded to the tip apex, the imaging resolution also changes. This is similar to what is well known for the CO molecule, where once it is picked up by the tip apex following a voltage pulse it enhances the STM and AFM contrast [52].

Interestingly, the magnitude and duration of the bias pulse differ between the H and D pick-up conditions. The H atom was picked up using a voltage pulse of 1.8 V

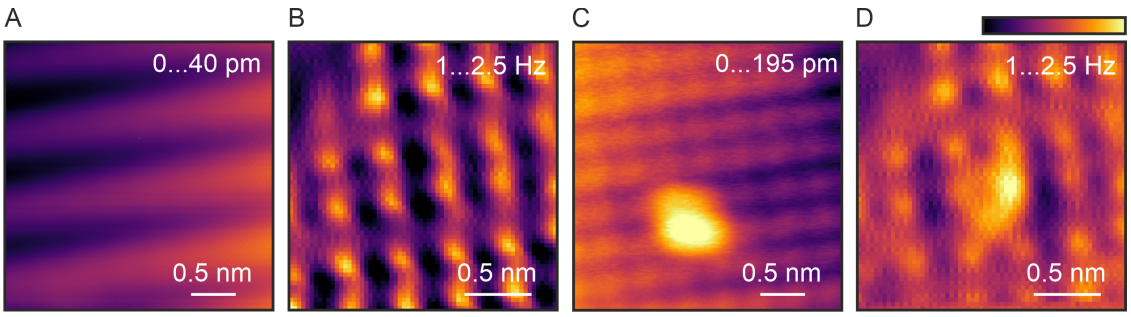

Figure 6.7: Single H/D pick up (A) STM image of D-Si(100) rows before D pick-up. $V_B = -1.8\,V$, $I_{set} = 50\,pA$. (B) LFM image of D-Si(100)rows before D pick-up. Oscillation amplitude is 50 pm. (C) STM image of same area after pick-up. dangling bond is brighter than surrounding region. Scanning parameter is $V_B = 1.3\,V$, $I_{set} = 50\,pA$. (D) LFM image after D pick-up. Oscillation amplitude is 50 pm. The oscillation direction is parallel to the figures. The bias is applied to the sample side for all measurements.

for 20 ms, while the D atom was picked up with a higher voltage of 2.2 V for 40 ms.

The LFM image after pick-up can be used to check the single atom tip apex, similar to the COFI mechanism (see section 3.3), as shown in Fig. 6.7 D. The dangling bond is represented as a protrusion in LFM image when scanned with a D terminated tip. This indicates that the dangling bond formed by removing the terminating atom has an attraction interaction with the D atom at the tip apex. However, the initial structure of the tip apex before picking up a H atom can vary [175], so the Htip bond is not necessarily identical across all H-functionalized tips. This variability is similar to the differences observed with CO-functionalized tips.

Then, the positions of the atoms and dimer rows were determined via procedure indicated in Fig. 6.8. First, the LFM and STM images were compared, as shown in Fig. 6.8 A. The same region of the surface was scanned using LFM (left side of Fig. 6.8 A) and STM (right side of Fig. 6.8 A). As described before, the dimer rows on the surface are oriented at an angle of 8° relative to the tip oscillation direction, which is indicated with a red arrow in Fig. 6.8 A, B and C. For easier interpretation, the scanned images were rotated by −8° in the analysis. White dots indicate Hydrogen atoms, solid lines trace dimer rows, and dotted lines denote spaces between rows.

Fig. 6.8 B presents the calculated potential energy derived from the Δf image,

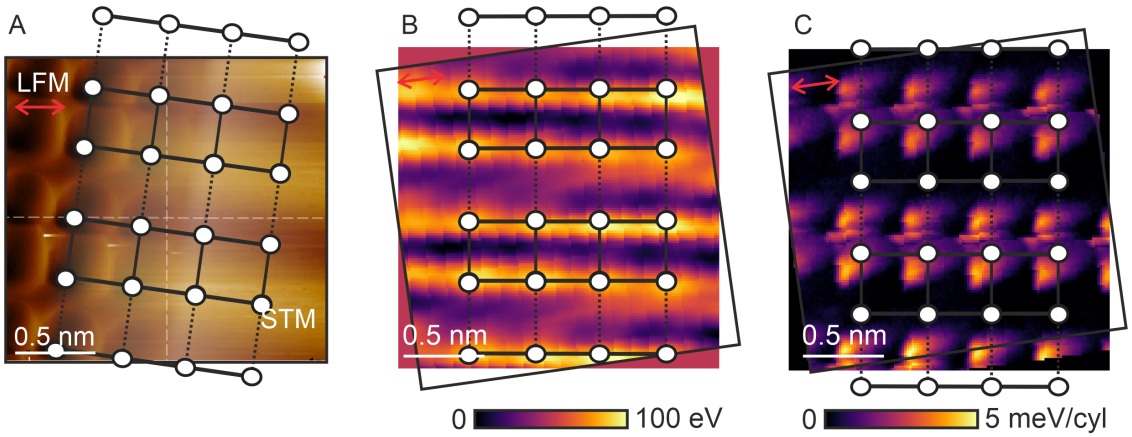

Figure 6.8: Process for finding the location of atoms (A) Same region of D-Si(100) scanned with LFM (left side) and STM (right side). Dimer rows have an angle of 8° relative to the tip oscillation direction. Tip oscillation direction is parallel to the figures. In analysis, scanned images are rotated −8° to help eyes. The white dots are locations of H atoms. The solid lines are guiding the dimer rows, and the dotted lines are corresponding to the space in between the rows. (B) Calculated potential energy from Δf image of (A) using Fourier method. It additionally helps where the atoms and rows should be, qualitatively, while the potential value is not accurate quantitatively. (C) E_{diss} image scanned simultaneously.

shown in the left side of Fig. 6.8 A, using the Fourier method [79]. This helps visualize the arrangement of atoms and rows, though the potential values are not quantitatively accurate. The dimer row locations obtained from Fig. 6.8 A show a slight offset between the STM and LFM images. It is known that AFM and STM images do not always match perfectly [151].

These small discrepancies in atom locations were corrected by comparing with potential energy images. The maximum energy points indicate where the atoms are expected to be. The atom locations determined through this process were then used as references for analyzing the dissipated energy (E_{diss}) image, as shown in Fig. 6.8 C. E_{diss} is calculated from the excitation of the LFM drive and was obtained simultaneously with the LFM Δf image used for Fig. 6.8 B.

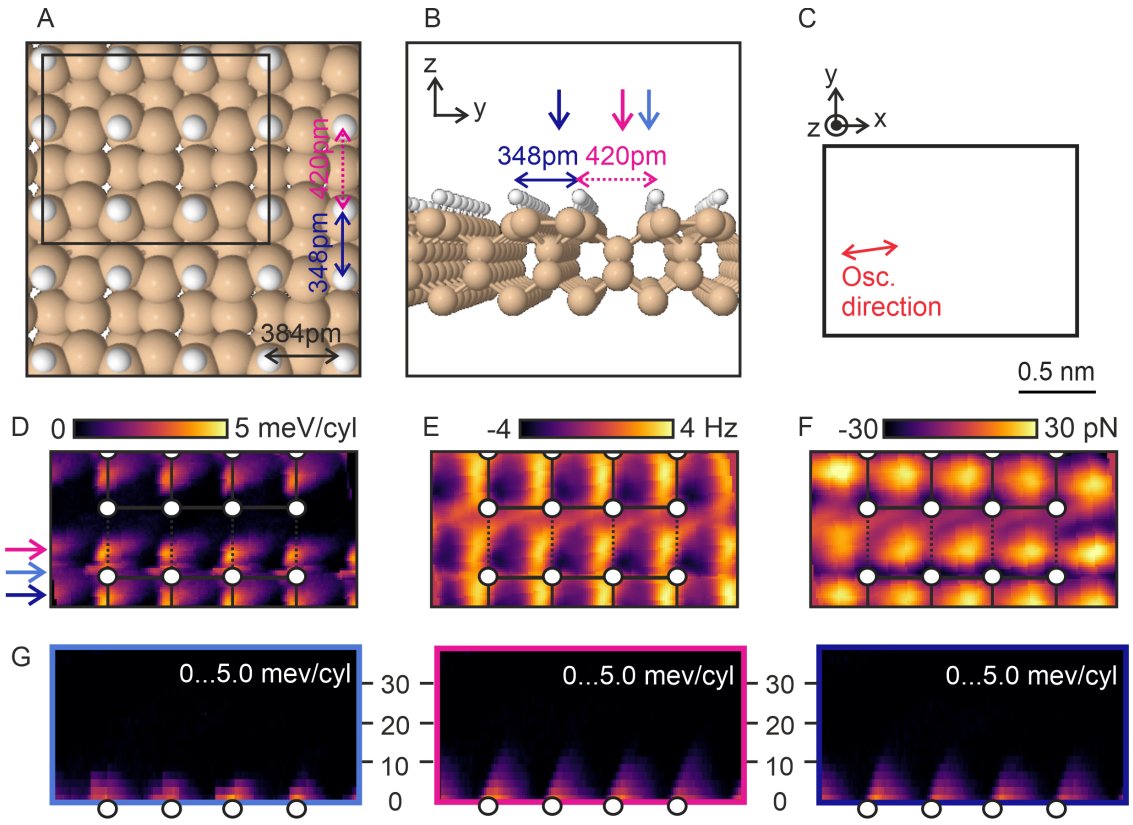

Figure 6.9: 3D data acquired over 2×1 reconstructed D-Si(100) (A) Schematic figure for the top view of the D-Si(100) surface area showing the 2×1 reconstruction. D atoms are indicated with a white color, and Si atoms are indicated with a yellow color. The lattice constant of the bare Si(100) is 543 pm. The distance between dimer rows is 420 pm, and the spacing between individual dimers within the same row is 384 pm and 348 pm. (B) Side view along the y-z direction, where z is the surface normal and y is parallel to the dimer rows. (C) Direction of tip oscillation relative to the (x, y, z) coordinates in (A) and (B). (D)-(F) Images from the 3D data set obtained at the lowest tip height. Data sets are rotated 8 degree from the raw data. (D) Calculated E_{diss}, (E) calculated lateral force using Δf data (F), via the Fourier method [79]. Figure (G) shows extracted images along xz direction from the data set. Arrows in (D) indicate the locations of x axis of each extracted xz planes, with D atoms location (white dots). The dotted line shows the spacing between dimer rows, and the solid line represents the spacing within dimer rows.

Fig. 6.9 shows 3D measurements over D-Si(100) surfaces by changing the tip height. The data were acquired in constant height mode with a height increment of 2 pm. Fig. 6.9 A provides a top view of the measured area on the D-Si(100) surface, which is characterized by a 2×1 reconstruction. D atoms are represented with white color and Si atoms as brown color. This 2×1 reconstruction results from the

surface rearrangement of Si atoms following D termination, which minimizes surface energy. Consequently, the surface unit cell is twice as long in one direction compared to the other, forming a rectangular lattice with dimensions of 2×1. Silicon atoms are paired along the [110] direction, creating a dimer row.

The lattice constant of the Si(100) surface matches the bulk silicon value of approximately 543 pm. The distance between dimer rows is approximately 420 pm, the distance between individual dimers within the same row is 348 pm, and the spacing between adjacent dimers within the same row is about 384 pm [50].

Fig. 6.9 B provides a side view along the y-z direction, with z as the surface normal and y parallel to the dimer rows. Fig. 6.9 C shows the tip oscillation direction relative to the defined coordinates. Fig. 6.9 D-F shows slices from the 3D dataset of D-Si(100) acquired at the lowest tip height. The arrows indicate the measured locations, as shown in Fig. 6.9 A and B, with matching colors. The locations of H atoms are marked by white dots. The dotted line guides the spacing between dimer rows, while the solid line indicates the spacing within the dimer rows.

Fig. 6.9 D shows an E_{diss} image obtained from the excitation data. The E_{diss} image reveals significant dissipation between dimer rows (magenta), over atoms (sky blue), and in the spaces between adjacent dimers within the same row (purple). Fig. 6.9E presents the Δf data used for calculating the lateral force, while Fig. 6.9F shows the calculated lateral force via the Fourier method [79]. Attractive interactions are observed above the atoms and dimer rows, in contrast to the regions between the rows.

Fig. 6.9 G presents extracted images along the xy direction from the data set. The arrows in Fig. 6.9 B and D indicate the locations for each xz plane, highlighted with corresponding colors, with D atoms shown as white dots. z axis is corresponding to the surface normal direction. The dotted line guides the spacing between dimer rows, and the solid line represents spacing within the dimer rows. The data were obtained over a total vertical distance of 40 pm, with a 2 pm increment between each slice, and the indicated numbers in Fig. 6.9 G shows 10 pm tip height differences. Fig. 6.10 shows the lowest 10 slices of full data set. The data was acquired by decreasing the tip heights, until the tip lost D atom at its apex. $z = 0$ pm is defined as the height at which the tip lost its terminated front atom.

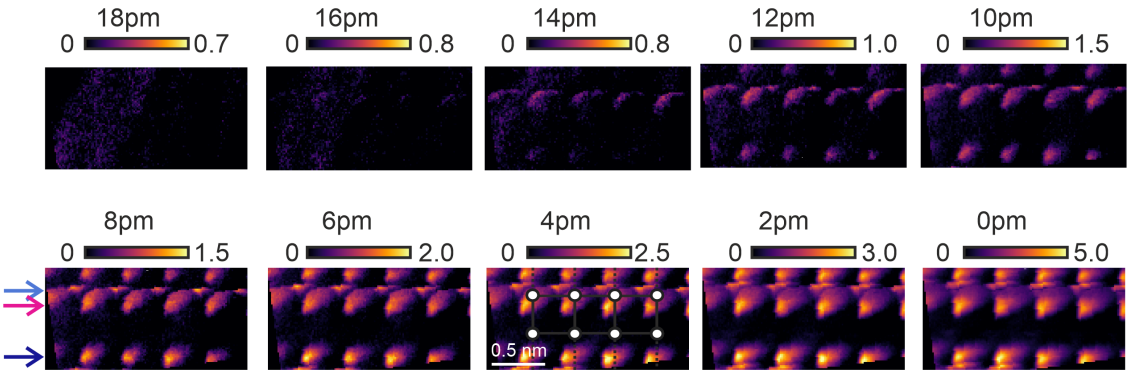

Figure 6.10: Energy dissipation acquired over D terminated Si (100). Dissipated energy, E_{diss}, is acquired from excitation data, by changing the tip height. z = 0 pm is defined as the height that the tip loses the H atom at its apex. The images were acquired for 2 pm tip height differences. Dimer rows are parellel to the oscillation direction. White circles are location of H atoms.

Dissipation initially appeared as a line or rectangular shape over individual atoms at z = 14 pm. As the tip approached the surface, dissipation was also observed over the dimer rows and in the spaces between them, forming a triangular shape. This triangular shape arises because the potential energy varies along the row, depending on the distance to the atoms.

The E_{diss} data for D-Si(100) is then compared with that for H-Si(100). Fig. 6.11 A shows slices of the 3D dataset acquired with single H terminated tip at a tip height of z = 12 pm over H-Si(100). The tip height of z = 0 pm is defined as the position at which the tip loses the H atom at its apex, consistent with the definition used for the tip height in D-Si(100). As mentioned before, the pick up condition was already different, in line with expectations of difference in E_{diss}. The data acquisition process is same with the data set of D-Si(100). D-terminated tip was lost earlier than H-tip for this data set. The colors of the arrows are consistent with those in Fig. 6.9. Magenta indicates the spaces between rows, sky blue indicates the space over atoms, and purple represents the spaces within the same rows.

Dissipation patterns, as shown in the first image of Fig. 6.11 A, are similar to those observed over D-Si(100), with triangular shapes appearing both over and between rows. However, there are differences in the shapes observed in Δf images, shown in the second image of Fig. 6.11 A. These differences may be attributed to variations in the tip apex configuration. Despite thorough checks for single atom pick-up, variations in the tip apex above that single atom can influence imaging.

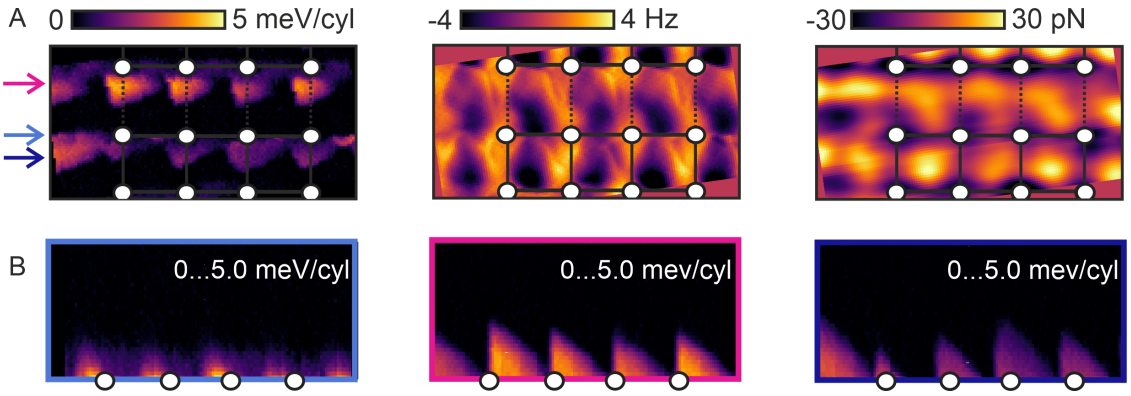

Figure 6.11: 3D data acquired over 2×1 reconstructed H-Si(100) (A) Images from the 3D data set obtained at $z = 0$ pm tip height. Data sets are rotated 8 degree from the raw data. Left figure is E_{diss}, middle one is Δf data used for calculating lateral force, as shown in right. (B) Subtracted E_{diss} images along xy direction from the data set. Arrows in (A) indicate the locations of y axis of each xz planes, with H atoms location (white dots). The dotted line shows the spacing between dimer rows, and the solid line represents the spacing within dimer rows.

For example, variations in the tip's apex or potential contamination can influence the resolved images, revealing additional structural details, such as the underlying silicon atom arrangement. The lateral force image, shown in the third figure of Fig. 6.11 A, is calculated using the Fourier method and exhibits a pattern similar to that observed for D-Si(100) [79]. The image reveals attractive interactions above the atoms and rows, compared to the surrounding areas.

Fig. 6.11 B shows extracted images along the xy direction from the data set. The arrows indicate the y-axis locations for each xz plane, with H atoms shown as white dots. The dotted line guides the spacing between dimer rows, and the solid line represents spacing within the dimer rows. The data were obtained over a total vertical distance of 64 pm, with a 2 pm height difference between each slice. The color scale is used with the same range in Fig. 6.9 G. Fig. 6.12 shows the lowest 19 slices of full data set. The tip height $z = 0$ pm is defined as the height at which the tip loses its H atom at the apex. As the tip height decreases, dissipation begins to appear, initially as lines or rectangular shapes over atoms. As the tip gets closer to the surface, dissipation is also observed over the dimer rows and in the spaces between the rows, forming a triangular shape. This triangular dissipation pattern occurs because the potential energy varies along a row, depending on the distance to the atoms.

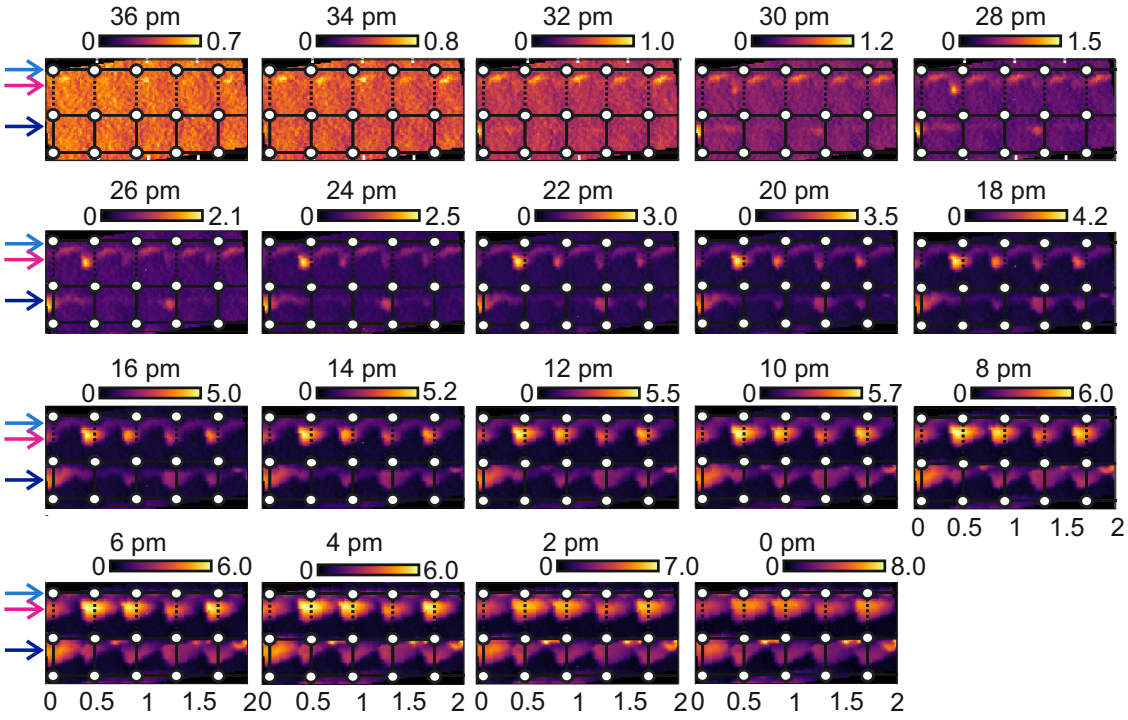

Figure 6.12: Energy dissipation acquired over H terminated Si(100). Dissipated energy, E_{diss}, is acquired from excitation data, by changing the tip height. $z = 0\,\mathrm{pm}$ is defined as the height at which the tip loses its H atom at the apex. The images were acquired for 2 pm tip height differences. Dimer rows are parallel to the oscillation direction. White circles are location of H atoms.

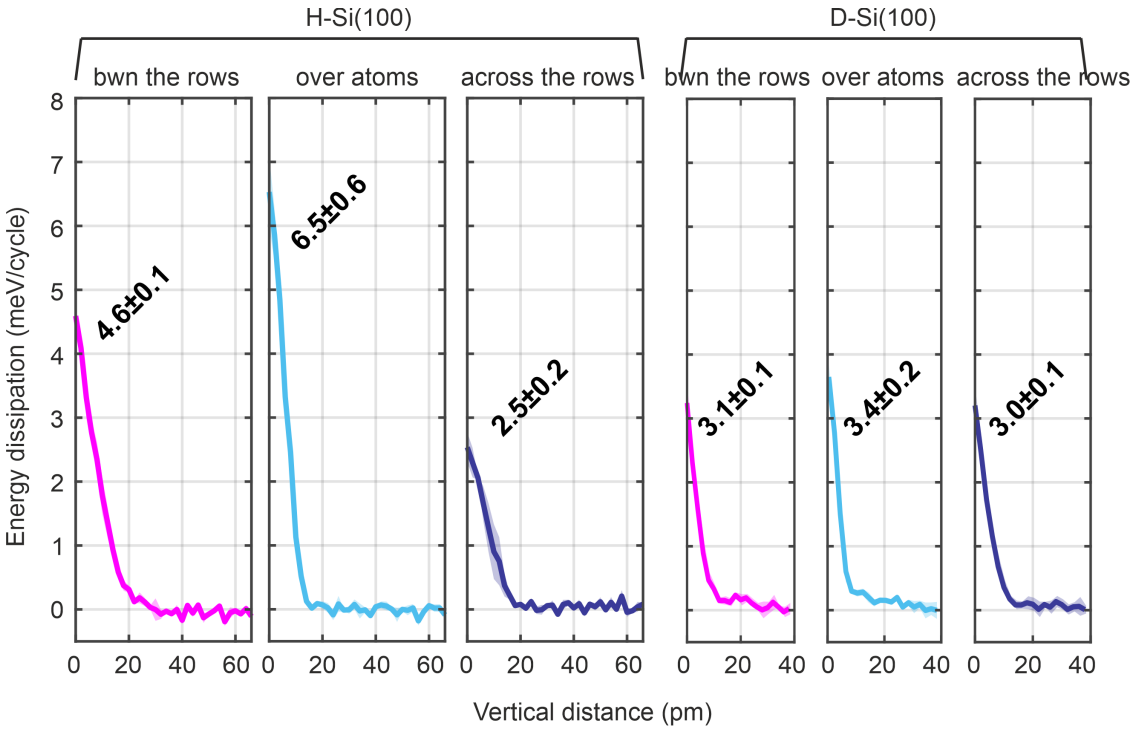

Figure 6.13: Energy dissipation plot as a function of tip height. The maximum E_{diss} values from each slice are plotted as a function of tip height. E_{diss} values were obtained from multiple locations: between dimer rows, directly over atoms, and across dimer rows, represented by magenta, sky blue, and purple colors, respectively. For each yz line, which includes 4 or 5 atoms, E_{diss} values were collected from 4 data points per atom. These data points were averaged, and the standard deviation was calculated to quantify variability. The same methodology was applied to locations across dimer rows and between dimer rows to ensure a comprehensive analysis. The numbers written in the figures indicate the averaged values and the standard deviation values multiplied by 0.5. The tip height $z = 0$ pm is defined as the height at which the tip loses its H or D atom at the apex.

To quantitatively compare the dissipation behaviors of D- and H-terminated Si(100) surfaces, the maximum E_{diss} values from each slice are plotted as a function of tip height, as shown in Fig. 6.13. These E_{diss} values were obtained from multiple locations, including positions directly over atoms, across dimer rows, and between dimer rows, as previously indicated with arrows. In each yz line, which includes four atoms, the E_{diss} were collected for each atom. These data points were averaged to provide a representative value for each slice. Additionally, the standard deviation was calculated to quantify the variability. The same process was applied to the other locations: across dimer rows and between dimer rows.

The grid sizes are kept the same for both the x- and y-axes in H- and D-terminated Si(100) for the accurate comparison. Compared to CO tips, single H/D tips are more prone to losing their apex atoms, making it challenging to obtain a complete dataset of $E_{\mathrm{diss}}(\mathrm{z})$. Despite this, the data at $\mathrm{z} = 0\,\mathrm{pm}$, defined as the height at which a single H/D atom is lost from the tip apex, can still be compared. Additionally, the plots are fitted with an exponential function to analyze the trends.

Applying the model introduced in appendix .2, H/D can be modeled as an atom colliding with a Si atom at the surface. According to Eq .10 in appendix .2, the ratio of energy dissipation between H and D is given by:

$$\frac{E_{\mathrm{H}}}{E_{\mathrm{D}}} \approx \frac{m_{\mathrm{D}}}{m_{\mathrm{H}}} = \frac{2.014\mathrm{u}}{1.008\mathrm{u}} \approx 2.00 \tag{6.6}$$

The dissipation ratios for H and D atoms can be determined by analyzing the maximum values of the dissipated energy (E_{diss}) at $\mathrm{z} = 0\,\mathrm{pm}$ from the data shown in Fig. 6.13. The ratio of dissipated energy for measurements taken between the rows is calculated as $\frac{dE_{\mathrm{H}}}{dE_{\mathrm{D}}} = \frac{4.6}{3.1} \approx 1.48$. This indicates that the energy dissipation for Hydrogen is approximately 1.48 times greater than that for Deuterium in these regions. For measurements taken directly over the atoms, the ratio is $\frac{dE_{\mathrm{H}}}{dE_{\mathrm{D}}} = \frac{6.5}{3.4} = 1.91$. Here, the energy dissipation for Hydrogen is about 1.91 times greater than that for Deuterium. This value is closer to the theoretical expectation of 2.00, which suggests that the observed dissipation is more aligned with theoretical predictions when measuring directly over atoms. The dissipation ratio for measurements taken across the rows is $\frac{dE_{\mathrm{H}}}{dE_{\mathrm{D}}} = \frac{2.5}{3.0} = 0.83$. In this case, the energy dissipation for Hydrogen is lower than that for Deuterium, with a ratio of 0.83. This observation is inconsistent with the expected ratio and suggests that other factors may be influencing the dissipation measurements in these regions.

To summarize, the theoretical dissipation ratio, based on the mass difference between Hydrogen and Deuterium, is approximately 2.00. This value reflects the expected difference in energy dissipation due to the mass discrepancy between these isotopes. Measurements obtained directly over atoms align reasonably well with the theoretical value of 2.00, indicating that the theory well predicts the dissipation behavior in these regions. However, the dissipation ratios obtained from regions between and across the rows exhibit greater deviation from the theoretical value. The observed dissipation ratios in other regions, particularly between and across the

rows, exhibit large deviations from the previous model [139]. Despite the similarities in some measurements, the calculated values do not always adhere strictly to neither the theoretical predictions [140] and previous experimental results [139].

Nevertheless, compared to measurements involving $^{12}C^{16}O$ and $^{12}C^{18}O$, where the differences in dissipation were relatively minor, the differences observed in the dissipation ratios for Hydrogen and Deuterium are significantly more pronounced. This more pronounced difference between isotopes is likely due to the substantial mass difference between Hydrogen and Deuterium, which amplifies the effect on energy dissipation.

The $E_{\mathrm{diss}}(z)$ plots are further analyzed by fitting the data with an exponential function, as shown in Fig. 6.14. The plots display averaged data for each location as dots, with the exponential fit represented by a red solid line. The left column of the figure corresponds to measurements on H-Si(100), while the right column shows measurements on D-Si(100). The grid sizes on the axes are consistent across all the plots. Fig. 6.14 A involves measurements taken between the dimer row. Fig. 6.14 B is for the measurements directly over the atoms, and Fig. 6.14 C covers measurements taken across the rows.

In the exponential fit, the vertical distance of the tip (x) is plotted against the averaged E_{diss} (y). The parameter multiplied by x in the exponent, the exponent's coefficient, is larger for measurements on D-Si(100) compared to H-Si(100) for Fig. 6.14 A and B. This indicates a more rapid increase in E_{diss} as a function of tip height for the D-Si(100) sample, suggesting a significant difference in dissipation behavior between the two surfaces.

The rapid increase in E_{diss} observed for the D-Si(100) sample can be interpreted as indicative of the vibrating with higher frequencies and lighter nature of the H atoms compared to the D atoms. This means the H atoms to interact with a wider range of tip heights, resulting in a more wider peak in $E_{\mathrm{diss}}(z)$. This tendency is similar to observations with isotopes of a CO tip, where lighter isotopes of CO also exhibited a wider peak width in their measurements as shown in section 6.1. The similarity suggests that, just as lighter CO isotopes show a broader range of interaction due to their lower mass, the D atoms on the silicon surface show a more extensive response due to their larger mass.

However, the friction measurements over H/D-Si(100) were obtained using different tips, either H-terminated or D-terminated. Both tips are chemically less

inert than a CO tip and lost their frontier atom quickly before completing the full 3D data acquisition. Further research is recommended on a mixed H/D-Si surface using the same tip or a CO-functionalized tip, which is more chemically inert.

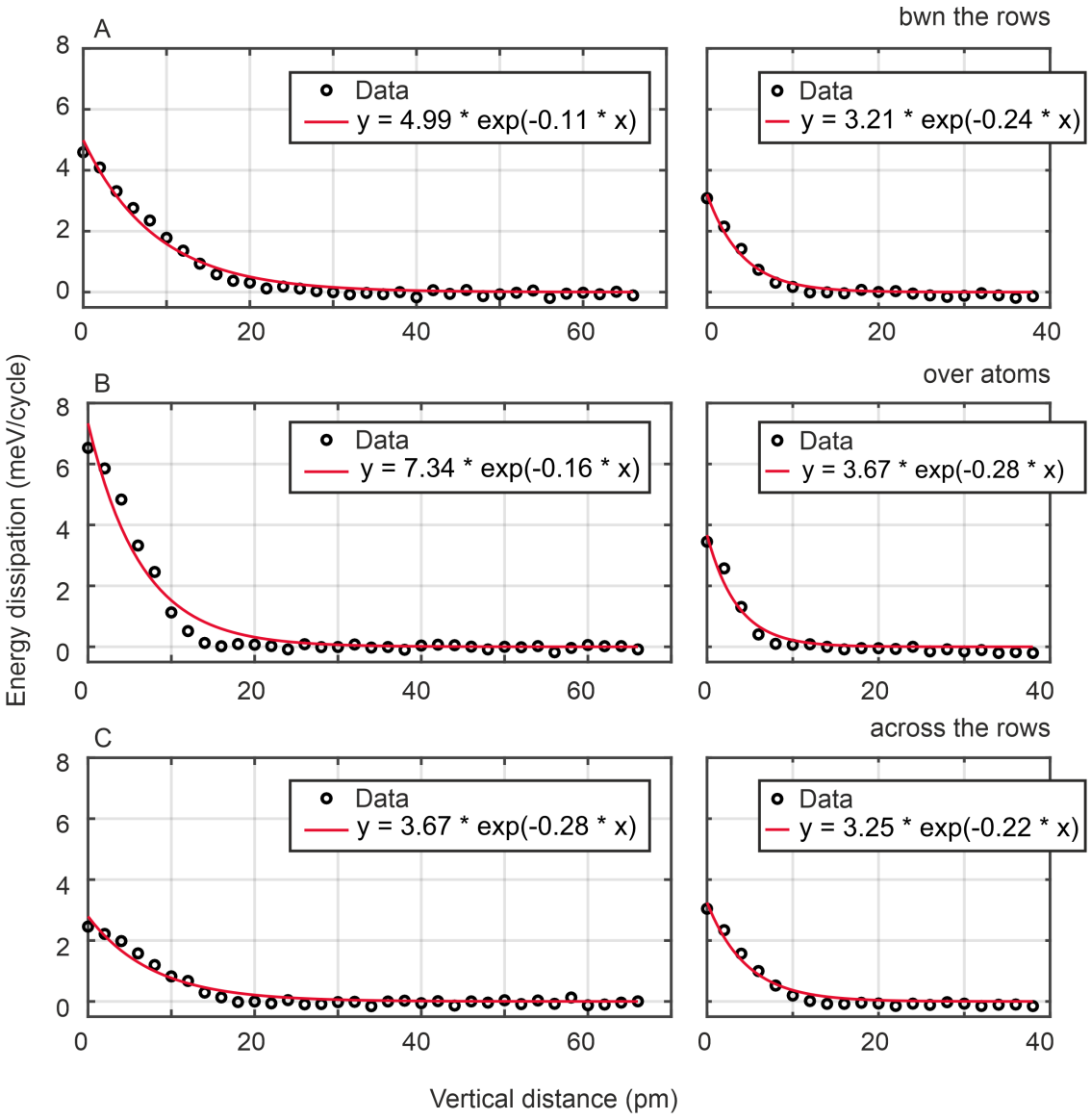

Figure 6.14: Energy dissipation plot with an exponential fit. The $E_{\text{diss}}(z)$ plots are analyzed by fitting the data with an exponential function. The data measurement taken between the dimer rows (A), over atoms (B), and across the dimer rows (C). The plots display averaged data for each location as dots, with the exponential fit represented by a red solid line. The left column shows measurements on H-Si(100), while the right column displays measurements on D-Si(100). The grid sizes on the axes are consistent across all plots.

6.4 Discussion

This chapter provides a thorough exploration of phononic contributions to friction at atomic and molecular scales, with a particular focus on the role of isotopic variations. By using different isotopes, the study isolates and examines these phononic contributions, revealing how variations in atomic mass influence energy dissipation. In the first experiment, isotopes of $^{12}C^{16}O$ and $^{12}C^{18}O$ are used for the tip functionalization and scanned the same chemical bond. The experimental results indicate that the measured dissipated energy is not much different between the isotopes. However, the mass difference between $^{12}C^{16}O$ and $^{12}C^{18}O$ is very small, with a ratio of 1.07, making it difficult to detect and insufficient for drawing conclusions.

Therefore, the experiment extends to the Si(100) surface terminated with Hydrogen and Deuterium, which have a larger mass difference ratio of 2. Hydrogen-terminated Si(100) surfaces exhibit a greater frictional response and a broader range of energy dissipation compared to Deuterium-terminated surfaces, as determined by exponential fitting. These findings align well with theoretical predictions in appendix .2, concerning phononic friction, supporting the idea that lighter atoms contribute more significantly to frictional interactions due to their higher vibrational frequencies. However, the ratio does not always align with the theoretical value across the entire scanned area, although it matches relatively better when measured directly over the atoms. This discrepancy may explain the differing conclusions in previous studies [141–144], both theoretical [140] and experimental [139], and suggests further investigation with a precise calculation. While the previous studies under debate involved systems with many atoms, at single-atom resolution, friction varies with picometer scale distance differences.

These findings underscore the critical role of atomic and molecular mass in determining frictional properties. By utilizing isotopic variations and precise friction measurements, the study discusses the phononic contributions to energy dissipation, providing a foundation for future investigations into friction mechanisms at the nanoscale.

7 Summary and outlook

This thesis presents the understanding of friction at the single-atom scale by using LFM, based on the qPlus sensor. The atomic interaction mechanisms that are relevant for the LFM contrast and dissipated energy in measurements have been analyzed in detail as a function of the tip-sample distance. By investigating various factors like tip functionalization, chemical bonds, and isotopic variations, each chapter has provided insights into the mechanisms governing friction at single atomic and molecular levels.

In chapter 4, the use of radially symmetric atomic interactions for a CO-terminated tip is validated, showing that these interactions are consistent across a wide range of angles relative to the surface. The results highlight that while radial functions like Morse or Lennard-Jones potentials are effective for describing short-range interactions, the influence of the metal dipole on electrostatic interactions must also be considered for accurate AFM data interpretation. Additionally, the chapter demonstrated that LFM is effective in visualizing Hydrogen atoms, which are challenging to detect with normal AFM methods. This capability is important for studying terminal molecular features and improving the understanding of molecular interactions.

Chapter 5 extended this work by quantitatively characterizing the energy dissipation over individual chemical bonds, including covalent and hydrogen bonds. Through the use of CO-functionalized tips and DFT simulations, the molecular snapping mechanism was confirmed. This chapter highlighted the role of bond order in energy dissipation, showing that higher bond orders lead to greater frictional energy losses. The findings provide a deeper understanding of how atomic-scale interactions contribute to friction, especially in systems with varying bond types and molecular orientations. The linear relationship observed between bond order and dissipation further reinforces the impact of bond properties on frictional behavior.

Chapter 6 explored the role of atomic mass and isotopic variations in phononic

friction. The experiments demonstrated that lighter isotopes does not always exhibit greater energy dissipation compared to heavier isotopes. This was previously explained with a simple theoretical models of phononic friction [139] and was further debated by molecular dynamics caculations [141]. By measuring the friction on H/D terminated Si(100) surfaces, this chapter demonstrated the importance of the single-atom resolution to finish the debate. The greater energy dissipation observed with hydrogen-terminated surfaces underscores the influence of atomic mass on frictional properties. However, discrepancies in energy dissipation measurements across different scanned areas suggest that further research is needed with a same tip and fully understand nanoscale friction mechanisms.

Friction research is often associated with its practical implications, but it is crucial to acknowledge the complex physics underlying these phenomena. Despite significant advancements, such as the introduction of Friction Force Microscopy (FFM) [8–11, 13] and frequency-modulation AFM, friction study with single-atom resolution using a true single atom tip apex has proven difficult. Recent developments, including the use of the qPlus sensor and functionalized tips [36, 53–55], have enhanced our ability to measure atomic-scale friction and in-plane forces with greater precision.

The findings of this thesis highlight the importance of continuing to refine experimental techniques and theoretical models. Atomic-scale friction remains a semi-phenomenological field where microscopic dissipation mechanisms are not yet fully integrated with experimental observations. There is a need to better understand how energy and momentum losses become irretrievable and how mechanical energy transitions to heat. Additionally, new approaches are needed to explore friction mechanisms across various timescales, from femtoseconds to microseconds [176, 177]. While this thesis has provided valuable insights into atomic-scale friction, addressing the remaining challenges and expanding the scope of research will be essential for achieving a comprehensive understanding of frictional phenomena at both nanoscale and larger scales.

In summary, this work has made significant strides in elucidating the intricacies of atomic-scale friction. However, ongoing research and advancements are necessary to fully unravel the complexities of energy dissipation and friction mechanisms, paving the way for both fundamental physics and practical applications in tribology.

Appendix

.1 MATLAB code scripts used in chapter 4

.1.1 The new model introduced in section 4.2.2

```
clear all;

%Parameters of the Morse potential
EB = 1.346e-21;      %Bond energy [J]
sigma = 354e-12;     %Bond length [m]
lambda = 47e-12;     %Bond decay length [m]

%Torsional spring constant of COs
kt1 =150e-21;        %Torsional spring constant of CO on
   surface [Nm]
kt2 = 22e-21;        %Torsional spring constant of CO on tip [
   Nm]

%Additional parameters and constants
l = 302e-12;         %Moment arm of CO (Cu core - O core) [m]
ke = 8.988e9;        %Coulomb constant [N m^2 / C^2]
D = 1/299792458*1e-21; %Debye -> Coulomb meter
pmetal = 5*D;        %Metal dipole moment, where positive
   number means positive charge at the apex (i.e. correct
   direction)
pco = 0.166*D;       %Tip CO dipole moment, where positive
   number means negative charge at CO apex (i.e. correct
   direction)
```

```
psurf =  -0.8*D;    %Surface CO dipole moment, where positive number means positive charge at O atom (after Schwarz et al APL 2014)

%Analysis parameters
dx = 3e-12;         %Lateral step size [m]
x0 = -100e-12;      %Starting lateral position
totcntX = 1000;     %Number of data points of Fx that are pre-calculated based on the dx (above) and x0
zpos = 570e-12;     %Height of the metal apex above the surface

xvec = [];          %Initialize to zero

tic;
%At each lateral (pseudo-radial) position, calculate the force on the tip.
for cnt1 = 1:totcntX
    %The lateral position
    x = x0 + (cnt1-1)*dx;
    xvec(cnt1) = x;

    %Allow the CO molecules to relax at this point
    [theta1, theta2, Uhere] = TwoSprings3Dipoles(x, zpos, kt2, sigma, pmetal, pco, psurf);

    %Save the angles and the potential energy here
    theta_tip(cnt1) = theta2;
    theta_sample(cnt1) = theta1;
    Umat1D(cnt1) = Uhere;
    th1 = theta1 * pi / 180;%sample CO
    th2 = theta2 * pi / 180;%tip CO

    %Now to calculate the forces. First we calculate distances
    %Distance between the two O atoms
```

```
47      Dx = x - (l)*sin(th1) - (l)*sin(th2);
48      Dz = zpos - (l)*cos(th1) - (l)*cos(th2);
49      d = sqrt(Dx^2 + Dz^2);
50      phi = atan2(Dx,Dz);
51      th3 = th2 - th1; %Angle between the two dipole directions
52
53      %Distance from O at surface to metal tip atom
54      Dx2 = x - (l)*sin(th1);
55      Dz2 = zpos - (l)*cos(th1);
56      d2 = sqrt(Dx2^2 + (Dz2^2));
57      phi2 = atan2(Dx2,Dz2);
58      th_2 = pi - th1;
59
60      %The distance between O atoms yields the force of the
           Morse interaction
61      Fmorse = EB*(1/(lambda))*(-2*(exp(-(d-sigma)/(lambda))) +
            2*exp(-2*(d-sigma)/lambda));
62
63      %The dipole-dipole interaction between the O atoms
64      Fdd = 0;
65      if (d > 10e-12)
66          Fdd = ke*(pco)*(psurf)*(cos(th3)-3*cos(phi-th1)*cos(
               phi-th2+pi))/(d)^4;
67      end
68
69      %The force on the metal tip apex from the surface dipole
70      Fdd2 = ke*(pmetal)*(psurf)*(cos(pi-th1)-3*cos(phi2-th1)*
           cos(pi-phi2))/(d2)^4;
71
72      %Total lateral force is a combination of the forces with
           the
73      %appropriate contributions
74      Ftot(cnt1) = Fmorse*(Dx/d) + Fdd*(Dx/d) + Fdd2*(Dx2/d2);
75      FM(cnt1)= Fmorse*(Dx/d);
76      FDD1(cnt1) = Fdd*(Dx/d);
77      FDD2(cnt1)= Fdd2*(Dx2/d2);
```

```
78 end
79 toc
80 %%Now we will use the calculated lateral forces as a lookup
       table to
81 %%populate an entire image in X and Y.
82
83 %linescan_X = 800;
84 linescan_dx = 5e-12; %1e-12
85 linescan_x0 = 0;
86 linescan_xend = 800e-12;
87 df_x = linescan_x0:linescan_dx:linescan_xend;
88 linescan_X = length(df_x);
89
90 %linescan_Y = 800;
91 linescan_dy = 5e-12; %1e-12
92 linescan_y0 = 0;
93 linescan_yend = 800e-12;
94 df_y = linescan_y0:linescan_dy:linescan_yend;
95 linescan_Y = length(df_y);
96
97 %Sensor parameters
98 f0 = 37419;
99 k = 889;
100 A = 50e-12;
101
102 %Conversion to time - we will simulate an oscillation at each
       position
103 totcnt = 200;%500       %Number of pixels in an individual
       oscillation (used for calculation of Df)
104 T = 1/f0;
105 t = ((1:totcnt)-1)*(T/totcnt);
106 q_osc = A*cos(2*pi*f0*t);
107
108 %Initializing vectors
109 df = [];
110 df2D = [];
```

```
Ftot1D = [];
Ftot2D =[];

f = waitbar(0, 'Calculating Df image');
for cnty = 1:linescan_Y
    y = df_y(cnty);
    for cnt2 = 1:linescan_X
        %q_here is the average x position
        q_here = df_x(cnt2);

        %The average lateral distance is
        distance = sqrt(q_here^2 + y^2);
        %The distance during an oscillation is
        x_osc = q_here + q_osc;
        q_prime = sqrt(x_osc.^2 + y^2);

        %Now interpolate the previously-calculated lateral
           force
        Fts = interp1(xvec, Ftot, q_prime); %Vector along
           oscillation
        %This angle is required for the correct component
        %Calculate the angle between x and y during the
           oscillation
        th_xy_vec = atan2(y,x_osc);
        %Use that to determine the x-component of force
        Fxtot = Fts.*cos(th_xy_vec);
        %We also want the average force for the components,
           so calculate a
        %as a scalar
        th_xy = atan2(y,q_here);

        %%%%%%%%%%For the components, only extract the force
            at the
        %%%%%%%%%%average lateral distance
        Fts2 = interp1(xvec, Ftot, distance);%%
        Fxtot2 = Fts2.*cos(th_xy);
```

```
142         Ftot1D(:,cnt2) = Fxtot2;
143
144 %         FtsLJ = interp1(xvec, FLJ, distance);%%
145 %         FLJ1D(:,cnt2) = FtsLJ.*cos(th_xy);
146
147         FtsDD1 = interp1(xvec, FDD1, distance);%%
148         FDD11D(:,cnt2) = FtsDD1.*cos(th_xy);
149
150         FtsDD2 = interp1(xvec, FDD2, distance);%%
151         FDD21D(:,cnt2) = FtsDD2.*cos(th_xy);
152
153         %%%%%%%%%%%%%%%%%%%%%%%%%
154
155         Fx_avg = trapz ( t, Fxtot.*cos(2*pi*f0*t));
156         df(:,cnt2) = -1*f0*f0/(k*A).*Fx_avg;
157     end
158     waitbar(cnty/linescan_Y, f)
159     Ftot2D(:,cnty) = Ftot1D;
160 %     FLJ2D(:,cnty) = FLJ1D;
161     FDD12D(:,cnty) = FDD11D;
162     FDD22D(:,cnty) = FDD21D;
163
164     df2D(:,cnty) = df;
165 end
166 close(f)
167 figure
168 imagesc(df2D)
169 colormap gray
170 axis equal tight xy
171 colorbar
172 %caxis([-3e-21 10e-21])
173
174
175 %% Function
176 function [theta1, theta2, energy] = TwoSprings3Dipoles(xtip,
    ytip, kt2, sigma,pmetal,pco,psurf)
```

```
177
178 EB = 1.346e-21; %J
179 % EB = 8.4e-3;%eV
180 %sigma = 359.38e-12;
181
182 lambda = 47e-12;
183 tran = 6.242e18;%ev=1J
184 % EB2 = 1.346e-21*358/142;
185 % sigma2 = 536e-12;
186
187 kt1 =150e-21;
188 %theta1=sample CO
189 %kt2 = 60e-21;
190 l = 302e-12;
191 ke = 8.988e9;
192 D = 1/299792458*1e-21; %C*m
193
194 %Here is where the fun begins!
195 U = [];
196 for cnt1 = 1:181
197     for cnt2 = 1:181
198         %Convert from counter to degrees
199         theta1 = cnt1-91;
200         theta2 = cnt2-91;
201         %Convert from degrees to radians
202         th1 = theta1 * pi / 180;
203         th2 = theta2 * pi / 180;
204         USpring1 = 0.5 * kt1 * th1^2;
205         USpring2 = 0.5 * kt2 * th2^2;
206         %dipole - dipole distance
207         [d, d2, phi, phi2, th3] = Ruler(th1, th2, xtip, ytip,
                l);
208
209         UMorse = EB*(-2*(exp(-(d-sigma)/(lambda))) + exp(-2*(
              d-sigma)/lambda));
210
```

```
211         %% Here I include the term for the interaction bwn
               two dipoles. Pco=0.166D (on the tip)
212
213         Udd = 0;
214         if (d > 10e-12) %only if the distance between O-O
               cores is more than 10 pm, then add the dipole
               interaction
215             %Between the O atoms. Otherwise, it (NON-
                   PHYSICALLY) dominates
216             %the interaction
217             Udd = ke*(pco)*(psurf)*(cos(th3)-3*cos(phi-th1)*
                   cos(phi-th2+pi))/d^3;
218         end
219         Udd2 = ke*(pmetal)*(psurf)*(cos(pi-th1)-3*cos(phi2-
               th1)*cos(pi-phi2))/d2^3;
220
221
222         U(cnt1, cnt2) = UMorse + USpring1 + USpring2 + Udd +
               Udd2 ;
223 end
224
225 [minU,ind] = min(U(:));
226 [m,n] = ind2sub(size(U),ind);
227 theta1ans = m - 91;
228 theta2ans = n - 91; %%%@error?? theta2ans = n - 91;
229 energyans = min(min(U));
230
231 end
232
233 %Another loop for higher precision!
234 U = [];
235 for cnt1 = 1:201
236     for cnt2 = 1:201
237         %Convert from counter to degrees
238         theta1 = theta1ans - (cnt1-101)/100;
239         theta2 = theta2ans - (cnt2-101)/100;
```

```
240         %Convert from degrees to radians
241         th1 = theta1 * pi / 180;
242         th2 = theta2 * pi / 180;
243         USpring1 = 0.5 * kt1 * th1^2;
244         USpring2 = 0.5 * kt2 * th2^2;
245         %dipole - dipole distance
246         [d, d2, phi, phi2, th3] = Ruler(th1, th2, xtip, ytip,
                l);
247
248         UMorse = EB*(-2*(exp(-(d-sigma)/(lambda))) + exp(-2*(
               d-sigma)/lambda));
249
250         %% Here I include the term for the interaction bwn
               two dipoles. Pco=0.166D (on the tip)
251
252         Udd = 0;
253         if (d > 10e-12) %only if the distance between O-O
               cores is more than 10 pm, then add the dipole
               interaction
254             %Between the O atoms. Otherwise, it (NON-
                   PHYSICALLY) dominates
255             %the interaction
256             Udd = ke*(pco)*(psurf)*(cos(th3)-3*cos(phi-th1)*
                   cos(phi-th2+pi))/d^3;
257         end
258         Udd2 = ke*(pmetal)*(psurf)*(cos(pi-th1)-3*cos(phi2-
               th1)*cos(pi-phi2))/d2^3;
259
260
261     U(cnt1, cnt2) = UMorse+ USpring1 + USpring2 + Udd + Udd2
           ;
262     end
263 end
264
265 [maxU,ind] = min(U(:));
266 [m,n] = ind2sub(size(U),ind);
```

```
267 theta1 = theta1ans - (m-101)/100;
268 theta2 = theta2ans - (n-101)/100;
269 energy = min(min(U));
270 end
271
272
273 %% Function
274 function [dCOCO, dCOTip, phiCOCO, phiCOTip, th3] = Ruler(th1,
        th2, x, z, l)
275     %Assuming that th1 is the tilt angle of the surface CO
            from +z
276     %Assume th2 is the tilt angle of the CO on the tip from -
            z
277     %All angles are in radians
278
279     %Distance between O atoms and angle from +z
280     Dx = x - (l)*sin(th1) - (l)*sin(th2);
281     Dy = z - (l)*cos(th1) - (l)*cos(th2);
282     dCOCO = sqrt(Dx^2 + Dy^2);
283     phiCOCO = atan2(Dx,Dy);
284
285     %Distance between surface O and tip apex
286     Dx2 = x - (l)*sin(th1);
287     Dy2 = z - (l)*cos(th1);
288     dCOTip = sqrt(Dx2^2+Dy2^2);
289     phiCOTip = atan2(Dx2, Dy2);
290
291     %Angle between two COs
292     th3 = th2 + pi - th1;
293 end
```

Listing 1: The new model includes electrostatic interactions between a CO adsorbate and two dipoles: one located at the metal tip apex and the other at the CO tip apex. The total interaction encompasses the Morse interaction between the two Oxygens with known parameters, bending CO molecules treated as torsional springs, and dipole-dipole interactions between the dipoles. Two CO molecules and the metal tip apex are treated as dipoles, as described in section 4.2.2. The CO dipole is allowed to tilt, whereas the metal tip dipole is not.

.1.2 Determination of the mean square error shown in Fig. 4.3

```
clear all;

EB = 1.346e-21; %J
sigma = 340e-12;
lambda = 47e-12;

kt1 =150e-21;%150zNm
kt2 = 22e-21;%22zNm

l = 302e-12;%302pm
ke = 8.988e9;
D = 1/299792458*1e-21;
pmetal = 0; %Positive number means positive charge at the
   apex (i.e. correct direction)
pco = 0; %Positive number means negative charge at CO apex (i
   .e. correct direction)
psurf = 0; %Positive number means positive charge at O atom (
   i.e. Schwarz et al APL 2014)

dx = 3e-12;
x0 = -100e-12;

totcntX = 1000; %Number of data points that we pre-calculate
   of Fx based on the dx (above) and x0
totcnt = 500; %Number of pixels in an individual line scan
ypos = 560e-12;
imgnumber = 14;

xvec = [];
% imgnumber = 16;
for cnt1 = 1:totcntX
    x = x0 + (cnt1-1)*dx;
    xvec(cnt1) = x;
```

```
30      [theta1, theta2, Uhere] = TwoSprings3Dipoles(x, ypos, kt2
            , sigma,pmetal,pco,psurf);
31
32      Umat1D(cnt1) = Uhere;
33      theta_tip(cnt1) = theta2;
34      theta_sample(cnt1) = theta1;
35
36      th1 = theta1 * pi / 180;%sample CO
37      th2 = theta2 * pi / 180;%tip CO
38
39      %% from here, forces at the minU point
40      xtip = x;
41      ytip = ypos;
42
43      %dipole - dipole distance
44      Dx = xtip - (l)*sin(th1) - (l)*sin(th2);
45      Dy = ytip - (l)*cos(th1) - (l)*cos(th2);
46      d = sqrt(Dx^2 + Dy^2);
47      phi = atan2(Dx,Dy);
48
49      FSpring1 = -1*kt1 * th1;
50      FSpring2 = -1*kt2 * th2;
51      Fmorse = EB*(1/(lambda))*(-2*(exp(-(d-sigma)/(lambda))) +
            2*exp(-2*(d-sigma)/lambda));
52
53
54
55      FM(cnt1) = Fmorse*(Dx/d);
56      FS1(cnt1) = FSpring1*(Dx/d);
57      FS2(cnt1) = FSpring2*(Dx/d);
58
59      theta_sample(:,cnt1) = theta1;
60      theta_tip(:,cnt1) = theta2;
61      Fxtot(cnt1) = Fmorse*(Dx/d);
62  end
63
```

```
linescan_N = 750;
linescan_dx = 1e-12;
linescan_x0 = 0;

f0 = 37419;
k = 1343;
A = 50e-12;

T = 1/f0;
dt = T/totcnt;
t0 = 0;

t = ((1:totcnt)-1)*(T/totcnt);
df = [];
df_x = [];

for cnt2 = 1:linescan_N
    q_here = linescan_x0 + linescan_dx*(cnt2-1);
    df_x(cnt2) = q_here;
    q_prime = q_here + A*cos(2*pi*f0*t);
    Fts = interp1(xvec, Fxtot, q_prime);
    Fx_avg = trapz ( t, Fts.*cos(2*pi*f0*t));
    df(cnt2) = -1*f0*f0/(k*A).*Fx_avg;
end

nfiles = 46;
fbasename = 'C:\Users\LocalAdmin\Desktop\2021-08-26\
   Cu111_3D2_COR_';
DfMat = [];
%Load data
for cnt = 1:nfiles
    %Load image
    fname = [fbasename, num2str(cnt, '%03d'), '.sxm'];
    [hdr, df_dat] = loadsxm(fname, 14);
    %Store the df image
    DfMat(:,:,cnt) = df_dat;
```

```
end
dx_dat = hdr.scan_range(1)/hdr.scan_pixels(1);
dy_dat = hdr.scan_range(2)/hdr.scan_pixels(2);

zline = dx:dx:(dx*size(DfMat, 2));
f0 = hdr.osc_ctrl_ctr_freq;
A = hdr.osc_ctrl_amp_setp;

DfMatSm = imgaussfilt3(DfMat,1);
xzSlicedf = DfMatSm(144,:,:);
xzSlicedf = reshape(xzSlicedf, size(DfMatSm,2),size(DfMatSm
    ,3));


%%cal error
xOffset = 200e-12;
X = xOffset:dx_dat: xOffset + dx_dat*(size(xzSlicedf,1)-1);
xzLine = xzSlicedf(:,imgnumber);

sum=0;
for cnt = 1:size(X,2)

    Mod = df(round(X(cnt)*1e12));
    Dat = xzLine(cnt);

    val = (Mod-Dat)^2;
    Val(cnt) = val;
    sum = sum + val;

end
mse = sum/(size(X,2));

figure;plot(1e12*df_x,df);
hold on;plot(X*1e12,xzSlicedf(:,imgnumber));
title(['tip height = ', num2str(ypos),'/ MSE = ', num2str(mse)
    ,'/ im# = ', num2str(imgnumber)]);
```

```
133
134 val_mse = [0.4093 0.5522 0.8268 1.1864 1.2753 1.3633];
135 height = [535:5:560];
136 height=fliplr(height);
```

Listing 2: To determine the discrepancy between the data and the previous model, the function used here is the same as the one included in the code .1.1, but without the electrostatic interaction.

.1.3 Determination of the bond length (σ) shown in Fig. 4.2

```
clear all;

%% load and smooth f-data
fbasename = 'C:\Users\LocalAdmin\Desktop\2021-10-18\
   Cu111_3D_AT_';
nfiles=35;
f0 = 37421;%19
k=1343;%N/m
Amp=50e-12;
Uj=1.6022e-19;
for cnt = 1:nfiles
    %substract back ground image
    fname = [fbasename, num2str(cnt, '%03d'), '.sxm'];
    [A, imgdforig] = loadsxm(fname, 14);
    offset = mean(mean(imgdforig(118:128, 1:10)));
    imgdf = imgdforig - offset;

    %image filter
    H = fspecial('average', [2 2]);
    imgdfsm = imfilter(imgdf, H);

    %meters per pixel
    mpp = A.scan_range(1) / A.scan_pixels(1);

    %find the minimum point of the image to define as a ref.
       point
    %for correct the drift
    [tmp, tmp2] = min(imgdfsm(:));
    [xmin, ymin] = ind2sub([size(imgdfsm, 1) size(imgdfsm, 2)
       ], tmp2);

    %Select the data by defining 'n' refer to the ref.point
    %Rotate the matrix
```

```
    %since our scan direction is 90 rotated to the opposite
       clock side.
    n = 60;
    M = imgdfsm(xmin-1:xmin+1, ymin-n:ymin+n);
    dfline(cnt,1:2*n+1) = mean(M', 2);
    df(:,cnt)= dfline(cnt,1:2*n+1);

    [A, imgcur] = loadsxm(fname, 8);
    offsetc = mean(mean(imgcur(118:128, 1:10)));
    bgd(cnt,:) = mean2(offsetc);
end
%meters per pixel
    mpp = A.scan_range(1) / A.scan_pixels(1);

%% load z spectrum, calculate absulute heights and convolute
   forces again
% load and confirm z spectrum
fbasename = 'C:\Users\LocalAdmin\Desktop\2021-10-18\';
fname = [fbasename, 'Z-Spectroscopy00006.dat'];
h_lines=19;
data=importdata(fname,'\t',h_lines);
z=data.data(:,1);
curr=data.data(:,2);

figure;
plot(z,curr, 'r');
title('Z spectrum of current exponential region');

% Kappa fitten from the loaded z spectrum
p = polyfit(z, log(abs(curr)), 1);
calcys = polyval(p, z);

figure;
plot(z, log(abs(curr)), 'b.', z, calcys, 'k');
title('Kappa fit');
kappa = p(1)/(-2);
```

```
65
66 % Calculate heights
67 G0 = 77.5e-6;
68 Vt = 1e-3; %Bias voltage
69
70 for nt = 1:nfiles
71     currMeanDrift(nt) = abs(bgd(nt));
72     AbsZ(nt) = log(currMeanDrift(nt)/(Vt*G0))*1/(-2*kappa);
73 end
74 % Plot heights
75 figure;
76 plot((1:1:nfiles),AbsZ);
77 title('Absolute␣heights␣vs␣n');
```

Listing 3: This is used to determine the bond length between two Oxygens from the 3D data set.

.2 Persson's model describing the phononic contribution to friction

The contents of this section are all from Ref. [2]. In Persson's model, the friction force due to vibrational damping by a single adsorbate is given by:

$$F_{\text{atom},f,\text{vib}} = -m_{\text{t}} h u \tag{.1}$$

where m_{t} is the effective mass of the tip, h is the damping constant of the interaction, and u is the relative sliding velocity between the tip and the sample. The negative sign indicates that the friction force opposes the direction of motion.The total vibrational contribution is proportional to the number of adsorbates, which depends on the areal density σ and the contact area A. When variations in h caused by non-uniform contact stresses are neglected, the total vibrational contribution is

$$F_{f,\text{vib}} = m_{\text{t}} h \sigma u A \tag{.2}$$

For interfacial friction, the vibrational contribution to the shear strength is $\tau_{\text{vib}} = m_{\text{t}} h \sigma$.

The damping constant h is related to the density ρ and the transverse sound velocity c_T of the moving surface by:

$$h \approx \frac{3 m w^4}{8\pi \rho c_T^3} \tag{.3}$$

where m and w refer to the adsorbate's mass and vibrational frequency, respectively.

To illustrate the physics behind this equation, consider an adsorbate vibrating with energy E and colliding with the moving surface (the AFM tip). During one vibration cycle, the adsorbate transfers energy $\Delta E = \frac{m}{M_S} E$ to the tip, where M_S is the mass of the portion of the tip effectively involved in the collision. Thus, the energy transfer rate can be expressed as:

$$\dot{E} = -\frac{w}{2\pi} \frac{m}{M_S} E \tag{.4}$$

During the collision time $t \approx \frac{2\pi}{w}$, a local displacement field forms in the tip within

a distance $\frac{c_T}{w}$, corresponding to a volume $\left(\frac{c_T}{w}\right)^3$. Therefore, $M_S \approx \rho\left(\frac{c_T}{w}\right)^3$. The energy transfer rate is then:

$$\dot{E} \approx -\frac{mw^4}{2\pi\rho c_T^3}E \tag{.5}$$

The solution to this equation shows exponential decay with a damping constant $h = \frac{mw^4}{2\pi\rho c_T^3}$, which aligns with the quantity derived in the previous equation. Since $w \propto m^{-1/2}$, the damping constant h, shear strength τ, and friction force F_f all scale as $\frac{m}{m^2} \approx \frac{1}{m}$.

.2.1 Solving with a rate of energy dissipation per unit time

For an atom of mass m colliding with a much heavier surface of mass M, the energy transfer ΔE per collision is given by:

$$\Delta E = E_0\left(\frac{4mM}{(m+M)^2}\right)\sin^2\theta \tag{.6}$$

where E_0 is the energy associated with the atoms oscillation, m is the mass of the atom (H or D), M is the mass of the surface part, and θ is the collision angle. Assuming $M \gg m$, it can be approximated $m + M \approx M$. Thus, $\frac{m}{m+M} \approx \frac{m}{M}$ and $\left(\frac{m}{m+M}\right)^2 \approx \left(\frac{m}{M}\right)^2$. Therefore, the energy transfer for the atoms having a mass value of m can be simplified:

$$\Delta E \approx E_0\left(\frac{4m}{M}\right)\sin^2\theta \tag{.7}$$

The mass of the surface part M involved in the collision can be estimated with the mass density ρ, the transverse speed of sound c_T, and the period of one oscillation τ of the surface. For a more general volumetric estimate, if considering a characteristic length of $c_\mathrm{T}\tau$ in three dimensions, the mass M can be approximated as $M \approx \rho \cdot (c_\mathrm{T}\tau)^3$.

To calculate the rate of energy dissipation per unit time, the energy transferred per collision ΔE and the period of oscillation τ, which is related to the phonon frequency by $\omega = 2\pi/\tau$, can be used:

$$\frac{dE}{dt} = \frac{E_0\sin^2\theta\left(\frac{4m}{M}\right)}{\frac{2\pi}{\omega}} = \frac{E_0\sin^2\theta\left(\frac{4m\omega}{M}\right)}{2\pi} = \frac{1}{4\pi^4}\frac{m\omega^4}{\rho c_\mathrm{T}^3}\sin^2\theta \tag{.8}$$

When comparing surfaces terminated with H atoms to those terminated with D atoms, the primary difference lies in the oscillation frequency of these atoms, which affects how much energy is dissipated when these surfaces interact with their environment. To compare the energy dissipation between H and D, the ratio of dissipated energies can be calculated:

$$\frac{dE_{\mathrm{H}}}{dE_{\mathrm{D}}} = \frac{m_{\mathrm{H}}\omega_{\mathrm{H}}^4}{m_{\mathrm{D}}\omega_{\mathrm{D}}^4} \tag{.9}$$

By approximating the bond between the atom and the surface as a spring with spring constant k_{s}, $\omega = \sqrt{\frac{k_{\mathrm{s}}}{m}}$. Then, the energy dissipation ratio between surfaces terminated with H and D due to phononic effects is:

$$\frac{dE_{\mathrm{H}}}{dE_{\mathrm{D}}} = \frac{m_{\mathrm{H}}m_{\mathrm{D}}^2}{m_{\mathrm{D}}m_{\mathrm{H}}^2} = 2 \tag{.10}$$

with the assumption that the spring constant of the bonds is the same for H and D. Eq. .10 can be interpreted as that the lighter atoms vibrate at a higher frequency, resulting in a faster energy dissipation and greater friction compared to heavier species.

Here, the spring constant,k_{s}, indicates the stiffness of the spring or the rigidity of the bond. In a chemical bond, a higher spring constant means the bond is stronger and requires more force to stretch or compress it. Conversely, a lower spring constant means the bond is weaker and more easily stretched or compressed. By the assumptions in this theory, the bond stiffness, k_{s}, does not change with isotopes, but the vibrational frequency does, due to the change in reduced mass when they make a bond with the surface. Assuming there is no inherent chemical contrast between the H- and D-terminated surfaces, the force constant remains unchanged across different isotopes. However, the difference in mass affects the observed vibrational frequency.

This theory predicts that H-terminated surfaces will dissipate twice the energy per unit time compared to D-terminated surfaces, given the following assumptions:

- The surface atom mass M is much larger than the masses of H and D.
- The collision angle θ is the same for both H and D.
- The spring constant is the same for both H and D.

List of Publications

The following is a list of publications authored or co-authored by the author of this thesis.

- Nam, S., Riegel, E., Hõrmann, L., Hofmann, O. T., Gretz, O., Weymouth, A. J., and Giessibl, F. J. , *Exploring in-plane interactions beside an adsorbed molecule with lateral force microscopy.*, Proceedings of the National Academy of Sciences of the United States of America, 121(2), (2024).

Bibliography

[1] E. Gnecco and E. Meyer. *Elements of Friction Theory and Nanotribology*. 2015.

[2] M. Winfried. *Springer-Verlag Berlin Heidelberg GmbH Physics and Astronomy*. 1993.

[3] R. W. Carpick and M. Salmeron. Scratching the Surface: Fundamental Investigations of Tribology with Atomic Force Microscopy. *Chemical Reviews*, 97(4):1163–1194, jun 1997.

[4] S. Mandal, D. Dey, and P. Banerjee. Diving deep into the superior lubrication efficiency: A dynamic approach incorporating covalent organic polymer as strengthening booster in paraffin oil through a holistic blend of experimental and computational approaches. *Tribology International*, 195:109567, 2024.

[5] K. Holmberg and A. Erdemir. Global impact of friction on energy consumption, economy and environment. *FME Transactions*, 43(3):181–185, 2015.

[6] W. Wang, Y. Wang, H. Bao, B. Xiong, and M. Bao. Friction and wear properties in MEMS. *Sensors and Actuators A: Physical*, 97-98:486–491, 2002.

[7] I. S. Y. Ku, T. Reddyhoff, A. S. Holmes, and H. A. Spikes. Wear of silicon surfaces in MEMS. *Wear*, 271(7):1050–1058, 2011.

[8] V. V. Deshpande, H.-Y. Chiu, H W Ch. Postma, C Mikó, L Forró, and M Bockrath. Carbon Nanotube Linear Bearing Nanoswitches. *Nano Letters*, 6(6):1092–1095, jun 2006.

[9] K. S. K. Karuppiah, Y. Zhou, L K. Woo, and S. Sundararajan. Nanoscale Friction Switches: Friction Modulation of Monomolecular Assemblies Using External Electric Fields. *Langmuir*, 25(20):12114–12119, oct 2009.

[10] N. V. Brilliantov, Yu A. Budkov, and C. Seidel. Theoretical and numerical analysis of nano-actuators based on grafted polyelectrolytes in an electric field. *Faraday Discussions*, 199:487–510, 2017.

[11] J. Li, H. Huang, and T. Morita. Stepping piezoelectric actuators with large working stroke for nano-positioning systems: A review. *Sensors and Actuators A: Physical*, 292:39–51, 2019.

[12] S. N. Zhang, B. Arfaei, and Z. Chen. Friction force reduction for electrical terminals using graphene coating. *Nanotechnology*, 32(3):35704, oct 2020.

[13] M. B. Farías, F. C Lombardo, A. Soba, P. I. Villar, and R. S. Decca. Towards detecting traces of non-contact quantum friction in the corrections of the accumulated geometric phase. *npj Quantum Information*, 6(1):25, 2020.

[14] G. V. Dedkov. Nonequilibrium CasimirLifshitz friction force and anomalous radiation heating of a small particle. *Applied Physics Letters*, 121(23):231603, 2022.

[15] Y. Xu, K. Fu, K. Liu, K. Sun, Y. Dong, and L. Yao. A state of the art review of the tribology of graphene/MoS2 nanocomposites. *Materials Today Communications*, 34:105108, 2023.

[16] A. Klemenz, L. Pastewka, S. G. Balakrishna, A. Caron, R. Bennewitz, and M. Moseler. Atomic Scale Mechanisms of Friction Reduction and Wear Protection by Graphene. *Nano Letters*, 14(12):7145–7152, dec 2014.

[17] B. Vasić, A. Matković, U. Ralević, M. Belić, and R. Gajić. Nanoscale wear of graphene and wear protection by graphene. *Carbon*, 120:137–144, 2017.

[18] C. Hou, S. Zhang, R. Liu, T. Gemming, A. Bachmatiuk, H. Zhao, H. Jia, S. Huang, W. Zhou, J. B. Xu, J. Pang, M. H. Rümmeli, J. Bi, H. Liu, and G. Cuniberti. Boosting flexible electronics with integration of two-dimensional materials. *InfoMat*, 6(7):1–50, 2024.

[19] Y. Guo, L. Zhang, Y. Wang, J. Liang, X. Liu, Y. Jiang, L. Jiang, and H. Chen. Nanofiber embedded bioinspired strong wet friction surface. *Science Advances*, 9(41):1–11, 2023.

[20] H. Lee, B. P. Lee, and P. B. Messersmith. A reversible wet/dry adhesive inspired by mussels and geckos. *Nature*, 448(7151):338–341, 2007.

[21] J Li, A .D. Celiz, J. Yang, Q. Yang, I. Wamala, W. Whyte, B .R. Seo, N. V. Vasilyev, J. J. Vlassak, Z. Suo, and D. J. Mooney. Tough adhesives for diverse wet surfaces. *Science (New York, N.Y.)*, 357(6349):378–381, jul 2017.

[22] D. Kim, J. Ahn, W. Choi, H. Kim, T. Kim, J. Song, Y. Huang, Z. Liu, C. Lu, and J. .A. Rogers. Stretchable and foldable silicon integrated circuits. *Science (New York, N.Y.)*, 320(5875):507–511, apr 2008.

[23] K. Jang, H. Jung, J. Lee, S. Xu, Y. Liu, Y. Ma, J. Jeong, Y. Song, J. Kim, B. Kim, A. Banks, J. Kwak, Y. Yang, D. Shi, Z. Wei, X. Feng, U. Paik, Y. Huang, R. Ghaffari, and J. A. Rogers. Ferromagnetic, folded electrode composite as a soft interface to the skin for long-term electrophysiological recording. *Advanced functional materials*, 26(40):7281–7290, oct 2016.

[24] S. Emaminejad, W. Gao, E. Wu, Z. A. Davies, H. Yin Yin N., S. Challa, S. P. Ryan, H.M. Fahad, K. Chen, Ziba Shahpar, Salmonn Talebi, Carlos Milla, Ali Javey, and Ronald W Davis. Autonomous sweat extraction and analysis applied to cystic fibrosis and glucose monitoring using a fully integrated wearable platform. *Proceedings of the National Academy of Sciences of the United States of America*, 114(18):4625–4630, may 2017.

[25] Da. de Sancho, A. Sirur, and R. B. Best. Molecular origins of internal friction effects on protein-folding rates. *Nature Communications*, 5(1):4307, 2014.

[26] B. G. Wensley, S. Batey, F. A C Bone, Z. M. Chan, N. R. Tumelty, A. Steward, L. G. Kwa, Al. Borgia, and J. Clarke. Experimental evidence for a frustrated energy landscape in a three-helix-bundle protein family. *Nature*, 463(7281):685–688, feb 2010.

[27] V. Bormuth, V. Varga, J. Howard, and E. Schäffer. Protein friction limits diffusive and directed movements of kinesin motors on microtubules. *Science (New York, N.Y.)*, 325(5942):870–873, aug 2009.

[28] R. Iino, K. Kinbara, and Z. Bryant. Introduction: Molecular Motors. *Chemical Reviews*, 120(1):1–4, jan 2020.

[29] G. M. Ashraf, N. H. Greig, T. A. Khan, I. Hassan, S. Tabrez, S. Shakil, I. A. Sheikh, S. K. Zaidi, M. Akram, N. R. Jabir, C. K. Firoz, A. Naeem, I. M. Alhazza, G. A. Damanhouri, and M. A. Kamal. Protein misfolding and aggregation in Alzheimer's disease and type 2 diabetes mellitus. *CNS & neurological disorders drug targets*, 13(7):1280–1293, 2014.

[30] E. Reynaud. Protein misfolding and degenerative diseases. *Nat. Educ.*, 3, 2010.

[31] E. L. Bortel, B. Charbonnier, and R. Heuberger. Development of a Synthetic Synovial Fluid for Tribological Testing. *Lubricants*, 3(4):664–686, 2015.

[32] M. Marian, R. Shah, B. Gashi, S. Zhang, K. Bhavnani, S. Wartzack, and A. Rosenkranz. Exploring the lubrication mechanisms of synovial fluids for joint longevity A perspective. *Colloids and Surfaces B: Biointerfaces*, 206:111926, 2021.

[33] R. P. Feynman. *The Feynman Lectures on Physics II - Electromagnatism*, volume 53. 2013.

[34] S. Yu Krylov and J. W.M. Frenken. The physics of atomic-scale friction: Basic considerations and open questions. *Physica Status Solidi (B) Basic Research*, 251(4):711–736, 2014.

[35] G Binnig. Atomic force microscope and method for imaging surfaces with atomic resolution - US Patent 4724318. *US Patent 4724318*, (19), 1986.

[36] F. J. Giessibl. Advances in atomic force microscopy. *Reviews of Modern Physics*, 75(3):949–983, 2003.

[37] A. J. Weymouth. Non-contact lateral force microscopy. *Journal of Physics Condensed Matter*, 29(32), 2017.

[38] C. M. Mate, G. M. McClelland, R. Erlandsson, and S. Chiang. Atomic-scale friction of a tungsten tip on a graphite surface. *Physical Review Letters*, 59(17):1942–1945, 1987.

[39] R. Bennewitz. Friction force microscopy. *Materials Today*, 8(5):42–48, 2005.

[40] A. Socoliuc, R. Bennewitz, E. Gnecco, and E. Meyer. Transition from Stick-Slip to Continuous Sliding in Atomic Friction: Entering a New Regime of Ultralow Friction. *Phys. Rev. Lett.*, 92(13):134301, apr 2004.

[41] R. W. Carpick, D. F. Ogletree, and M. Salmeron. Lateral stiffness: A new nanomechanical measurement for the determination of shear strengths with friction force microscopy. *Applied Physics Letters*, 70(12):1548–1550, 1997.

[42] M. Hirano. Superlubricity: A state of vanishing friction. *Wear*, 254(10):932–940, 2003.

[43] L. Prandtl. Ein Gedankenmodell zur kinetischen Theorie der festen Korper. *Z. Angew. Math. Mech*, 8(85), 1928.

[44] G.A. Tomlinson. *A molecular theory of friction*, volume 7. CAMBRIDGE, 1929.

[45] G. Meyer and N. M. Amer. Novel optical approach to atomic force microscopy. *Applied Physics Letters*, 53(12):1045–1047, 1988.

[46] G. Meyer and N. M. Amer. Simultaneous measurement of lateral and normal forces with an opticalbeamdeflection atomic force microscope. *Applied Physics Letters*, 57(20):2089–2091, 1990.

[47] T. R. Albrecht, D. Horne, and D. Rugar. Frequency modulation detection using high . 673:668–673, 1991.

[48] F. J. Giessibl. High-speed force sensor for force microscopy and profilometry utilizing a quartz tuning fork. *Applied physics letters*, 73(26):3956–3958, 1998.

[49] F. J. Giessibl, M. Herz, and J. Mannhart. Friction traced to the single atom. *Proceedings of the National Academy of Sciences of the United States of America*, 99(19):12006–12010, 2002.

[50] A. J. Weymouth, D. Meuer, P. Mutombo, T. Wutscher, M. Ondracek, P. Jelinek, and F. J. Giessibl. Atomic structure affects the directional dependence of friction. *Physical Review Letters*, 111(12):1–4, 2013.

[51] A. J. Weymouth, O. Gretz, E. Riegel, and F. J. Giessibl. Measuring sliding friction at the atomic scale. *Japanese Journal of Applied Physics*, 61(SL):SL0801, sep 2022.

[52] L. Gross, F. Mohn, N. Moll, P. Liljeroth, and G. Meyer. The Chemical Structure of a Molecule Resolved by Atomic Force Microscopy. *Science*, 325(5944):1110–1114, aug 2009.

[53] M. Emmrich, F. Huber, F. Pielmeier, J. Welker, T. Hofmann, M. Schneiderbauer, D. Meuer, S. Polesya, S. Mankovsky, D. Ködderitzsch, H. Ebert, and F.J. Giessibl. Subatomic resolution force microscopy reveals internal structure and adsorption sites of small iron clusters. *Science*, 348(6232):308–311, 2015.

[54] J. Welker and F.J. Giessibl. Revealing the angular symmetry of chemical bonds by atomic force microscopy. *Science*, 336(6080):444–449, 2012.

[55] J. Welker, A. John Weymouth, and F. J Giessibl. The Influence of Chemical Bonding Configuration on Atomic Identification by Force Spectroscopy. *ACS Nano*, 7(8):7377–7382, aug 2013.

[56] A.J. Weymouth, E. Riegel, O. Gretz, and F. J. Giessibl. Strumming a Single Chemical Bond. *Physical Review Letters*, 124(19):196101, 2020.

[57] G. Binning, H. Rohrer, Ch. Gerber and E. W. Surface Studies by Scanning Tunneling Microscopy. *Phys. Rev. Lett.*, 49(57):6196, 1982.

[58] C. J. CHEN. *Introduction to Scanning Tunneling Microscopy*. 1993.

[59] G. Binnig, H. Rohrer, Ch Gerber, and E. Weibel. Tunneling through a controllable vacuum gap. *Applied Physics Letters*, 40(2):178–180, 1982.

[60] J. Bardeen. Tunneling from a many-particle point of view. *Physical Review*, 131(3):1083–1086, 1963.

[61] J. Tersoff Hamann and D. R. Theory and Application for the Scanning Tunneling Microscope. 50(25):1998, 1983.

[62] J. Tersoff and D. R. Hamann. Theory of the scanning tunneling microscope. *Physical Review B*, 31(2):805–813, 1985.

[63] U Diebold, J. F. Anderson, Kwok O Ng, and D Vanderbilt. Evidence for the tunneling site on transition-metal oxides: TiO2(110). *Physical Review Letters*, 77(7):1322–1325, 1996.

[64] M. A. Reed. Inelastic electron tunneling spectroscopy. *Materials Today*, 11(11):46–50, 2008.

[65] J. Lambe and R. C. Jaklevic. Molecular vibration spectra by inelastic electron tunneling. *Physical Review*, 165(3):821–832, 1968.

[66] D. M. Eigler A. J. Heinrich, J. A. Gupta, C. P. Lutz and We. Single-Atom Spin-Flip Spectroscopy. 306(October):466–469, 2004.

[67] B. C. Stipe, M. A. Rezaei, and W. Ho. Single-molecule vibrational spectroscopy and microscopy. *Science*, 280(5370):1732–1735, 1998.

[68] S. Kano, T. Tada, and Y. Majima. Nanoparticle characterization based on STM and STS. *Chemical Society Reviews*, 44(4):970–987, 2015.

[69] N. Lorente and M. Persson. Theory of single molecule vibrational spectroscopy and microscopy. *Physical Review Letters*, 85(14):2997–3000, 2000.

[70] F. J. Giessibl. The qPlus sensor, a powerful core for the atomic force microscope. *Review of Scientific Instruments*, 90(1), 2019.

[71] R. Daniel and H. Paul. Atomic Force Microscopy. *Physics Today*, 43(10):23–30, 1990.

[72] S. Morita, F. J. Giessibl, E. Meyer and R. Wiesendanger. *Noncontact Atomic Force Microscopy, Volume 3*. Springer-Verlag Berlin Heidelberg, 2015.

[73] B. Anczykowski, D. Krüger, K. L. Babcock, and H. Fuchs. Basic properties of dynamic force spectroscopy with the scanning force microscope in experiment and simulation. *Ultramicroscopy*, 66(3-4):251–259, 1996.

[74] H. Hölscher. Quantitative measurement of tip-sample interactions in amplitude modulation atomic force microscopy. *Applied Physics Letters*, 89(12), 2006.

[75] F. J. Giessibl. Forces and frequency shifts in atomic-resolution dynamic-force microscopy. *Physical Review B - Condensed Matter and Materials Physics*, 56(24):16010–16015, 1997.

[76] U. Dürig. Relations between interaction force and frequency shift in large-amplitude dynamic force microscopy. *Applied Physics Letters*, 75(3):433–435, 1999.

[77] F. J. Giessibl. A direct method to calculate tip-sample forces from frequency shifts in frequency-modulation atomic force microscopy. *Applied Physics Letters*, 78(1):123–125, 2001.

[78] J. E. Sader and S. P. Jarvis. Accurate formulas for interaction force and energy in frequency modulation force spectroscopy. *Applied Physics Letters*, 84(10):1801–1803, 2004.

[79] T. Seeholzer, O. Gretz, F. J. Giessibl, and A. J. Weymouth. A Fourier method for estimating potential energy and lateral forces from frequency-modulation lateral force microscopy data. *New Journal of Physics*, 21(8), 2019.

[80] Barry R Holstein. The van der Waals interaction. *American Journal of Physics*, 69(4):441–449, 2001.

[81] Tim Gould and Tomáš Bučko. C6 Coefficients and Dipole Polarizabilities for All Atoms and Many Ions in Rows 16 of the Periodic Table. *Journal of Chemical Theory and Computation*, 12(8):3603–3613, aug 2016.

[82] H C Hamaker. The Londonvan der Waals attraction between spherical particles. *Physica*, 4(10):1058–1072, 1937.

[83] Ivan Andrianov and Peter Saalfrank. Theoretical study of vibration-phonon coupling of H adsorbed on a Si(100) surface. *The Journal of Chemical Physics*, 124(3):34710, 2006.

[84] P Hohenberg and W Kohn. Inhomogeneous Electron Gas. *Phys. Rev.*, 136(3B):B864—-B871, nov 1964.

[85] Charlotte Froese Fischer. General Hartree-Fock program. *Computer Physics Communications*, 43(3):355–365, 1987.

[86] Volker Blum, Ralf Gehrke, Felix Hanke, Paula Havu, Ville Havu, Xinguo Ren, Karsten Reuter, and Matthias Scheffler. Ab initio molecular simulations with numeric atom-centered orbitals. *Computer Physics Communications*, 180(11):2175–2196, 2009.

[87] John P Perdew, Kieron Burke, and Matthias Ernzerhof. Generalized Gradient Approximation Made Simple. *Phys. Rev. Lett.*, 77(18):3865–3868, oct 1996.

[88] Victor G Ruiz, Wei Liu, Egbert Zojer, Matthias Scheffler, and Alexandre Tkatchenko. Density-Functional Theory with Screened van der Waals Interactions for the Modeling of Hybrid Inorganic-Organic Systems. *Phys. Rev. Lett.*, 108(14):146103, apr 2012.

[89] Alexandre Tkatchenko and Matthias Scheffler. Accurate Molecular Van Der Waals Interactions from Ground-State Electron Density and Free-Atom Reference Data. *Phys. Rev. Lett.*, 102(7):73005, feb 2009.

[90] P. Hapala, G. Kichin, C. Wagner, F. S. Tautz, R. Temirov, and P. Jelínek. Mechanism of high-resolution STM/AFM imaging with functionalized tips. *Physical Review B*, 90(8):085421, aug 2014.

[91] Philipp Schaffhauser and Stephan Kümmel. Simulating atomic force microscope images with density functional theory: The role of nonclassical contributions to the force. *Phys. Rev. B*, 94(3):35426, jul 2016.

[92] O. Gretz, A. J. Weymouth, T. Holzmann, K. Pürckhauer, and F. J. Giessibl. Determining Amplitude and Tilt of a Lateral Force Microscopy Sensor. *Beilstein Journal of Nanotechnology*, 12(Figure 1):517–524, 2021.

[93] W. L. Chan and E. Chason. Making waves: Kinetic processes controlling surface evolution during low energy ion sputtering. *Journal of Applied Physics*, 101(12), 2007.

[94] K. K. Gomes, W. Mar, W. Ko, F. Guinea, and H. C. Manoharan. Designer Dirac fermions and topological phases in molecular graphene. *Nature*, 483(7389):306–310, 2012.

[95] A. J. Weymouth, T. Hofmann, and F. J. Giessibl. Quantifying molecular stiffness and interaction with lateral force microscopy. *Science*, 343(6175):1120–1122, 2014.

[96] S. Nam, E. Riegel, L. Hõrmann, O. T. Hofmann, O. Gretz, A. J. Weymouth, and F. J. Giessibl. Exploring in-plane interactions beside an adsorbed molecule with lateral force microscopy. *Proceedings of the National Academy of Sciences of the United States of America*, 121(2), 2024.

[97] Fabian Mohn, Bruno Schuler, Leo Gross, and Gerhard Meyer. Different tips for high-resolution atomic force microscopy and scanning tunneling microscopy of single molecules. *Applied Physics Letters*, 102(7):73109, feb 2013.

[98] G. Schull, T. Frederiksen, A. Arnau, D. Sánchez-Portal, and R. Berndt. Atomic-scale engineering of electrodes for single-molecule contacts. *Nature nanotechnology*, 6(1):23–27, jan 2011.

[99] T. Hofmann, F. Pielmeier, and F. J Giessibl. Chemical and Crystallographic Characterization of the Tip Apex in Scanning Probe Microscopy. *Phys. Rev. Lett.*, 112(6):66101, feb 2014.

[100] N. Moll, L. Gross, F. Mohn, A. Curioni, and G. Meyer. The mechanisms underlying the enhanced resolution of atomic force microscopy with functionalized tips. *New Journal of Physics*, 12, 2010.

[101] L Bartels, G Meyer, and K.-H. Rieder. Controlled vertical manipulation of single CO molecules with the scanning tunneling microscope: A route to chemical contrast. *Applied Physics Letters*, 71(2):213–215, jul 1997.

[102] D.M. Eigler, C .P. Lutz, and W. E. Rudge. An atomic switch realized with the scanning tunnelling microscope. *Nature*, 352(6336):600–603, 1991.

[103] S. Ishi, Y. Ohno, and B. Viswanathan. An overview on the electronic and vibrational properties of adsorbed CO. *Surface Science*, 161(2):349–372, 1985.

[104] F. Huber, J. Berwanger, S. Polesya, S. Mankovsky, H. Ebert, and F. J Giessibl. Chemical bond formation showing a transition from physisorption to chemisorption. *Science (New York, N.Y.)*, 366(6462):235–238, oct 2019.

[105] N. Moll, L. Gross, F. Mohn, A. Curioni, and G. Meyer. A simple model of molecular imaging with noncontact atomic force microscopy. *New Journal of Physics*, 14(8):083023, aug 2012.

[106] M. Schneiderbauer, M. Emmrich, A. J. Weymouth, and F. J. Giessibl. CO Tip Functionalization Inverts Atomic Force Microscopy Contrast via Short-Range Electrostatic Forces. *Physical Review Letters*, 112(16):166102, apr 2014.

[107] J. Van Der Lit, F. Di Cicco, P. Hapala, P. Jelinek, and I. Swart. Submolecular Resolution Imaging of Molecules by Atomic Force Microscopy: The Influence of the Electrostatic Force. *Physical Review Letters*, 116(9):2–6, 2016.

[108] M. Ellner, N. Pavliček, P. Pou, B. Schuler, N. Moll, G. Meyer, L. Gross, and R. Peréz. The Electric Field of CO Tips and Its Relevance for Atomic Force Microscopy. *Nano Letters*, 16(3):1974–1980, 2016.

[109] O. Pfeiffer, R. Bennewitz, A. Baratoff, E. Meyer, and P. Grütter. Lateral-force measurements in dynamic force microscopy. *Phys. Rev. B*, 65(16):161403(R), apr 2002.

[110] A J Weymouth, T Wutscher, J Welker, T Hofmann, and F J Giessibl. Phantom Force Induced by Tunneling Current: A Characterization on Si(111). *Phys. Rev. Lett.*, 106(22):226801, jun 2011.

[111] M. Gajdoš and J. Hafner. CO adsorption on Cu(1 1 1) and Cu(0 0 1) surfaces: Improving site preference in DFT calculations. *Surface Science*, 590(2-3):117–126, 2005.

[112] P. M. Morse. Phys. Rev. *Phys. Rev.*, 34(1927):57–64, 1929.

[113] D. Z. Gao, J. Grenz, M. B. Watkins, F. Federici Canova, A. Schwarz, R. Wiesendanger, and A. L. Shluger. Using metallic noncontact atomic force microscope tips for imaging insulators and polar molecules: Tip characterization and imaging mechanisms. *ACS Nano*, 8(5):5339–5351, 2014.

[114] F. Schulz, J. Ritala, O. Krejčí, A.P. Seitsonen, A. S. Foster, and P. Liljeroth. Elemental Identification by Combining Atomic Force Microscopy and Kelvin Probe Force Microscopy. *ACS Nano*, 12(6):5274–5283, 2018.

[115] A. Schwarz, A. Köhler, J. Grenz, and R. Wiesendanger. Detecting the dipole moment of a single carbon monoxide molecule. *Applied Physics Letters*, 105(1), 2014.

[116] L Gross, F Mohn, N Moll, B Schuler, A Criado, E Guitián, D Peña, A Gourdon, and G Meyer. Bond-Order Discrimination by Atomic Force Microscopy. *Science*, 337(6100):1326–1329, sep 2012.

[117] O. Krejčí P. Hapala. Probe Particle Model. GitHub.

[118] Victor G. Ruiz, W. Liu, E. Zojer, M. Scheffler, and A. Tkatchenko. Density-functional theory with screened van der Waals interactions for the modeling of hybrid inorganic-organic systems. *Physical Review Letters*, 108(14):146103, 2012.

[119] A. Gerlach, S. Sellner, F. Schreiber, N. Koch, and J. Zegenhagen. Substrate-dependent bonding distances of PTCDA: A comparative x-ray standing-wave study on Cu(111) and Ag(111). *Physical Review B*, 75(4):045401, jan 2007.

[120] B. Such, D. Weiner, A. Schirmeisen, and H. Fuchs. Influence of the local adsorption environment on the intramolecular contrast of organic molecules in noncontact atomic force microscopy. *Applied Physics Letters*, 89(9):28–31, 2006.

[121] J. P. Perdew, K. Burke, and M. Ernzerhof. Generalized gradient approximation made simple. *Physical Review Letters*, 77(18):3865–3868, 1996.

[122] A. Tkatchenko and M. Scheffler. Accurate Molecular Van Der Waals Interactions from Ground-State Electron Density and Free-Atom Reference Data. *Physical Review Letters*, 102(7):073005, feb 2009.

[123] S. Kawai, T. Nishiuchi, T. Kodama, P. Spijker, R. Pawlak, T. Meier, J. Tracey, T. Kubo, E. Meyer, and A. S. Foster. Direct quantitative measurement of

the C==O · · · H-C bond by atomic force microscopy. *Science Advances*, 3(5):1–6, 2017.

[124] J. Peng, J. Guo, P. Hapala, D. Cao, R. Ma, B. Cheng, L. Xu, M. Ondráček, P. Jelínek, E. Wang, and Y. Jiang. Weakly perturbative imaging of interfacial water with submolecular resolution by atomic force microscopy. *Nature Communications*, 9(1):1–7, 2018.

[125] S. Kawai, N. Sasaki, and H. Kawakatsu. Direct mapping of the lateral force gradient on Si(111)-7x7. *Phys. Rev. B*, 79(19):195412, 2009.

[126] S. Kawai, T. Glatzel, S. Koch, B. Such, A. Baratoff, and E. Meyer. Ultrasensitive detection of lateral atomic-scale interactions on graphite (0001) via bimodal dynamic force measurements. *Phys. Rev. B*, 81(8):085420, 2010.

[127] F. Mohn, L. Gross, and G. Meyer. Measuring the short-range force field above a single molecule with atomic resolution. *Applied Physics Letters*, 99(5):1–4, 2011.

[128] B. Gotsmann, W. Allers, H. Hölscher, U. D. Schwarz, R. Wiesendanger, and H. Fuchs. Measurement of conservative and dissipative tip-sample interaction forces with a dynamic force microscope using the frequency modulation technique. *Physical Review B - Condensed Matter and Materials Physics*, 64(7):1–6, 2001.

[129] L. L. Patera, F. Queck, P. Scheuerer, and J. Repp. Mapping orbital changes upon electron transfer with tunnelling microscopy on insulators. *Nature*, 566(7743):245–248, 2019.

[130] M. Ondráček, P. Hapala, and P. Jelínek. Charge-state dynamics in electrostatic force spectroscopy. *Nanotechnology*, 27(27), 2016.

[131] Y. Sugimoto, P. Jelinek, P. Pou, M. Abe, S. Morita, R. Perez, and O. Custance. Mechanism for room-temperature single-atom lateral manipulations on semiconductors using dynamic force microscopy. *Physical Review Letters*, 98(10):1–4, 2007.

[132] S. Hembacher, F. J. Giessibl, J. Mannhart, and C. F. Quate. Local spectroscopy and atomic imaging of tunneling current, forces, and dissipation on graphite. *Physical Review Letters*, 94(5):1–4, 2005.

[133] A. Liebig, A. Peronio, D. Meuer, A. J. Weymouth, and F. J. Giessibl. High-precision atomic force microscopy with atomically-characterized tips. *New Journal of Physics*, 22(6), 2020.

[134] Th. Wagner, A. Bannani, C. Bobisch, H. Karacuban, and R. Möller. The initial growth of PTCDA on Cu(111) studied by STM. *Journal of Physics Condensed Matter*, 19(5), 2007.

[135] V. Blum, R. Gehrke, F. Hanke, P. Havu, V. Havu, X. Ren, K. Reuter, and M. Scheffler. Ab initio molecular simulations with numeric atom-centered orbitals. *Computer Physics Communications*, 180(11):2175–2196, 2009.

[136] J. Moreno and J. M. Soler. Optimal meshes for integrals in real- and reciprocal-space unit cells. *Physical Review B*, 45(24):13891–13898, 1992.

[137] L. Hörmann, A. Jeindl, and O. T. Hofmann. From a bistable adsorbate to a switchable interface: tetrachloropyrazine on Pt(111). *Nanoscale*, 14(13):5154–5162, 2022.

[138] M. Dienwiebel, G. S. Verhoeven, N. Pradeep, J. W.M. Frenken, J. A. Heimberg, and H. W. Zandbergen. Superlubricity of graphite. *Physical Review Letters*, 92(12):1–4, 2004.

[139] R. J. Cannara, M. J. Brukman, K. Cimatu, A. V. Sumant, S. Baldelli, and R.W. Carpick. Nanoscale friction varied by isotopic shifting of surface vibrational frequencies. *Science*, 318(5851):780–783, 2007.

[140] Y. Mo, M. H. Müser, and I. Szlufarska. Origin of the isotope effect on solid friction. *Physical Review B - Condensed Matter and Materials Physics*, 80(15):1–7, 2009.

[141] D. Matté, G. L. Rech, L. M. Leidens, J. E. Zorzi, A. F. Michels, C. A. Figueroa, and C. A. Perottoni. Molecular dynamics simulations of the isotopic effect on nanoscale friction. *Applied Physics A: Materials Science and Processing*, 127(9):1–9, 2021.

[142] F. G. Echeverrigaray, S. R. Sales De Mello, C. D. Boeira, L. M. Leidens, M. E.H. Maia Da Costa, F. L. Freire, F. Alvarez, A. F. Michels, and C. A. Figueroa. Nanoindentation unidirectional sliding and lateral force microscopy: Evaluation of experimental techniques to measure friction at the nanoscale. *AIP Advances*, 8(12), 2018.

[143] H. Lin, L. Habibova, A. Rauf, José D. Cojal G, N. Severin, S. Kirstein, I.M. Sokolov, and J. P. Rabe. At Least 10-fold Higher Lubricity of Molecularly Thin D2O vs H2O Films at Single-Layer Graphene-Mica Interfaces. *Nano Letters*, 22(19):7761–7767, 2022.

[144] A. Kandratsenka, H. Jiang, Y. Dorenkamp, S. M. Janke, M. Kammler, A. M. Wodtke, and O. Bünermann. Unified description of H-atominduced chemicurrents and inelastic scattering. *Proceedings of the National Academy of Sciences of the United States of America*, 115(4):680–684, 2018.

[145] H. Labidi, M. Taucer, M. Rashidi, M. Koleini, L. Livadaru, J. Pitters, M. Cloutier, M. Salomons, and R. A. Wolkow. Scanning tunneling spectroscopy reveals a silicon dangling bond charge state transition. *New Journal of Physics*, 17(7), 2015.

[146] M. B. Haider, J. L. Pitters, G. A. Dilabio, L. Livadaru, J. Y. Mutus, and R. A. Wolkow. Controlled coupling and occupation of silicon atomic quantum dots at room temperature. *Physical Review Letters*, 102(4):2–5, 2009.

[147] D. C. Harris and M. D. Bertolucci. *Symmetry and Spectroscopy: An Introduction to Vibrational and Electronic Spectroscopy*. Dover Books on Chemistry Series. Dover Publications, 1989.

[148] C. Housecroft and A. Sharpe. *Inorganic Chemistry*. Pearson Deutschland, 2018.

[149] G. Hähner, J. P. Toennies, and Ch. Wöll. Normal modes of CO adsorbed on metal surfaces. *Applied Physics A Solids and Surfaces*, 51(3):208–215, 1990.

[150] F. Hofmann and J. P. Toennies. High-resolution helium atom time-of-flight spectroscopy of low-frequency vibrations of adsorbates. *Chemical Reviews*, 96(4):1307–1326, 1996.

[151] N. Okabayashi, M. Paulsson, and T. Komeda. Inelastic electron tunneling process for alkanethiol self-assembled monolayers. *Progress in Surface Science*, 88(1):1–38, 2013.

[152] N. Okabayashi, A. Gustafsson, A. Peronio, M. Paulsson, T. Arai, and F. J. Giessibl. Influence of atomic tip structure on the intensity of inelastic tunneling spectroscopy data analyzed by combined scanning tunneling spectroscopy, force microscopy, and density functional theory. *Physical Review B*, 93(16):1–6, 2016.

[153] N. Okabayashi, A. Peronio, M. Paulsson, T. Arai, and F. J. Giessibl. Vibrations of a molecule in an external force field. *Proceedings of the National Academy of Sciences of the United States of America*, 115(18):4571–4576, 2018.

[154] L. Vitali, R. Ohmann, K. Kern, A. Garcia-Lekue, T. Frederiksen, D. Sanchez-Portal, and A. Arnau. Surveying molecular vibrations during the formation of metal-molecule nanocontacts. *Nano Letters*, 10(2):657–660, 2010.

[155] A. J. Heinrich, C. P. Lutz, J. A. Gupta, and D. M. Eigler. Molecule cascades. *Science*, 298(5597):1381–1387, 2002.

[156] A. Peronio, N. Okabayashi, F. Griesbeck, and F.J. Giessibl. Radio frequency filter for an enhanced resolution of inelastic electron tunneling spectroscopy in a combined scanning tunneling- And atomic force microscope. *Review of Scientific Instruments*, 90(12), 2019.

[157] V A Bufeev. Wave losses during friction. *Soviet Physics Journal*, 15(5):689–693, 1972.

[158] J B Sokoloff. Theory of energy dissipation in sliding crystal surfaces. *Phys. Rev. B*, 42(1):760–765, jul 1990.

[159] J B Sokoloff. Theory of atomic level sliding friction between ideal crystal interfaces. *Journal of Applied Physics*, 72(4):1262–1270, aug 1992.

[160] V L Popov. Superslipperiness at Low Temperatures: Quantum Mechanical Aspects of Solid State Friction. *Phys. Rev. Lett.*, 83(8):1632–1635, aug 1999.

[161] S. Kajita, H. Washizu, and T. Ohmori. Deep bulk atoms in a solid cause friction. *Europhysics Letters*, 87(6):66002, oct 2009.

[162] V L Popov. Electronic contribution to sliding friction in normal and superconducting states. *Journal of Experimental and Theoretical Physics Letters*, 69(7):558–561, 1999.

[163] J E Sacco, J B Sokoloff, and A Widom. Dynamical friction in sliding condensed-matter systems. *Phys. Rev. B*, 20(12):5071–5083, dec 1979.

[164] J B Sokoloff. Theory of the contribution to sliding friction from electronic excitations in the microbalance experiment. *Phys. Rev. B*, 52(7):5318–5322, aug 1995.

[165] S. R.Sales De Mello, M. E.H.Maia Da Costa, C. M. Menezes, C. D. Boeira, F. L. Freire, F. Alvarez, and C. A. Figueroa. On the phonon dissipation contribution to nanoscale friction by direct contact. *Scientific Reports*, 7(1):1–8, 2017.

[166] J. J. Boland. Scanning tunnelling microscopy of the interaction of hydrogen with silicon surfaces. *Advances in Physics*, 42(2):129–171, 1993.

[167] J. Croshaw, T. Dienel, T. Huff, and R. Wolkow. Atomic defect classification of the H-Si(100) surface through multi-mode scanning probe microscopy. *Beilstein Journal of Nanotechnology*, 11(100):1346–1360, 2020.

[168] A. Sweetman, S. Jarvis, R. Danza, J. Bamidele, L. Kantorovich, and P. Moriarty. Manipulating Si(100) at 5 K using qPlus frequency modulated atomic force microscopy: Role of defects and dynamics in the mechanical switching of atoms. *Physical Review B - Condensed Matter and Materials Physics*, 84(8):1–10, 2011.

[169] A. Sweetman, S. Jarvis, R. Danza, J. Bamidele, S. Gangopadhyay, G.A. Shaw, Lev Kantorovich, and Philip Moriarty. Toggling bistable atoms via mechanical switching of bond angle. *Physical Review Letters*, 106(13):1–4, 2011.

[170] A. Sweetman, S. Jarvis, R. Danza, and P. Moriarty. Effect of the tip state during qPlus noncontact atomic force microscopy of Si(100) at 5 K: Probing the probe. *Beilstein Journal of Nanotechnology*, 3(1):25–32, 2012.

[171] D. Sawada, T. Namtkawa, M. Hiragaki, Y. Sugimoto, M. Abe, and S. Morita. High-spatial-resolution topographic imaging and dimer distance analysis of Si(100)-(2 Œ 1) using noncontact atomic force microscopy. *Japanese Journal of Applied Physics*, 47(7 PART 3):6085–6087, 2008.

[172] J. J. Boland. Structure of the H-saturated Si(100) surface. *Physical Review Letters*, 65(26):3325–3328, 1990.

[173] Y. J. Chabal Raghavachari and Krishnan. New Ordered Structure for the H-Saturated Si(100) Surface: The (3x1) Phase. 54(10):1055, 1985.

[174] R. Achal, M. Rashidi, J. Croshaw, D. Churchill, M. Taucer, T. Huff, M. Cloutier, J. Pitters, and R.A. Wolkow. Lithography for robust and editable atomic-scale silicon devices and memories. *Nature Communications*, 9(1), 2018.

[175] T. R. Huff, H. Labidi, M. Rashidi, M. Koleini, R. Achal, M. H. Salomons, and R. A. Wolkow. Atomic White-Out: Enabling Atomic Circuitry through Mechanically Induced Bonding of Single Hydrogen Atoms to a Silicon Surface. *ACS Nano*, 11(9):8636–8642, 2017.

[176] S.Y. Krylov and J. W.M. Frenken. The physics of atomic-scale friction: Basic considerations and open questions. *Physica Status Solidi (B) Basic Research*, 251(4):711–736, 2014.

[177] D. Gangloff, A. Bylinskii, I. Counts, W. Jhe, and V. Vuletić. Velocity tuning of friction with two trapped atoms. *Nature Physics*, 11(11):915–919, 2015.

Acknowledgments

First and foremost, I want to thank my Doktorvater, PD. Dr. Jay Weymouth, for his constant support, patience, and invaluable advice. His guidance and ever-present encouragement have been a true source of motivation throughout my PhD journey, and Im deeply grateful for everything he has taught me. My first international experience in Germany was made both smooth and memorable thanks to his warm concern. Furthermore, the many conference opportunities he provided made me braver and more confident. I especially want to mention our awesome running days and birthday cakes at the conference in Singapore.

I want to express my heartfelt gratitude to my big boss, Prof. Dr. Franz J. Gießibl, for his insightful advice and incredible support (and for the marathon!). I will never forget his enthusiasm and his knack for turning challenges into opportunities. I truly admire his genuine curiosity and philosophical perspective on fundamental physics. This helped me grow as an independent thinker, entertaining a thought without necessarily accepting it. Additionally, I want to thank him for his final feedback on this thesis, which helped shape this work.

My research became much more fruitful thanks to Prof. Dr. Jascha Repp. His clear and sharp comments during seminars helped me organize my ideas and perspectives. I truly appreciate our discussions, as well as his constant willingness to say 'yes' whenever I asked for favors or had questions.

A huge thank you to my thesis committee members, Prof. Dr. Andrea Donarini, Prof. Dr. Rupert Huber, and Prof. Dr. Isabella Gierz, for your thoughtful feedback and encouragement. I would like to deeply thank Prof. Dr. Rupert Huber for the second assessment of this thesis, as well as for the meetings, kind and sincere advice, and for giving me the wonderful opportunity to present at the RUN seminar. His ability to working efficiently and finding time for students, even in the middle of his busy schedule, touched me and was a significant source of motivation.

I'm also fortunate to have been surrounded by amazing colleagues in the LT3

team: Maximilian Titl, Jyotiraditya Mishra, Hannah Spirkl, Bianca Simmet, Thomas Holzmann, and Oliver Gretz. A special thanks to Maxi, whose problem-solving skills were a huge help, especially with the tip stiffness calculation. His quick and skilled sensor building made my job so much easier. I'm also really grateful to Aditya for his passion and intuitive thinking, particularly with flashing Si samples his dedication always pushed our team forward. Hannah's hard work and patience on friction anisotropy gave me the first real insights into the project. I also want to give a big shoutout to my first-year colleagues, Bianca, Thomas, and Oliver, whose support and assistance were incredibly valuable. Thanks to many insightful discussions and the automation of data acquisition as well as flash through clever coding, my life was made much easier. The wonderful times we shared during the Hütten seminar will never be forgotten. From shared frustrations over broken equipment to celebrating the little wins, this experience wouldnt have been the same without you all. The laughs, long discussions, and shared struggles made this journey not only productive but also enjoyable.

I'd like to extend a special thanks to our international collaborators and visiting scientists. Im particularly grateful to Dr. Lukas Hörmann and Prof. Dr. Oliver T. Hofmann for their exceptional work on the DFT simulations for the CO snapping model. Their calculations greatly enriched our project and interpretations.

A heartfelt thank you goes to Prof. Dr. Norio Okabayashi for his frequent research visits and for collaborating with LT3. I deeply appreciate our insightful discussions, especially about IETS measurements and his precise measurement skills. I admire his dedication and perseverance, which have been a source of inspiration for me.

A big shoutout to Marco Weiss, Adrian Weindl, Fabian Stilp, and the 'next generation' Chris Setescak, Michael Schelchshorn, and Sophia Schweiss. Their support was invaluable in helping me complete my thesis on time, especially through their diligent proofreading of each chapter. I deeply cherish the time we shared as friends, always there for me through the ups and downs of my first international experience - even in covid times..! At the end of my PhD journey, the short but productive time I spent working with Michael and Sophia, along with the nice help from others, allowed me to focus and complete my thesis. Your constant support, engaging discussions, and the fun times weve shared at conferences, excursions, and board game evenings have meant a lot to me. Whenever I was feeling worn out,

your quiet gestures of support, like offering a beer or a game of billiards, gave me the boost I needed to keep going. Our time is definitely one warm chapter in my life, which I will never forget.

Warm thanks to Claudia, Anja, and Florian! Thanks to punctual and efficient mechanical work from Anja and Florian, our experiment could have been much faster. Claudia was incredibly helpful with document tasks, even those that were not necessarily part of her responsibilities. This kind support allowed me to think more clearly and stabilized my work process.

I also want to thank my previous lab supervisors, Prof. Dr. Andreas Heinrich, Dr. Jungseok Chae, and Dr. Jinoh Jung at QNS, who sparked my initial curiosity about nano science and encouraged me to be brave in asking questions and stepping out into the wider world. The experience of setting up and working (with a old machine that time ;)) actually strengthened my resilience whenever I faced issues in life. The wide network established by Andreas helped me grab the opportunity to work with my current team. I am deeply grateful for these experiences, as well as the warm and welcoming atmosphere they provided, which always made me feel at home and re-energized whenever I visited Korea.

Finally, to my family and friends, as well as my puppy, thank you for always being there for me. With warm hearts, you constantly gave me the strength to take one more step, even in the toughest moments, through the power of your love. Your unwavering support and encouragement, offered unconditionally, carried me through all the highs and lows of this journey. I will never forget the final night of completing this thesis. This wonderful achievement would not have been possible without you.